UCGE Reports
Number 20248

Department of Geomatics Engineering

Global and Local Gravity Field Recovery from Satellite-to-Satellite Tracking

(URL: http://www.geomatics.ucalgary.ca/research/publications/GradTheses.html)

by

Matthias Luigi Weigelt

January 2007

UNIVERSITY OF CALGARY

Global and Local Gravity Field Recovery from Satellite-to-Satellite Tracking

by

MATTHIAS LUIGI WEIGELT

A THESIS
SUBMITTED TO THE FACULTY OF GRADUATE STUDIES
IN PARTIAL FULFILLMENT OF THE REQUIREMENTS FOR THE
DEGREE OF DOCTOR OF PHILOSOPHY

DEPARTMENT OF GEOMATICS ENGINEERING

CALGARY, ALBERTA
JANUARY, 2007

Abstract

The main objective of this thesis is the gravity field recovery using satellite-to-satellite tracking methods. Based on new technologies like the global positioning system and accelerometers satellite-to-satellite tracking yields a dramatic improvement in the determination of the Earth gravity field. Two dedicated satellite missions, namely the CHAllenging Minisatellite Payload (CHAMP) and the Gravity Recovery And Climate Experiment (GRACE) are underway. This work describes the processing of the satellite data from CHAMP and GRACE based on the energy balance approach. The first part discusses the global gravity field recovery from CHAMP. Specifically, it aims at a reprocessing of kinematic position data and at a refinement of the data processing strategies. Although the energy balance approach is theoretically simple, its implementation proved to be quite challenging. By refining the processing techniques an improvement of up to 30% is reached for the low degree spherical harmonic coefficients. Nevertheless, the solutions still depend strongly on the variability of the groundtrack. The quality of the monthly solutions can vary up to one order of magnitude. To address this challenge, an in-depth analysis gives new insight into the phenomenon, and a new and unique combination method with GRACE data is presented, which yields a more homogeneous set of solutions and reaches the edge of the recoverability of a time-variable gravity signal from high-low satellite-to-satellite tracking missions. In the second part the energy balance approach is applied to the GRACE mission. Previous attempts of expressing the kinetic energy in terms of the K-band measurement make use of an approximation. In this work, an exact representation is introduced and is validated by simulations. In the third part, the aim is to make optimal usage of the data distribution in the high latitude area. For this, interpolation and downward continuation techniques are investigated and an improvement, compared to the global solutions, is achieved. Overall, the analysis provides new and valuable insight into the data processing of satellite-to-satellite tracking data using the energy balance approach.

Acknowledgement

First and foremost, I want to express my deepest gratitude to my supervisors, Dr. N. Sneeuw and Dr. M.G. Sideris, for their encouragement and advice throughout my studies. Their continuous support and patience to answer countless questions, is highly appreciated. I also wish to thank the third member of my supervisory committee, Dr. N. El-Sheimy, for his advice and comments on the thesis.

The work of the two other members of the examining committee, Dr. L. Lines and Dr. C.K. Shum, is also highly appreciated. Their thorough proofreading and directions helped deepening the discussions and clarifying the content of the thesis.

I am also very thankful to Dr. R. Rummel, who sparked my interest in Physical Geodesy and gave me the opportunity for visiting the Institute of Astronomical and Physical Geodesy, TU Munich, as a research fellow during my studies. Furthermore, I would like to express my thanks to D. Švehla for providing the kinematic data, to Dr. C. Gerlach for his advice and tide code, and to M. Wermuth for his assistance.

Funding for my PhD studies was provided by the Werner Graupe International Fellowship, GEOIDE, the University of Calgary and the Department of Geomatics Engineering. I want to express my gratitude for the support.

I also wish to thank Mohamed El-Habiby and his family for their great friendship and support. We went through good and bad times forming a friendship for life. Katrin and Stefan, Carina, Bihter, Dr. Alexander Braun, Wouter and Cécile, Balaji, Chen and April, Elena, Vidya, Rossen, Georgia, Raymond, Niklas and Julia, Eric and Elisabeth, Taher and his family, all these friends supported me. I am glad to have met you and, without you, the stay had not been as wonderful.

Last but not least, I am very thankful to God for my dear parents, my brother and his lovely wife. They gave me strength, support and encouragement. Without them I could not have done it and, therefore, I dedicate this work to them.

To my parents, Mum and Dad,

my brother Oliver and his wife Britta

Contents

List of Tables

List of Figures

Chapter 1

Introduction

1.1 Historical development of physical geodesy

The determination of the shape of the Earth dates back to Aristotle (384–322 B.C.). He assumed the Earth to be spherical and based his theory on the natural motion of the elements. The first determination of its radius was performed by Eratosthenes of Cyrene (276–194 B.C.). He developed the principle of the arc-measurement and determined the circumference of the Earth to be 252 000 stadia ($\approx$ 37 000 km).

Figure 1.1: Eratosthenes of Cyrene 276–194 B.C. (O'Connor and Robertson, 1999)

With the advent of the Roman empire and the following Christianization the idea of a spherical Earth was discarded and replaced by a flat Earth, surrounded by the sea and covered by the celestial dome. Although this idea was dominant, it was not accepted by all members of the church. Bishop Virgilius of Salzburg was convinced of the spherical shape of the Earth (700–784) and came into conflict with the pope. Three centuries later the French pope Sylvester II. (999–1003) even agreed with the idea and wrote a series of works principally on philosophical, mathematical, and physical subjects. He was held in high repute for his learning capabilities, but the common people regarded him as a magician in league with the devil and many legends grew around his name. Nevertheless, he is said to have introduced the use of Arabic figures into Western Europe and to have invented the pendulum clock. At the end of the middle ages and with the

rise of the seafaring and the trading as well as the discovery of America by Christopher Columbus (1451–1506) and the voyage around the world by Ferdinand Magellan (1470–1521), the spherical shape of the Earth was established and the question of the size of the Earth became most urgent.

The breakthrough in its determination came in the end of the 16$^{\text{th}}$century when Willebrord Snel van Royen (1580–1626), called Snellius, developed the principle of triangulation. He used it to measure the arc between Bergen op Zoom and Alkmaar in order to determine the Earth's circumference. At the end of the 17$^{\text{th}}$century France assumed the leading role in geodesy and Jean Picard (1620–1682), a French astronomer, measured the meridian arc from Malvoisine through Paris to Amiens. His measurements were more precise than the one of Snellius since he equipped the telescopes with cross hairs. His measurements also supported the verification of Isaac Newton's (1642–1727) law of gravitation and for the time being the determination of the shape of the Earth was completed. The discussion started again when Giovanni Domenico Cassini (1625–1712) observed in 1666 the flattening of Jupiter. Additionally, Christiaan Huygens (1629–1695) showed with his precise pendulum measurements that a dependency on the location exists. It was Newton again who explained these phenomena and the precession of the Earth with his principle. The determination of the flattening of the Earth was pushed forward again by the Academy of Science in Paris. Two expeditions were sent out in order to measure meridian arcs. Pierre de Maupertuis (1698–1759) provided the first results from his expedition to Lapland and proved the flattening of the Earth.

Figure 1.2: Snellius (1580–1626 A.D.) (Kertz, 2002)

At the end of the 18th century methods using satellites were used for the first time. Pierre Simon Laplace (1749–1827) used the lunar nodal motion to determine the flat-

tening of the Earth. The term *satellite geodesy* was formed only later. At the same time the basics of potential theory were developed by the work of Jean Henri Lambert (1728–1777), Comte Louis de Lagrange (1736–1813) and Adrien Marie Legendre (1752–1833). George Gabriel Stokes (1819–1903) introduced in 1849 the connection between the potential, the surface of the Earth and the mass distribution inside the Earth. Johann B. Listing (1808–1882) formed the term *geoid*, which is the mathematical and geometrical shape of the Earth as an equipotential surface at mean sea level and is still in use today. At the same time, Friedrich Robert Helmert (1843–1917) conceived his definition of geodesy, which is the science of measurement and mapping of the Earth's surface. He added that geodesy is also teaching the method of determining the shape of the Earth and mapping of any arbitrarily sized parts by horizontal projection and heights under the consideration of the shape of potential surfaces. At the beginning of the 20$^{\text{th}}$century geodesy was established as a science field with a complete theory.

Figure 1.3: Johann B. Listing (1808–1882) (O'Connor and Robertson, 1999)

1.2 The decade of the geopotentials

The general objective is to determine the disturbing potential T. It is the part of the gravity field W which deviates from a normal (ellipsoidal) model U:

$$W = U + T \tag{1.1}$$

The quantity T cannot be observed directly. Instead so-called gravity anomalies Δg can be observed using, e.g., gravimeters. One way to derive the gravity field is the

so-called Stokes-integral:

$$T(r,\theta,\lambda) = \frac{R}{4\pi} \iint_{\sigma} S(r,\psi)\, \Delta g\, d\sigma \tag{1.2}$$

where θ is the co-latitude, λ the longitude, r the radius, R the mean Earth radius and σ denotes the integration over the whole body. The function $S(r,\psi)$ is the so-called Stokes function which gives a weight depending on the spherical distance ψ (and radius) to the calculation point. Similar integrals exists for other measured quantities, cf. Heiskanen and Moritz (1967) or Rummel and van Gelderen (1995). The geoid N is connected to the disturbing potential T by the equation of Bruns:

$$N = \frac{T}{\Delta g} \tag{1.3}$$

Consequently, the theory requires the knowledge of the gravity anomalies (or other quantities) all around the world in order to determine the geoid at a certain location. Especially in the beginning of the 20^{th} century this posed a huge problem for the geodetic community. The theory is still the same today and the problem could only be tackled with the development of dynamic satellite geodesy.

This relatively young branch of physical geodesy was adopted with the launch of the first artificial satellite Sputnik I on 4^{th}October 1957. The methods were used with several satellites but there was no dedicated satellite mission for the gravity field recovery till the year 2000. Gravity field models were derived from numerous data sources, like terrestrial, shipborne and airborne gravimetry, satellite tracking and altimetry, thus yielding a very inhomogeneous data set. Figure 1.4 shows the data density of terrestrial gravity anomalies and shipborne gravimetry in 1997. Only a few areas are well covered. Huge areas on the southern hemisphere, on the oceans, in the Arctic regions, but also in Russia and in Canada have only a sparse coverage and/or only a few measurements. The oceans are supplemented by altimetry measurements, which yields the sea surface though. Averaging over at least one year, the mean sea surface can be determined, which is a good approximation of the geoid but still deviates from it up to $\pm 1\,\text{m}$.

The situation worsens since the data has different quality and is taken with measurement techniques and instruments of variable accuracies. On the other hand, the

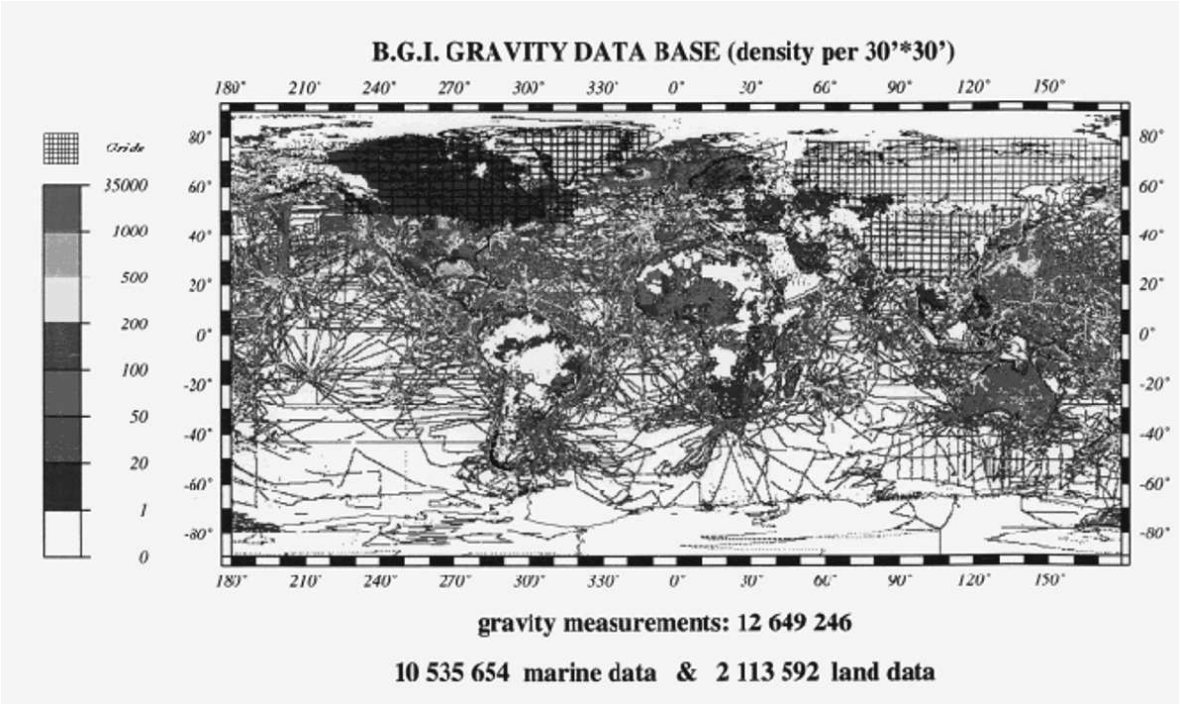

Figure 1.4: Gravity data available in 1997 collected by the Bureau Gravimetrique International (B.G.I.)

Earth with its atmosphere, oceans, ice sheets, land surfaces and its interior is subject to multiple dynamic processes. They cover a broad variety of spatial and temporal scales and are driven by large interior and exterior forces. Therefore, observations from space play an important role since only from space it is possible to monitor the dynamics of various processes globally with reasonable repetition rates and with homogeneous data quality (Ilk et al., 2004).

During the last three decades a large number of proposals for the gravity field recovery using satellite missions have been put forward, e.g., Geopotential Research Mission (GRM), ARISTOTELES or STEP. An overview of the historic development and a discussion of the benefits of these mission concepts can be found in Sneeuw and Ilk (1997). For this work, two concepts are of importance. Common to both concepts is that the lower the satellite flies, the better the sensitivity to the spatial variations of the gravity field is. However, a low Earth orbiter (LEO) will be influenced by non-

gravitational forces on the surface of the satellite, especially by atmospheric drag. These must either be modelled or measured by three-axis accelerometers. The basic concept of an accelerometer uses normally the gravity vector as a constant signal, and deviations are integrated to derive velocities and positions. In case of the satellite missions, the application is different. The accelerometers are placed into the center of mass of the satellite, which is in free fall. Therefore, the accelerometer does not sense any gravitational forces. In fact this is the very important property. Any forces measured are not due to gravitational attractions but due to non-gravitational forces like atmospheric drag, solar radiation pressure, etc.

The first concept to be considered here is the high-low satellite-to-satellite tracking (SST) case. A LEO is flying in an altitude of a few hundred kilometers and is continuously tracked by GPS; see figure 1.5(a). The concept is successfully implemented in the German geoscientific satellite CHAllenging Minisatellite Payload (CHAMP) which was launched in July 2000 into a highly inclined but circular orbit with an initial altitude of 450 km. The satellite decays slowly during the mission resulting in an in-orbit time of approximately 7 years. The improvement of the knowledge about the gravity field is almost one order of magnitude compared to any multi-satellite pre-CHAMP satellite-only gravity field model for half-wavelength longer than 200 km (Reigber et al., 2003). Due to the long mission duration, it has been expected to recover time variations of the gravity field as well but to date no attempt was successful.

In the case of low-low SST, two satellites are placed in the same orbit, separated by a few hundred kilometers. The quantity of interest is the relative motion of the mass center of the two satellites, which is measured with an highly accurate inter-satellite link. The low-low technique can also be combined with the high-low technique, cf. figure 1.5(b). The Gravity Recovery And Climate Experiment (GRACE), a joint US-German mission, is the implementation of this concept. The satellites were launched in 2002 into a near polar orbit and are flying at an initial altitude of about 500 km and are slowly decaying to an orbit height of approximately 300 km at the end of their lifetime. They are separated by approximately 200 km in the alongtrack direction. The observables are

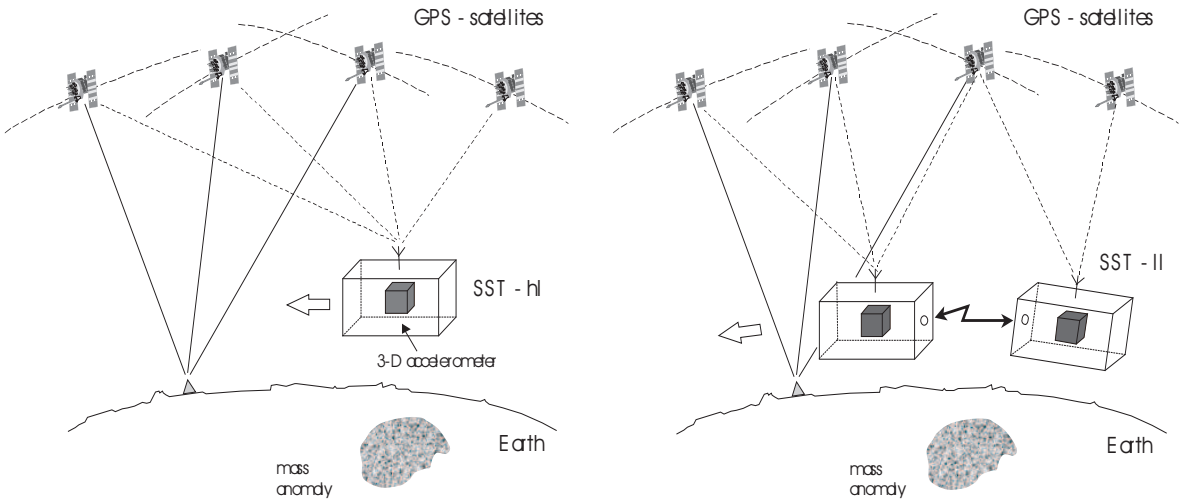

(a) high-low mode

(b) low-low mode

Figure 1.5: Concepts of satellite-to-satellite tracking

ranges, range rates and range accelerations. The advantage of the low-low SST technique is that these can be connected to differentiated quantities of the potential, thus yielding a much higher sensitivity. GRACE gives for the first time temporal variations on a global scale with a spatial resolution of 1000 km half-wavelength and higher. (Tapley et al., 2004b). It measures gravity changes due to mass redistribution related to hydrology, sea level, glaciology, solid Earth and atmosphere. The scientific challenge is the separation of these signals (Balmino et al., 1999).

1.3 Problem statement

The basic target of the research will be the recovery of the gravity field using satellite methods, globally and in high-latitude areas. The conventional way of computing the gravity from orbit data is the numerical integration of the equation of motion, as well as of the partial derivatives, also known as the variational equations of motion. Orbit and gravity field parameters are modelled in a combined way and the normal equation system, which is very large and full, is inverted (Reigber, 1989). Clearly, this is a costly operation in terms of processing time and computing resources, and can only be

treated on high performance computers. The near-continuous tracking of the CHAMP and GRACE satellites by GPS complicates the situation since a huge amount of data is available and needs to be processed. However, this technique, in combination with the accelerometer measurements, enables the implementation of new approaches, namely for this thesis the energy balance approach.

The basic principle is the decoupling of orbit determination and gravity field recovery. In the first step, position and velocity are solved for using the GPS data. In the second step, position, velocity and accelerometer data are connected to the gravity field. This method avoids problems related to orbit dynamics and initial state. It is considered for gravity field recovery purposes since the beginning of the satellite era (O'Keefe, 1957; Bjerhammer, 1967). Jekeli (1999) showed the applicability to the CHAMP and GRACE mission. He and Visser et al. (2003) showed also that the approach is highly sensitive to velocity errors. Nevertheless, it was successfully implemented by several groups for the case of CHAMP using the Rapid Science Orbits (RSO) provided by GeoForschungsZentrum Potsdam (GFZ); see Gerlach et al. (2003c); Howe et al. (2003); Han et al. (2002). Due to the low accuracy of the RSO the procedure was refined using the more accurate dynamic and reduced dynamic orbits (Gerlach et al., 2003b). However, Gerlach et al. (2003a) showed that the solution depends on the *a priori* gravity field used for the determination of dynamic positions and velocities. Švehla and Rothacher (2005) introduced GPS-derived kinematic positions that are based on a purely geometric approach and thus virtually independent of *a priori* information. The best result in terms of a global spherical harmonic model using these data to date is probably the TUM2s which was derived using two years of data (Wermuth et al., 2004; Földváry et al., 2005). The best model using the classical approach is probably the EIGEN-3P using 33 months of CHAMP data (Reigber et al., 2005b). Beside these, several models exist that combine satellite data from CHAMP and terrestrial data, e.g., Reigber et al. (2004).

The processing of CHAMP data, however, has never reached completeness. The EIGEN-3P model is still based on dynamic orbits and consequently the dependency

on a priori data is still inherent. The TUM2s model is based on kinematic orbits but is also criticized to have a deficient calibration procedure, thus filtering low degree gravity signal.

The results from the CHAMP mission improved the knowledge of the gravity field dramatically but one goal of this mission was not achieved. CHAMP was supposed to give first empirical results of a time-variable gravity field. The idea is to calculate monthly solutions of the gravity field and generate a mean of these snapshots. By subtracting the mean from the monthly solution the remaining is the time-variable part and errors. Sneeuw et al. (2005) analyzed the monthly solutions using this method and compared

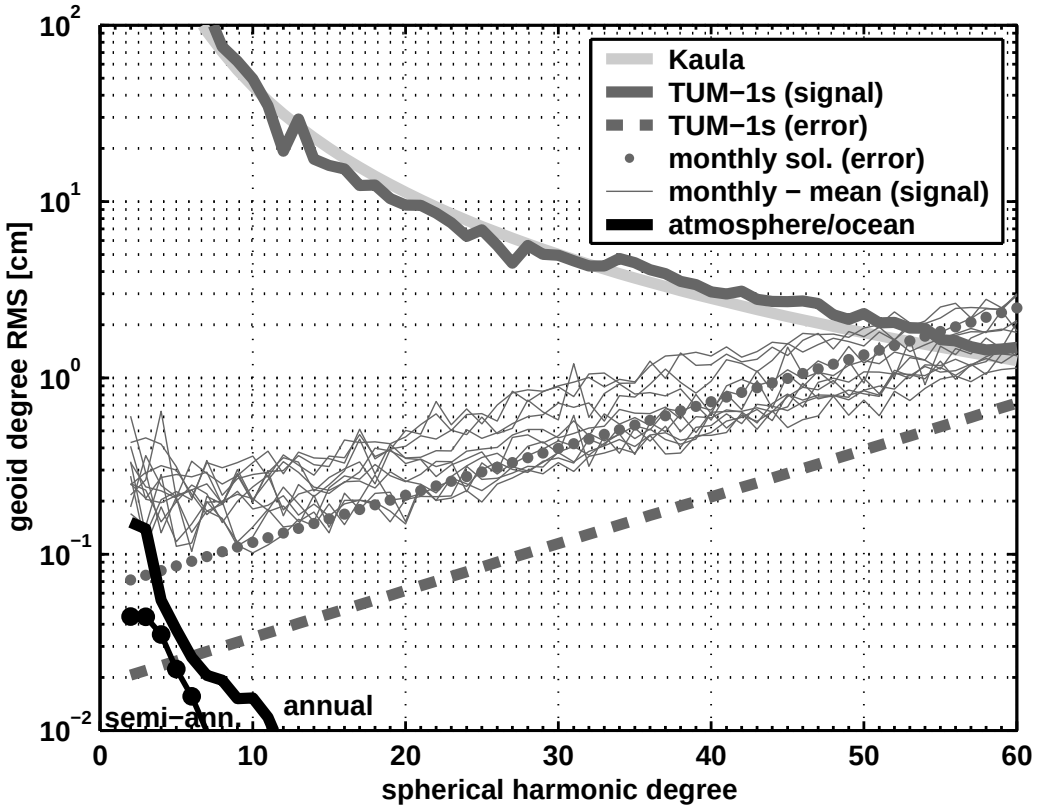

Figure 1.6: Monthly CHAMP signal and error spectra compared to TUM1s and to seasonal gravity signal from atmosphere and ocean

the results with seasonal gravity variations from SLR solutions. In their study TUM1s, which was the predecessor of TUM2s, represents the static field in the period of interest.

For comparison, the signal spectra of the annual and semi-annual atmospheric/oceanic signal is shown in figure 1.6. Most geophysical signal spectra are below the CHAMP error level. The error level of the monthly CHAMP solutions is insufficient for revealing these time variations. Orbit decay and consequently the groundtrack variation is one of the main contributors to the loss of accuracy. The problem is that one tries to recover a time-variable gravity field from a time-variable geometry and the influence on the monthly solution is neither well understood nor do any techniques exist to circumvent or reduce this dependency.

With the advent of GRACE however, CHAMP has been outperformed in terms of accuracy and many discontinued the data processing. Using a classical method, Tapley et al. (2004a) derived the first gravity field from GRACE (GGM01s) using preliminary data from the commissioning phase[1]. The early results indicated that they are better by one order of magnitude than the CHAMP results. The important thing about GRACE is that it gives these accurate results every thirty days. By differencing these monthly snapshots the time-variable part of the gravity field can be recovered, see e.g., Wahr et al. (2004). The results were improved in the following time and additional gravity field models, like the GGM02s and the EIGEN-CG01C, were published (Reigber et al., 2004). The new results are improved further but, as in the case of CHAMP, the results are still not as good as predicted. Especially the very low coefficients, like J_2, seem to be problematic but also the overall accuracy is still below the expectations. Since the orbit is similar to CHAMP and no drag-free system is installed the satellite system is slowly decaying and the problem is again that one tries to recover a time-variable gravity field from a time-varying geometry.

The energy balance approach can be extended for the case of low-low SST. One of the first to discuss this in satellite geodesy was Wolff (1969). He connected the difference of the potential in two orbit locations to the range-rate between the two satellites. Thus he introduced a satellite configuration which is more sensitive to the medium and short wavelength structure of the gravity field but his derivations were

[1]Phase of the initial power-up and evaluation of the science instrument system

also based on approximations. First test results were obtained in the ATS-6/GEOS-3 and the ATS-6/Apollo-Soyuz experiment. Gravity anomalies with ≈ 3 mGal accuracy and a wavelength of $500 - 1000$ km were derived (Vonbun, 1977). Several theoretical discussions and investigations using simulated data exist, as well. Jekeli (1999) derived the energy balance approach for the case of GRACE in the inertial frame but it is still based on the approximation suggested by Wolff, though it is applied to residuals.

Another specific property of the two satellite missions is that the satellites have an almost polar orbit, which yields a higher data density due to convergence near the pole. The missions provide new and vital information on the geoid and the gravity field of the polar regions itself. The new data is beginning to yield the highly accurate geoid, which is needed for Arctic oceanographic and sea ice studies. CHAMP- and GRACE-based geoids could have the accuracy required to detect, in combination with satellite altimetry, the poorly known dynamic topography of the Arctic Ocean (McAdoo et al., 2005). Garcia (2002) discussed the application of the GRACE data for local geoid determination using simulated data and showed that an improvement compared to global models in these areas is possible.

An additional area of interest will be Canada. The newest official geoid for Canada is the Canadian Gravimetric Geoid model 2000 (CGG2000) (Véronneau, 2001). It uses the Helmert-Stokes condensation method and geoid heights are computed from gravimetric measurements using the Stokes integral. The contribution for the long-wavelength part comes from EGM96, which is a pre-CHAMP model. It is obvious that the far more accurate data from CHAMP and GRACE should be implemented.

1.4 Thesis objectives

CHAMP. The primary task for the case of CHAMP is the reprocessing of the available kinematic data and the refinement of the data processing steps. It includes the development of a proper calibration procedure, which takes the physical properties of an accelerometer into account. The aim is an improvement of the low degree signal,

which is especially important for the investigation of time variability. In addition, the influence of the changing orbit geometry on the observables and on the modelling needs to be investigated. Since CHAMP is a single satellite mission it can be investigated more easily than in case of a multi-satellite mission but understanding of the dependency on the orbit geometry is equally important for GRACE.

GRACE. The first task for the case of GRACE is the application of the energy balance approach in the Earth-fixed frame, thus introducing an alternative but equivalent way to the method of Jekeli (1999). Additionally and more importantly, the work aims at the derivation of an exact relation between the gravitational potential and the K-band measurement. The refined concept needs to be validated with simulated data, and its applicability with real GRACE data is to be tested.

High latitude areas. In order to make optimal use of the data distribution in high latitude areas, two different interpolation methods will be investigated, namely the weighted mean interpolation and the least-squares prediction. The former yields fast results and is often used as a gridding tool before the application of FFT-techniques. The latter is a computationally expensive tool but can be combined with downward continuation. This is the first step towards a highly accurate geoid model for Canada and the Arctic regions, which will support the development of new gravimetric models and the investigation of geophysical phenomena in these areas.

1.5 Research methodology - Thesis outline

The research comprises three parts. The first one discusses the reprocessing of the CHAMP data and investigates the dependency on the geometry of the satellite orbit, cf. chapter 4. The second part aims at the application of the energy balance approach to GRACE (chapter 5). The final part discusses the two interpolation techniques for the derivation of local geoids in high-latitude areas (chapter 6). The classical setup of describing the theory in the first part, followed by numerical results is relinquished

here on purpose. For the sake of clarity, global and local applications for each satellite mission are discussed separately.

The thesis starts with a brief review of the theoretical foundations of gravity field representation in chapter 2. For validation purposes, spectral representations are of major importance. They are introduced for standard deviations of the spherical harmonic coefficients as well as difference error spectra with respect to a known model. Extensive use of the later will be made in chapters 4 and 5.

Chapter 3 introduces tools which are of importance for both satellite missions, globally as well as locally. These definitions, transformations, models and procedures enable the application of the energy balance approach. It starts with the transformation of time systems and the new transformation between the Earth-fixed and inertial system according to the IERS conventions (McCarthy and Petit, 2003). The accelerometer data needs to be transformed from the space-body frame to the inertial frame. For this, quaternions are available but data gaps need to be interpolated. Due to the nature of quaternions, a special interpolation technique is necessary and the spherical linear interpolation is introduced in section 3.3. Kinematic orbits only yield positions, and thus velocities need to be derived numerically. Two different approaches are discussed in terms of accuracy and applicability. Finally, tides cannot be recovered from the two satellite missions and their proper reduction is an important step in the data processing.

The energy balance approach for the high-low satellite-to-satellite tracking case is introduced in chapter 4 and investigated in terms of accuracy requirements. Two years of kinematic and accelerometer data is used to derive the global gravity model UofC using a least-squares adjustment. The solution incorporates a refined calibration technique, which is introduced in section 4.2.2, and is validated in the spatial and spectral domain. Monthly solutions and the influence of the groundtrack pattern are investigated. Aiming at an improvement of the data distribution, the two GRACE satellites are considered as CHAMP-like satellite. The combination technique and the results are discussed in section 4.3.

Chapter 5 extends the energy balance approach to the case of two satellites in the

low-low satellite-to-satellite tracking mode and introduces an exact relation between the kinetic energy term and the K-band measurement. The concept is validated with simulated data and its feasibility is discussed with real GRACE data.

The local investigations are based on the pointwise measurements of CHAMP in high latitude areas. First, the weighted mean interpolation and the least-squares prediction for the interpolation of data at satellite height is discussed in section 6.2. Finally, the concept of least-squares prediction can be extended to include downward continuation yielding results on the surface, cf. section 6.3.

Chapter 7 summarizes the achievements of this thesis and gives recommendations for future work.

Chapter 2

Fundamentals of the gravitational theory

Gravitational acceleration is described by Newton's law of gravitation. The dominating feature of this vector field can be represented by a rotating and oblate sphere (=ellipsoid). The flattening of the Earth results in a higher attraction at the pole than at the equator. However, the aim of the gravity field determination from satellite tracking missions is to recover small deviations from this basic ellipsoidal model caused by a wide range of mass inhomogeneities (Rummel et al., 2002). Additionally, mass transportation yields a time variation of the gravitational attraction. For this, a mathematical representation on the sphere will be necessary, which is introduced in this section.

2.1 Representation and linearization of the gravitational potential

The starting point is, whether the gravitational field can be determined from measurements on and outside the Earth without the knowledge of its density structure. The two input parameters for the determination are the measurements on or outside the boundary and the knowledge of the spatial behavior described by partial differential equations. This type of problem is called a Boundary Value Problem (BVP). In our particular case, the measurements cannot be taken on the boundary since it is by itself unknown. This type of BVP is known as the *geodetic boundary value problem*.

The behavior outside the boundary is described by the Laplace equation:

$$\Delta V = \nabla^2 V = 0, \tag{2.1}$$

where V is the gravitational potential of the Earth, Δ is the Laplace and ∇ the Nabla[1] operator. Any representation of V must fulfill this equation. The Laplace operator

[1] vector of the first partial derivatives

corresponds to the sum of the diagonal elements of the tensor of the second order partial derivatives of V, which is physically a measure for the divergence of the gravity field. The divergence indicates the sources and sinks in a vector field. If it is equal to zero, the field contains neither of them and is called a harmonic one.

Since the gravitational field of the Earth is a harmonic function outside the Earth, it can be expressed as a spherical harmonic (SH) function (Heiskanen and Moritz, 1967):

$$V(r,\theta,\lambda) = \frac{GM}{R}\sum_{l=0}^{\infty}\left(\frac{R}{r}\right)^{l+1}\sum_{m=0}^{l}\left(\bar{C}_{lm}\cos m\lambda + \bar{S}_{lm}\sin m\lambda\right)\bar{P}_{lm}(\cos\theta), \tag{2.2}$$

where G is the gravitational constant, M the mass of the Earth, R the radius, r, θ and λ the coordinates of the calculation point, $\bar{P}_{lm}$ the normalized Legendre functions and $\bar{C}_{lm}$ and $\bar{S}_{lm}$ the normalized dimensionless spherical harmonic coefficients. The indices of the double summation are the degree l and the order m. The infinite summation is in reality truncated at a maximum degree L yielding an *omission* error.

If the density distribution of the Earth is known, the coefficients can be calculated by integration over all mass elements $d\sigma$ according to:

$$\left.\begin{matrix}\bar{C}_{lm}\\ \bar{S}_{lm}\end{matrix}\right\} = \frac{1}{M}\frac{1}{2l+1}\iiint_{\sigma}\left(\frac{r}{R}\right)^{l}\rho\bar{P}_{lm}(\cos\theta)\left\{\begin{matrix}\cos m\lambda\\ \sin m\lambda\end{matrix}\right\}d\sigma, \tag{2.3}$$

where ρ is the density of the mass element. Note that it is more convenient to use the normalized Legendre function and spherical harmonic coefficients. The relation to the non-normalized version of the two is given as:

$$P_{lm}(\cos\theta) = N_{lm}^{-1}\,\bar{P}_{lm}(\cos\theta) \tag{2.4}$$

$$\left.\begin{matrix}C_{lm}\\ S_{lm}\end{matrix}\right\} = N_{lm}\left\{\begin{matrix}\bar{C}_{lm}\\ \bar{S}_{lm}\end{matrix}\right. . \tag{2.5}$$

The normalization factor is given as:

$$N_{lm} = \sqrt{(2-\delta_{m0})(2l+1)\frac{(l-m)!}{(l+m)!}}. \tag{2.6}$$

Adding the centrifugal potential

$$Z = \frac{1}{2}\omega^2 r^2 \sin^2\theta \tag{2.7}$$

to the gravitational potential V yields the gravity potential W

$$W = V + Z. \tag{2.8}$$

From section 1.2 it is known already that the gravity field W can be split into a normal (ellipsoidal) model part U and the disturbing potential T:

$$W = U + T. \tag{1.1}$$

Geodetic observables are normally connected to gravity field quantities by nonlinear relations. Introducing the normal field is part of a linearization step using a Taylor series which is truncated after the linear term. The normal potential is defined to have the following properties:

- rotational symmetry;
- equatorial symmetry; and
- be constant on the ellipsoid.

Since the normal potential is also a harmonic function, it can be expanded in a SH-series as well. Due to the first property of rotational symmetry, only zonal coefficients need to be taken into account. Equatorial symmetry reduces the series to even degrees only. Restricting the development to degree $L = 8$, the spherical harmonic series simplifies to:

$$U(r,\theta) = \frac{GM}{R} \sum_{l=0,[2]}^{8} \left(\frac{R}{r}\right)^{l+1} \sum_{m=0}^{l} \bar{c}_{l,0} \bar{P}_l(\cos\theta), \tag{2.9}$$

where $\bar{P}_l(\cos\theta)$ is the Legendre polynomial of degree l. The spherical harmonic coefficients $\bar{c}_{l,0}$ are derived from the GRS80 constants (Moritz, 1980b).

Subtracting the normal field from the gravity field yields a spherical harmonic expression for the so-called disturbing potential T:

$$T(r,\theta,\lambda) = \frac{GM}{R} \sum_{l=0}^{\infty} \left(\frac{R}{r}\right)^{l+1} \sum_{m=0}^{l} \left(\Delta\bar{C}_{lm} \cos m\lambda + \Delta\bar{S}_{lm} \sin m\lambda\right) \bar{P}_{lm}(\cos\theta), \tag{2.10}$$

where $\Delta\bar{C}_{lm} = \bar{C}_{lm} - \bar{c}_{lm}$ and $\Delta\bar{S}_{lm} = \bar{S}_{lm}$. The quantity T cannot be observed directly. Instead, in terrestrial measurements the so-called gravity anomalies Δg can be observed using gravimeters. The fundamental equation of physical geodesy connects the measured quantity with the disturbing potential:

$$\Delta g = -\frac{\partial T}{\partial r} - \frac{2}{r}T. \tag{2.11}$$

For measurements on the Earth's surface, r is equal to the Earth radius R. The calculation can be performed on any level outside the Earth, thus making this equation also fundamental for satellite applications. The objective of dynamical satellite geodesy is the determination of the Earth's gravitational field using observations to or of space-borne vehicles. In the case of CHAMP and GRACE the satellites act as a test mass on the one hand and as a measurement platform on the other hand. Instead of gravity anomalies, positions, velocities, accelerations and differences of these quantities are measured. Chapter 4 and 5 will introduce the *energy balance approach* which connects these observables to T. The approach will yield the disturbing potential along the orbit at the instantaneous location of the satellite. The spherical harmonic coefficients can be derived by:

$$\left.\begin{matrix}\bar{C}_{lm} \\ \bar{S}_{lm}\end{matrix}\right\} = \frac{1}{4\pi}\frac{R}{GM}\iint_{\sigma}\left(\frac{r}{R}\right)^{l+1} T\left(r,\theta,\lambda\right)\,\bar{P}_{lm}\left(\cos\theta\right)\left\{\begin{matrix}\cos m\lambda \\ \sin m\lambda\end{matrix}\right\} d\sigma. \tag{2.12}$$

Equation (2.12) is generally referred to as spherical harmonic analysis. Equations (2.2) and (2.10) are known as spherical harmonic synthesis. Certainly, the spherical harmonic representations are not restricted to the disturbing potential only. Using their eigenvalues any of the gravitational functionals can be represented by a spherical harmonic series (Rummel and van Gelderen, 1995).

2.2 Spectral error representation

When it comes to the validation and discussion of the spherical harmonic analysis spatial as well as spectral comparisons are useful. Spectral representation of the signal

and the noise can be two-dimensional or one-dimensional. These quantities will be used intensively in the discussion of the global solutions in section 4 and 5.

2.2.1 Two-dimensional error spectrum

The spherical harmonic coefficients are two-dimensional quantities which are either derived in a least-squares adjustment or from quadrature. As output, the covariance matrix of the unknowns $Q_{\hat{x}\hat{x}}$ might be available. Taking the diagonal elements, the variance of the coefficients can be represented but correlations are neglected.

$$\operatorname{diag}\left(Q_{\hat{x}\hat{x}}\right) = \left\{ \begin{array}{ll} \operatorname{VAR}\left\{\bar{C}_{lm}, \bar{C}_{lm}\right\} & m \geqslant 0 \\ \operatorname{VAR}\left\{\bar{S}_{lm}, \bar{S}_{lm}\right\} & m < 0 \end{array} \right\} = \sigma_{lm}^2 \tag{2.13}$$

Similar to the error spectrum, the difference between two signal spectra can be used:

$$\Delta_{lm} = \left\{ \begin{array}{ll} \bar{C}_{lm}^{\text{new}} - \bar{C}_{lm}^{\text{old}} & m \geqslant 0 \\ \bar{S}_{lm}^{\text{new}} - \bar{S}_{lm}^{\text{old}} & m < 0 \end{array} \right. \tag{2.14}$$

The advantage of the latter is that it can also be used when $Q_{\hat{x}\hat{x}}$ is not available. Moreover, comparison with external data is possible. The variance, on the other hand, represents the internal accuracy of the estimation.

2.2.2 One-dimensional error spectrum

The most common way to determine a one-dimensional error spectrum from spherical harmonic coefficients is to derive degree-specific components. The first one to be mentioned is the *error degree variance*:

$$\sigma_l^2 = \sum_{m=-l}^{l} \sigma_{lm}^2 \qquad \forall \quad l \,\epsilon\, [2 \ldots L]\,. \tag{2.15}$$

The summation in this case is from $-l$ to l, where the negative degrees denote the sine and the positive the cosine coefficients. The error degree variance represents the total error power in the coefficients and is a quadratic quantity. In order to derive an average standard deviation for the coefficients of a specific degree l, the error degree variance

can be divided by the number of coefficients $(2l+1)$ and the square root can be taken. The result is the root mean square of the error spectrum per degree:

$$\text{RMS}_l = \sqrt{\frac{\sigma_l^2}{2l+1}} = \sqrt{\frac{1}{2l+1}\sum_{m=-l}^{l}\sigma_{lm}^2}. \tag{2.16}$$

The RMS_l is a representative standard deviation only if the error spectrum is isotropic, i.e., it is independent of the order m. Order specific components can also be derived but do not have any physical meaning. They might be useful for weighting purposes and can reveal patterns in the spectrum.

2.2.3 Cumulative error spectrum

It might also be of interest to see the cumulative error which contains all the error power up to a certain degree. It is also called *commission error*.

$$\text{CUM}_l = \sqrt{\sum_{i=2}^{l}\sigma_i^2} = \sqrt{\sum_{i=2}^{l}\sum_{m=-l}^{l}\sigma_{im}^2}. \tag{2.17}$$

Due to the nature of the spherical harmonic coefficients, the error is unitless. More interesting is the comission error for any given gravitational functional f, which can be derived from (2.17) and the Meissl-scheme (Rummel and van Gelderen, 1995):

$$\text{CUM}_l\,(f) = \sqrt{\sum_{i=2}^{l}\lambda_i^2\sigma_i^2}, \tag{2.18}$$

where λ is the eigenvalue of f. For example, in order to derive the comission error in geoid height, λ is equal to the Earth radius R. Thus it represents the noise in the functional due to noise in the coefficients.

2.2.4 Relative error spectrum

Two relative error spectra measures are available, namely *gain* and *signal-to-noise ratio* (SNR). Both can be used with either the error spectrum or the difference spectrum.

Here, both are mainly used as one-dimensional error spectra, i.e., expressed per degree. They may also be expressed for each coefficient individually.

The gain describes the ratio between the error or the difference between two coefficients:

$$g_{lm}^{\sigma} = \frac{\sigma_{lm}^{\text{old}}}{\sigma_{lm}^{\text{new}}} \qquad g_{lm}^{\Delta} = \frac{\Delta_{lm}^{\text{old}}}{\Delta_{lm}^{\text{new}}}. \tag{2.19}$$

As one-dimensional quantity, the gain describes the ratio between the error or difference curves of two models:

$$g_{l}^{\sigma} = \frac{\sigma_{l}^{\text{old}}}{\sigma_{l}^{\text{new}}} \qquad g_{l}^{\Delta} = \frac{\Delta_{l}^{\text{old}}}{\Delta_{l}^{\text{new}}}. \tag{2.20}$$

If one of the error spectra has a larger content than the other, the signal curve of the bigger one takes the role of the missing part of the error curve. This means that the expectation of the coefficients is zero and their variance equals the signal variance model (Sneeuw, 2000). The ratio is usually expressed on a logarithmic scale, i.e., a value of zero represents the same error level. Values above zero indicate an improvement whereas values below describe a degradation.

The signal-to-noise ratio in the two-dimensional case is the ratio between the signal coefficient and the noise or difference coefficient

$$\text{SNR}_{lm}^{\sigma} = \begin{cases} \frac{\bar{C}_{lm}}{\sigma_{lm}} & m \geqslant 0 \\ \frac{\bar{S}_{lm}}{\sigma_{lm}} & m < 0 \end{cases} \qquad \text{SNR}_{lm}^{\Delta} = \begin{cases} \frac{\bar{C}_{lm}}{\Delta_{lm}} & m \geqslant 0 \\ \frac{\bar{S}_{lm}}{\Delta_{lm}} & m < 0 \end{cases}. \tag{2.21}$$

The one-dimensional counterpart is expressed as the ratio between the signal curve and the noise or difference curve

$$\text{SNR}_{l}^{\sigma} = \frac{\sqrt{c_l}}{\sigma_l} \qquad \text{SNR}_{l}^{\Delta} = \frac{\sqrt{c_l}}{\Delta_l} \tag{2.22}$$

where c_l is the signal degree variance, which can be calculated as the sum over all degrees of the signal spectrum:

$$c_l = \sum_{m=0}^{l} \left(\bar{C}_{lm}^2 + \bar{S}_{lm}^2\right)$$

It is normally expressed on a logarithmic scale. A value of one represents the crossing point between the signal and the noise curve, which determines the maximum solvable

degree L. In practice, the signal curve might not cross the noise curve but rather merge with it after a transition zone. In this case, the crossing with a model curve, e.g., Kaula or Tscherning-Rapp, might be used instead in order to determine L.

Chapter 3

Transformations, numerical differentiation and tides

This chapter describes all the background models and transformations necessary in order to derive successfully the disturbing potential along the orbit using the energy balance approach that will be introduced in chapter 4. It starts with a description of the transformations between time systems in use in section 3.1. They are also important for the transformation between reference frames. Chapter 3.2 introduces the new transformation between the celestial and the terrestrial frame according to the IERS conventions. It adopts the IAU2000A precession and nutation model and takes polar motion and the variable Earth rotation into account.

The equally important quaternion transformation is described in section 3.3. It enables the transformation from the satellite frame to the inertial frame. The usage of kinematic orbits requires the numerical differentiation of position data, and two different approaches are discussed in section 3.4.

Tides introduce a time-variable gravity signal that would be an objective of the gravity field recovery. For the gravity field missions CHAMP and GRACE however, the tide signals will act as noise to the measurements or cause aliasing. Their proper reduction is an important step towards the recovery of time-variable gravity signals. Tides are a gravitational signal by nature and the relevant theory should be in chapter 2 but here its usage as a reduction tool before the actual gravity field recovery is emphasized and thus it is part of this chapter.

3.1 Transformation of time systems

The overview is restricted to the transformation of the time systems used in the calculations. For details and other time systems the reader is referred to Müller (1999), Torge (2001) or Seeber (2003). Figure 3.1 summarizes the transformation between all

necessary time systems.

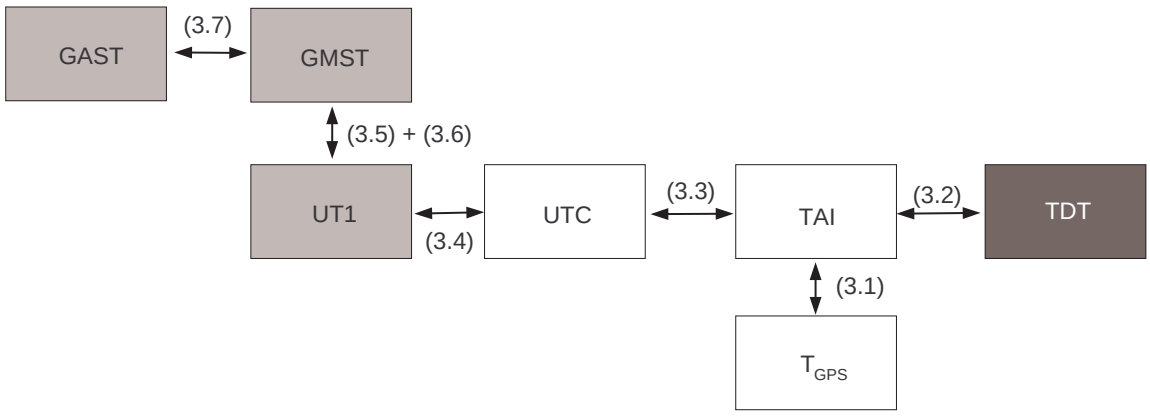

Figure 3.1: Transformation between time systems (Müller, 1999)

One basic time system is the International Atomic Time (TAI = Temps Atomique International). It provides a uniform and highly accurate time-scale and is based on the definition of the SI second. The primary system used in the calculations is the GPS time T_{GPS}, which is provided with the position and velocity data. It is connected to the atomic time TAI by a constant offset:

$$TAI = T_{\mathrm{GPS}} + 19\,\mathrm{s}, \tag{3.1}$$

which is the number of leap seconds at the time of its introduction on 06.01.1980, 0^{h} UTC. The GPS time is based on numerous atomic clocks of its ground and space segment. Each satellite is equipped with four clocks that are connected to the coordinated time scale of the US Naval Observatory with its 73 caesium clocks and 12 hydrogen maser. It is counted in terms of GPS weeks, which start on Sunday at $0^{\mathrm{h}}00^{\mathrm{m}}00^{\mathrm{s}}$ GPS time.

The atomic time systems are complemented on the one hand by time systems based on the Earth rotation and on the other hand by time systems based on the motion of celestial bodies in the solar system. The Terrestrial Dynamic Time (TDT) belongs to the latter group and is referred to the geocenter. It is a strictly uniform time scale for the calculations of ephemeris data of celestial and artificial satellites. The difference

between TAI and TDT is constant:

$$TDT = TAI + 32.184\,\mathrm{s}. \tag{3.2}$$

Celestial bodies have impact on the transformation between the celestial and the terrestrial reference frame, and TDT is needed for the calculation of the precession-nutation model, cf. section 3.2.

The connection to time systems based on the Earth rotation is implemented by the Universal Time Coordinated (UTC). It is a constant timescale like TAI but kept close to the mean solar day ($UT1$) by the application of leap seconds.

$$UTC = TAI + N = TAI + 32\,\mathrm{s} \text{ (for the period of interest)} \tag{3.3}$$

The data used throughout this thesis covers the period from April 2002 to February 2004; N is equal to 32 s during this period. The mean solar day is denoted with $UT1$ and the difference between $UT1$ and UTC is constantly monitored. If it becomes larger than 0.9 s, another leap second is introduced.

$$\Delta UT = UT1 - UTC \tag{3.4}$$

The precise corrections ΔUT for every day can be interpolated from the *EOPC04* data file of the IERS (2002).

For the calculation of tidal accelerations, the Greenwich Mean and Apparent Sidereal Times ($GMST$, $GAST$) are needed. They describe the mean and true hour angle of the Greenwich meridian with respect to mean and true vernal equinox, respectively. The transformation from the mean solar time to the mean sidereal time is equivalent to a change of the reference from the sun to the vernal equinox:

$$GMST = \alpha - 12^{\mathrm{h}} + UT1, \tag{3.5}$$

where α is the right ascension of the sun:

$$\begin{aligned} \alpha = 18^{\mathrm{h}}41^{\mathrm{m}}50.54841^{\mathrm{s}} &+ 8640184.812866\,{}^{\mathrm{s}}/_{\mathrm{JC}} \cdot (T - T_0) \\ &+ 0.093104\,{}^{\mathrm{s}}/_{\mathrm{JC}^2} \cdot (T - T_0)^2 \\ &- 0.0000062\,{}^{\mathrm{s}}/_{\mathrm{JC}^3} \cdot (T - T_0)^3 . \end{aligned} \tag{3.6}$$

The reference epoch T_0 is *J2000.0* and the time T is counted in Julian centuries (JC). The linear term corrects for precession. The quadratic and cubic term correct for the secular influence of the planets. The difference of apparent and mean time is termed the *Equation of Equinoxes*:

$$GMST - GAST = \Delta\psi \cos\epsilon, \tag{3.7}$$

where $\Delta\psi$ is the nutation correction in longitude and ϵ the obliquity of the ecliptic.

3.2 Transformation between celestial and terrestrial reference frame

On its 24$^{\text{th}}$General Assembly in 2000 the International Astronomical Union (IAU) adopted several resolutions, which allow the transformation between the Celestial Reference System (CRS) and the Terrestrial Reference System (TRS) with an accuracy at the microarcsecond (mas) level. The transformation of the observation at the epoch t can be written as:

$$\mathbf{r}_{\text{CRS}} = Q(t)R(t)W(t)\mathbf{r}_{\text{TRS}}, \tag{3.8}$$

where $Q(t)$, $R(t)$ and $W(t)$ are time dependent rotation matrices.

$W(t)$ accounts for the polar motion. The modified polar coordinates x_P and y_P are obtained by taking the polar coordinates provided by the IERS and adding the effects of ocean tides and nutation with periods less than two days. After the $W(t)$ rotation, the z-axis points to the Celestial Intermediate Pole (CIP). The concept is an extension of the formerly used Celestial Ephemeris Pole (CEP) which did not take diurnal and higher frequency variations of the Earth rotation into account. With $W(t)$, the x-axis is moved on the moving equator from the instantaneous x-axis and to the Terrestrial Ephemeris Origin (TEO). The second rotation matrix $R(t)$ uses the negative Earth rotation angle θ and the x-axis is moved to the Celestial Ephemeris Origin (CEO) as shown in figure 3.2(b). The frame generated by these two rotations is called the intermediate reference frame at epoch t.

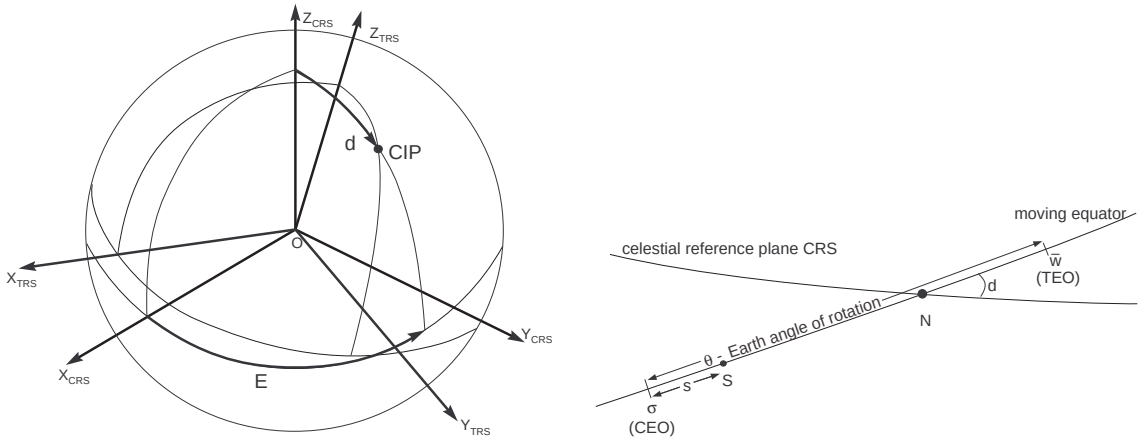

(a) Coordinates of the CIP

(b) CEO, TEO, Earth angle of rotation

Figure 3.2: Relation between CIP, TEO and CEO

The rotation $Q(t)$ continues to move the x-axis to the point S and rotates the frame from the CIP to the celestial reference frame. At the core of this transformation is the new IAU2000 precession-nutation model. Two versions of the model are available. IAU2000A provides the highest accuracy of about 0.2 mas, while the shorter version IAU2000B is precise to only 1 mas. Both models provide the coordinates X and Y which do not have a physical meaning, but they can be transformed into the coordinates d and E which can be visualized as in figure 3.2(a). The new transformation was adopted beginning 1stJanuary, 2003, and replaces the precession-nutation model based on the "IAU 1976 Precession and the IAU 1980 Theory of Nutation". Modern Very Long Baseline Interferometry (VLBI) observations had revealed that it was not adequate any more.

3.3 Transformation using quaternions

The second important type of rotation is the quaternion transformation. The accelerometer data is usually given in the Space Body Frame (SBF) which is connected to the satellite body. The attitude data of the SBF with respect to the CRS is determined from

the star sensor onboard the satellites. The rotation angles are expressed in terms of quaternions, which is a four dimensional vector:

$$q = (q_0, q_1, q_2, q_3) = (q_0, \boldsymbol{q}) \,. \tag{3.9}$$

It can be divided into a scalar part q_0 and a vectorial part $\boldsymbol{q}$. Their theory is based on complex numbers and was developed by Sir William Rowan Hamilton (1805–1865). The quaternions in use are restricted to *unit length*, i.e., their degree of freedom is also restricted to three (Hanson, 2006).

$$q \cdot q = q_0^2 + \boldsymbol{q} \cdot \boldsymbol{q} = 1 \tag{3.10}$$

In order to apply the transformation to three-dimensional vectors, the quaternions can be transformed to a rotation matrix as follows:

$$\begin{aligned} \boldsymbol{x}' &= \boldsymbol{R}(q) \cdot \boldsymbol{x} \\ \boldsymbol{R}(q) &= \begin{pmatrix} q_0^2 + q_1^2 - q_2^2 - q_3^2 & 2q_1q_2 - 2q_0q_3 & 2q_1q_3 + 2q_0q_2 \\ 2q_1q_2 + 2q_0q_3 & q_0^2 - q_1^2 + q_2^2 - q_3^2 & 2q_2q_3 - 2q_0q_1 \\ 2q_1q_3 - 2q_0q_2 & 2q_2q_3 - 2q_0q_1 & q_0^2 - q_1^2 - q_2^2 + q_3^2 \end{pmatrix} \end{aligned} \tag{3.11}$$

The quaternions can also be applied directly to the vector $\boldsymbol{x}$, but for this the quaternion conjugation (3.12) and the quaternion multiplication (3.13) needs to be defined:

$$\bar{q} = (q_0, -q_1, -q_2, -q_3) = (q_0, -\boldsymbol{q}) \tag{3.12}$$

$$p * q = \begin{pmatrix} p_0q_0 - \boldsymbol{p} \cdot \boldsymbol{q} \\ p_0\boldsymbol{q} + q_0\boldsymbol{p} + \boldsymbol{p} \times \boldsymbol{q} \end{pmatrix} \tag{3.13}$$

The three dimensional rotation is then given as:

$$\begin{pmatrix} 0 \\ \boldsymbol{x}' \end{pmatrix} = q * \begin{pmatrix} 0 \\ \boldsymbol{x} \end{pmatrix} * \bar{q} \tag{3.14}$$

The attitude data is not as complete as the accelerometer data, since the Sun and the Moon blind the star sensors every once in a while. Consequently, interpolation between two quaternions $q(t_0)$ and $q(t_1)$ is necessary. Linear interpolation (LERP) will result in

a nonconstant angular velocity and in general quaternions will loose their unit length. They can be renormalized; thus forces the interpolation points to be on the unit sphere (cf. figure 3.3(a)) but the uneven angular spacing is inherent. Instead the spherical

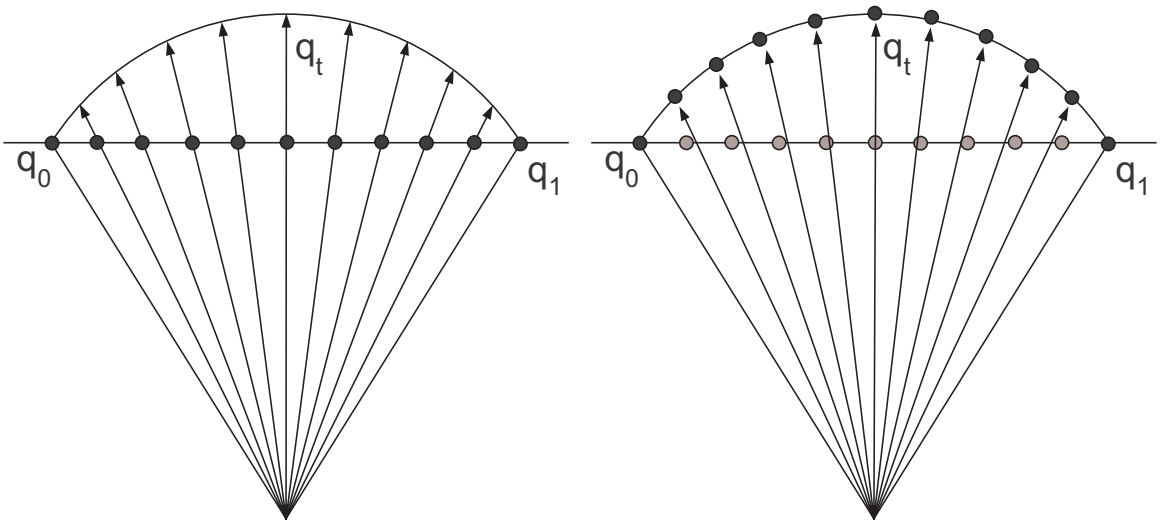

(a) linear interpolation (b) spherical linear interpolation

Figure 3.3: Linear vs. spherical linear interpolation of quaternions, from Hanson (2006)

linear interpolation (SLERP) is introduced, which guarantees the interpolation points to lie on the unit circle and to maintain constant angular velocity. The difference of the constant angular velocity (black points) with respect to the linear interpolation (gray points) is illustrated in figure 3.3(b). The quaternion for any arbitrary time t between the quaternion $q(t_0)$ and the quaternion $q(t_1)$ is given as:

$$q(t) = q(t_0)\frac{\sin(1-t)\phi}{\sin\phi} + q(t_1)\frac{\sin t\phi}{\sin\phi}, \tag{3.15}$$

where $\cos\phi = q(t_0) \cdot q(t_1)$ is the inner product of the two quaternions. For the definition of the inner product and a detailed derivation, see Hanson (2006). The SLERP interpolator keeps the vector at time t in the mutual plane of the two limiting vectors and guarantees the transformation of one unit vector into another.

3.4 Numerical Differentiation

In the calculations, purely kinematic CHAMP orbits are used in order to avoid the contamination of the solution with *a priori* gravity field information. The data is provided by Drazen Švehla from the Technical University Munich (Švehla and Rothacher, 2004). They are derived using a zero-difference approach and are independent of the satellite dynamics and the orbit characteristics. The disadvantage is that kinematic orbit determination yields only positions, and velocities have to be derived by numerical differentiation. The ideal differentiator can be described by the spectral transfer function $H\left(e^{i\omega T}\right)$ (Antoniou, 1979):

$$H\left(e^{i\omega T}\right) = i\omega \quad \text{for} \quad 0 \leqslant |\omega| < \frac{\omega_s}{2} \tag{3.16}$$

where ω is the frequency, ω_s is the sampling frequency and i the imaginary number. It represents the angle bisection of the first and third quadrant as shown in figure 3.4. Note that the frequency axis is already adapted to the case of CHAMP, i.e., the sampling frequency ω_s is equal to $1/30$ Hz. In the following, two methods are presented which are both approximations of the ideal differentiator. The approximation is desired, since differentiators act as a high-pass filter and tend to amplify noise. By adjusting the properties of each method, the amplification of noise in the data can be minimized. Further details can be found in Weigelt and Sneeuw (2004).

3.4.1 FFT Method

The first method presented here utilizes a Fast Fourier Transformation (FFT) approach. The idea is to determine the spectral content of the signal, i.e., of the position, and multiply the result with $i\omega$ or any suitable approximation of it. After back-transformation to the time domain, the signal represents the velocities. The advantage of the approach is the easy application and modification of the differentiator itself. The drawback is that problems with leakage, aliasing and data gaps arise. The latter cause problems in the transformation and need to be filled with dynamic position data or by interpolation.

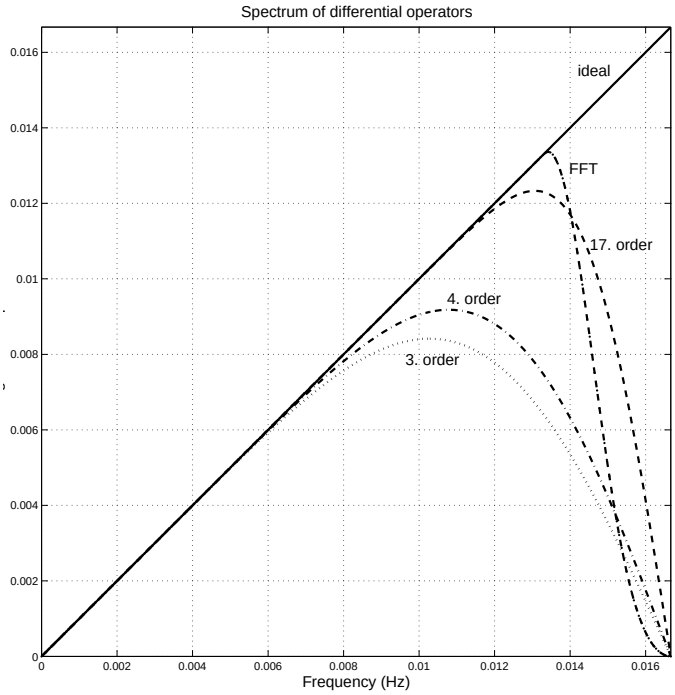

Figure 3.4: Spectral transfer of differentiators

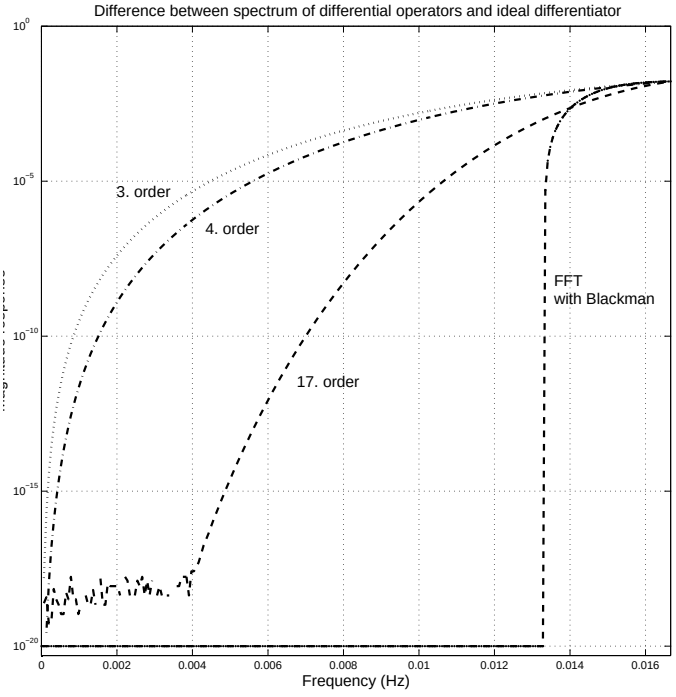

Figure 3.5: Difference to the ideal differentiator

This is a major drawback of the approach since high frequencies due to jumps between the kinematic and dynamic positions are introduced.

Leakage is caused by a finite number of measurements, which corresponds to a multiplication of the infinite signal with a boxcar function. The multiplication leads to a convolution of the spectrum with the spectrum of a boxcar function, i.e., the sinc-function. Windowing techniques are used in order to minimize leakage, but applying a window results in major differences at the edges of the data since the data is continuously downweighted towards zero. In order to minimize this effect, data before and after the desired area of interest should be added. Since the number of frequencies in the spectral domain is also finite, it can also be seen as a multiplication of an infinite spectrum with a boxcar function and the corresponding time domain function is again convolved with the sinc-function. Therefore, a window should also be applied to the differentiator in the frequency domain in order to minimize the sidelobes of the corresponding time domain function. The advantage is that this window will also act as a low-pass filter, and therefore, gives control over the amplification of the noise.

In practice, the calculation is performed on a daily basis. For each day, one complete day of data is added before and afterwards. Half of these are used to apply the window. The differentiator is used complete up to $\approx 80\%$ of the frequency content (figure 3.4), and a Blackman window is applied (Lyons, 1997) in the stopband between 0.013 Hz and the Nyquist frequency.

The top panel in figure 3.6 shows results with noiseless simulated data for CHAMP which were developed by the IAG Special Commission SC7 (Ilk, 2001). The data is created using numerical integration with the EGM96 model up to degree and order 300. For the validation of the approach, the position of the satellite is differentiated and compared to the simulated velocity. Note that the difference is at the level of $10^{-3}\,\mathrm{mm/s}$ for the simulated data. Computations with position and velocity data provided by the IAPG, TU Munich (Švehla and Rothacher, 2004), are shown in the middle panel of figure 3.6. The data is derived using a reduced dynamic approach, i.e., the dynamics are reduced by geometrical information. For an exten-

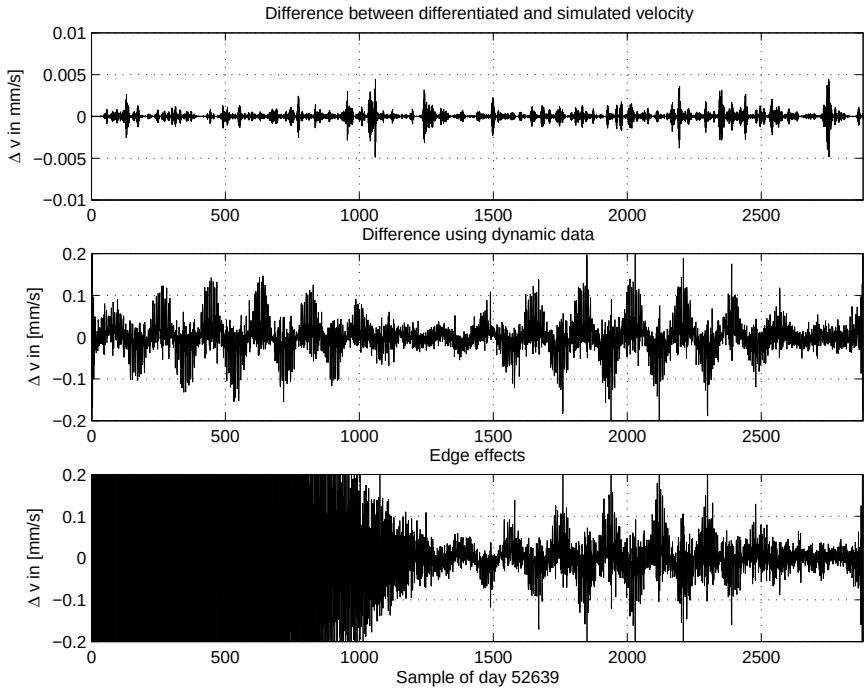

Figure 3.6: Test results: simulated data (top), real dynamic data (middle), edge effect (bottom)

sive overview over the different type of data the reader is referred to the webpage of Drazen Švehla (`http://tau.fesg.tu-muenchen.de/~drazen/`), which contains numerous publications about the methods used to derive kinematic, dynamic, reduced kinematic and reduced dynamic data. The dynamic data has the advantage that velocities can be derived as well, thus a more realistic test scenario than with simulated data is achieved. Since the data contains noise, the simulated results are overoptimistic and two orders of magnitude in accuracy are lost due to the noise. For the gravity field recovery, an error level of 1 dm in geoid height is aspired for CHAMP which corresponds to an minimum accuracy of $0.14\,{}^{\mathrm{mm}}/_{\mathrm{s}}$ in the velocity (see section 4.1.2). The results are at this level but the data availability was ideal, which means that there was enough data before and after the timespan of interest available for the usage of the windowing technique. The lower panel shows the edge effect, which occurs when a major data gap exists and/or filling with dynamic position data is not possible. Valuable data is lost.

In the case of CHAMP, approximately 1500 samples are necessary to reach the level of 0.14 mm/s. With its 30 second data sampling, this means a loss of data of 8 revolutions or half a day, which is unacceptable.

The second problem is the global behavior of the approach. Changes due to orbit maneuvers or sudden changes in the environment are aliased over the whole interval of calculation. In practice, this means that the differentiator causes up to one day delay in the reaction to these events and contaminates data before these events.

3.4.2 FIR Method

The FFT method uses multiplication in the frequency domain, which is identical to a convolution in the time domain. Therefore, the differentiator can be implemented as a Finite Impulse Response (FIR) filter. The design of the filter is based on a central finite difference Taylor approximation of the first derivative (Bruton et al., 1999), the so-called Taylor differentiator. It is applied by convolving the signal with the filter coefficients f_k:

$$y_i = \sum_{k=-n}^{n} f_k \cdot x_{i-k}, \tag{3.17}$$

where n is the order of the differentiator. The coefficients of n^{th} order can be calculated in a fast and effective way using closed-form expressions (Khan and Ohba, 1999). Knowing that a convolution in the time domain is equivalent to a multiplication in the frequency domain, the methodology is practically identical to the FFT method except that the filter is designed and applied in the time domain. For the calculation of one value, only $2n + 1$ data elements for a n^{th} order differentiator are necessary, i.e., the delay is equal to the order n and the differentiator responds quickly to changes in the environment or due to orbit maneuvers. The edge effect still exists but is much smaller than in the case of FFT. For a n^{th} order differentiator, n elements at the beginning and at the end of an area of interest are lost. The smaller the order of the differentiator, the smaller will the edge effect be. The filling with dynamic position data becomes unnecessary, if a reasonably small order is used for the differentiator and this leads to a more

rigorous data treatment. Thus, the usage of a FIR filter overcomes the two obstacles of the FFT method but at the cost of a restricted freedom in the design of the filter (Antoniou, 1979). On the other hand, it is necessary to use a reasonably high order to achieve results better than the level of 0.14 mm/s. Figure 3.5 shows the difference of several differentiators to the ideal differentiator and obviously the approximation becomes better with increasing order. The FFT differentiator naturally is identical with the ideal differentiator in the passband but the sharp transition effect due to the Blackman window is clearly visible. The Taylor differentiators have a much longer transition zone, which is a disadvantage in the application to noisy data. A filter with a sharper transition could also be designed in the time domain, which leads to the usage of the so-called equiripple or least-squares differentiators but normally a much higher order is necessary than in the case of the Taylor differentiator and the advantage compared to the FFT approach is partially lost. The task is, therefore, to choose the *minimum possible* and *maximum necessary* order; naturally, this choice will depend on the frequency content of the signal.

Several differentiators with different orders have been tested. Figure 3.7 shows results with simulated data and clearly demonstrates that the order of the differentiator and thus the approximation of the ideal differentiator influences the accuracy of the solution. The higher the order, the better the result. Figure 3.8 shows test results performed with reduced dynamic data and there is virtually no difference between the three solutions. This is supported by the RMS values of the three solutions, which are all around 0.04 mm/s (cf. table 3.1). Note that only the dynamic data reaches this level. Kinematic data is even more noisy and the RMS will consequently be higher.

The conclusion is that in the case of CHAMP an order of three is sufficient. For completeness, it should be mentioned that an order less than three gives unacceptable results (e.g., RMS = 0.23 mm/s for order 2).

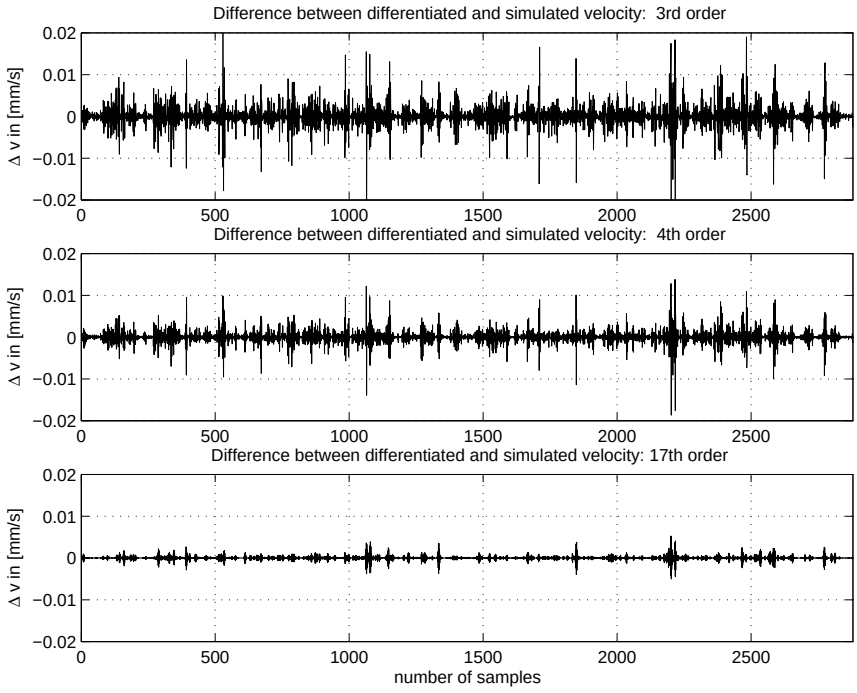

Figure 3.7: Test results with simulated data: 3rd order (top), 4th order (middle), 17th order (bottom)

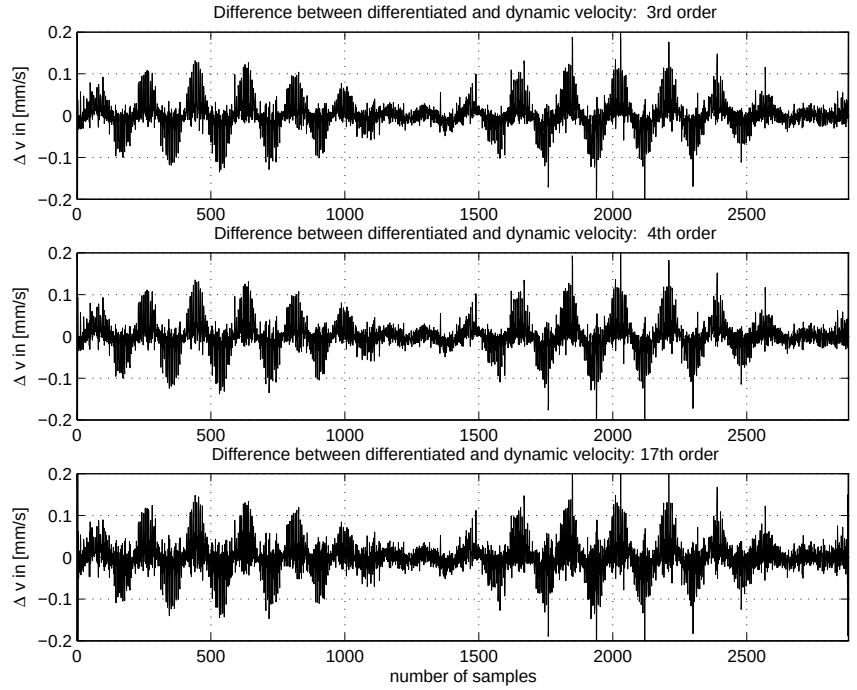

Figure 3.8: Test results with reduced dynamic data: 3rd order (top), 4th order (middle), 17th order (bottom)

order	RMS: simulated data	RMS: dynamic data
2	$0.18\,^{\mathrm{mm}}/_{\mathrm{s}}$	$0.23\,^{\mathrm{mm}}/_{\mathrm{s}}$
3	$0.01\,^{\mathrm{mm}}/_{\mathrm{s}}$	$0.04\,^{\mathrm{mm}}/_{\mathrm{s}}$
4	$5.43\,^{\mu\mathrm{m}}/_{\mathrm{s}}$	$0.04\,^{\mathrm{mm}}/_{\mathrm{s}}$
17	$2.33\,^{\mu\mathrm{m}}/_{\mathrm{s}}$	$0.05\,^{\mathrm{mm}}/_{\mathrm{s}}$

Table 3.1: RMS of the difference between differentiated positions and velocities for simulated and reduced dynamic data

3.5 Tides

Tidal deformations of the potential and forces on the satellite are primarily caused by the Sun and the Moon. The direct effect is referred to as *N-body perturbations* and can reach several decimeters in geoid height. Other planets, especially Jupiter and Saturn, also cause tidal effects which are several orders of magnitude smaller and usually neglected.

The Earth itself is not rigid and responds to the external force with displacement that, in turn, changes the potential. This effect is referred to as the *solid Earth tide*. *The ocean tides* take into account that the water masses react differently than the land masses to the forces. Both effects also cause a change in the pole axis and yield indirect effects which are known as *solid Earth pole tide* and *ocean pole tide*.

3.5.1 N-body perturbations

Assuming point masses for the disturbing body, the force on a satellite orbiting the Earth can be calculated as:

$$\ddot{\boldsymbol{r}}_j = Gm_j \left(\frac{\boldsymbol{r}_j - \boldsymbol{r}}{|\boldsymbol{r}_j - \boldsymbol{r}|^3} - \frac{\boldsymbol{r}_j}{|\boldsymbol{r}_j|^3} \right), \tag{3.18}$$

where G is the gravitational constant and m_j the mass of the disturbing bodies. The geocentric vectors $\boldsymbol{r}_j$ and $\boldsymbol{r}$ point to the disturbing body j and the satellite, respectively. Cartesian coordinates for the all major bodies in the solar system are available from

the Jet Propulsion Laboratory (JPL). The so-called "Development Ephemerides" (DE) are available in the versions DE200 and DE405. The DE200 include nutations, but no librations. The DE405 include both. The data is provided in the form of a Chebyshev approximation and can be interpolated to the time of interest (Montenbruck and Gill, 2000).

3.5.2 Solid Earth Tide

Since the Earth is not a rigid body, the astronomic tides will deform the Earth causing an additional effect on the potential. The effect can be approximated by (Seeber, 2003):

$$\ddot{\boldsymbol{r}} = \frac{k_2}{2}\frac{Gm_j}{r_j^3}\frac{R^5}{r^4}\left(3 - 15\cos^2\theta\right)\frac{\boldsymbol{r}}{r} + 6\cos\theta\frac{\boldsymbol{r}_j}{r_j}, \tag{3.19}$$

where k_2 is the Love number describing the elasticity of the Earth body, m_j the mass, r_j the distance and $\boldsymbol{r}_j$ the position vector of the disturbing body j from the geocenter, R the Earth radius, $\boldsymbol{r}$ and r the position vector and distance of the satellite from the geocenter, and θ the angle between the geocentric position vector of the satellite and the disturbing body.

The approximation is valid within $10\% - 20\%$ compared to the IERS conventions and can already be used for the case of CHAMP. For more precise calculations, the procedure of the IERS conventions (McCarthy and Petit, 2003, §6) should be followed. The variations are most conveniently expressed as corrections to the spherical harmonic coefficients. The computation is split into two parts.

In the first step, the frequency-independent part is calculated according to:

$$\Delta\bar{C}_{nm} = \frac{k_{nm}}{2n+1}\sum_{j=2}^{3}\frac{Gm_j}{GM}\left(\frac{R}{r_j}\right)^{n+1}\bar{P}_{nm}\left(\sin\Phi_j\right)\cos m\lambda_j \tag{3.20}$$

$$\Delta\bar{S}_{nm} = \frac{k_{nm}}{2n+1}\sum_{j=2}^{3}\frac{Gm_j}{GM}\left(\frac{R}{r_j}\right)^{n+1}\bar{P}_{nm}\left(\sin\Phi_j\right)\sin m\lambda_j, \tag{3.21}$$

where k_{nm} is the nominal Love number for degree n and order m, GM the gravitational parameter of the Earth and r_j, Φ_j and λ_j the geocentric distance, latitude and longitude, respectively. The rest of the notation is following equation (3.19). The summation is

restricted to $j = 2$ for the Moon and $j = 3$ for the Sun. The influence of other disturbing bodies is neglected. The degree 4 terms will have an additional correction due to the degree 2 tidal effect. Values for the nominal Love numbers k_{nm} can be found in McCarthy and Petit (2003, table 6.1).

The second step includes a frequency dependent correction from a number of tidal constituents depending on the respective band and the treatment of the permanent tide. The degree two zonal tide has a mean value, which is nonzero and yields a permanent deformation of the potential. Consequently, it has a time-independent contribution to $\bar{C}_{20}$. If the tidal corrections are applied according to the IERS conventions the resulting potential is a *conventional tide free model* as in the case of, e.g., EGM96. Care must be taken in the comparison of geopotential models. Some include the time-independent contribution and are referred to as "*zero tide*". Examples are the *JGM-3* and the GGM02s model.

3.5.3 Solid Earth Pole Tide

The solid Earth pole tide is caused by the polar motion, which generates a centrifugal effect and affects the geopotential coefficients $\bar{C}_{21}$ and $\bar{S}_{21}$. It can be calculated using

$$\Delta\bar{C}_{21} = -1.333 \cdot 10^{-9} \left(m_1 - 0.0115_2\right) \tag{3.22}$$

$$\Delta\bar{S}_{21} = -1.333 \cdot 10^{-9} \left(m_2 + 0.0115_1\right), \tag{3.23}$$

where m_1 and m_2 are in seconds of arc and describe the time dependent offset of the instantaneous rotation pole from the mean. For their determination the instantaneous polar coordinates x_p and y_p are subtracted from the mean pole (McCarthy and Petit, 2003, §7).

3.5.4 Ocean tide

The ocean tides are similarly modelled as the solid Earth tide as variations to the spherical harmonic coefficients. The modelling also follows the suggestions by the IERS

conventions (McCarthy and Petit, 2003, §6).

$$\Delta\bar{C}_{lm} = F_{lm} \sum_{s(l,m)} \bar{\sum_{+}} \left(C^{\pm}_{slm} \mp S^{\pm}_{slm}\right) \cos \pm\theta_s \tag{3.24}$$

$$\Delta\bar{S}_{lm} = F_{lm} \sum_{s(l,m)} \bar{\sum_{+}} \left(C^{\pm}_{slm} \mp S^{\pm}_{slm}\right) \sin \pm\theta_s \tag{3.25}$$

$$\text{with: } F_{lm} = \frac{4\pi G\rho_w}{g} \sqrt{\frac{(l+m)}{(l-m)(2l+1)\,(2-\delta_{lm})}} \left(\frac{1+k'_l}{2l+1}\right), \tag{3.26}$$

where ρ_w is the density of saltwater ($1025\,^{\mathrm{kg}}/_{\mathrm{m}^3}$), k'_l the load deformation coefficients and θ_s the argument of the tide constituent s. The coefficients $C^{\pm}_{slm}$ and $S^{\pm}_{slm}$ are gained by a spherical harmonic analysis of the ocean tide height caused by a specific constituent s of the tide generating potential. The variations in the spherical harmonic coefficients $\Delta\bar{C}_{lm}$ and $\Delta\bar{S}_{lm}$ of degree l and order m are then calculable by summation over all constituents s for retrograde (top sign) and prograde (bottom sign) waves. The effect of the ocean tides cannot be neglected for the CHAMP data processing, cf. figure 3.9, but the older Schwiderski model (Schwiderski, 1984) is already sufficient. For the GRACE processing, newer models like *CSR4.0* from Eanes (2002) or *FES2004* (Letellier, 2004) are mandatory for a proper dealiasing (Han et al., 2004). The ocean tide will also have an effect on the polar motion and thus introduces an effect similar to the

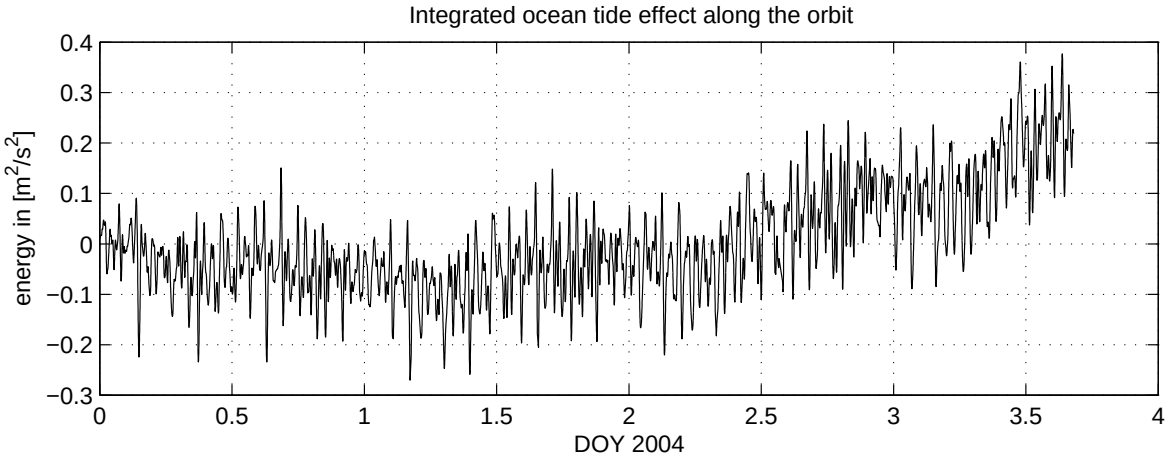

Figure 3.9: Integrated accelerations due to ocean tides along the orbit

solid Earth pole tide. The model for the latter is still under review and not yet part of the recommendations in the IERS conventions 2003 (McCarthy and Petit, 2003). It is about to be included in the near future and should be accounted for in the processing of GRACE data. For CHAMP, the effect is negligible.

3.6 Non-tidal variations of the atmosphere and oceans

For the proper analysis of a series of monthly gravity field solutions, short term mass variations in the atmosphere and oceans with periods smaller than one month need to be taken into account. Since the mission profile of CHAMP and GRACE do not allow an elimination by repeated observations within short periods, these effects need to be removed during the data processing. Han et al. (2004) showed also that the current atmospheric and ocean models are not sufficient for proper reduction and introduce an error in the global monthly geoid estimates. For this, the atmosphere and ocean dealiasing product AOD1B is introduced (Flechtner, 2005). It provides residual spherical harmonic coefficients every six hours, which can be interpolated and transformed into corresponding disturbing potential difference variations along the orbit.

Chapter 4

Global gravity field recovery from high-low satellite-to-satellite tracking

This chapter discusses in detail the gravity field recovery for the case of a single satellite mission using the energy integral. It starts in with its derivation in the Earth-fixed frame in section 4.1.1 and investigates its sensitivity to input quantities in section 4.1.2. With the approach the disturbing potential along the orbit can be derived, and a spherical harmonic analysis is subsequently necessary in order to derive global spherical harmonic coefficients. Section 4.2 starts with a detailed description of the data processing strategy for the case of CHAMP (section 4.2.1) and discusses the refined accelerometer calibration procedure in section 4.2.2. In the subsequent sections 4.2.3–4.2.5, the derived solutions are validated and the influence of the groundtrack variation on the solution is quantified and investigated. In order to minimize the effect of the data distribution, information from several satellite missions can be combined. Methodology and results for the combined case are discussed in section 4.3.

4.1 The energy balance approach

The *energy balance* approach, also referred to as the *energy integral* approach, is based on the law of energy conservation. It states that in a closed system the total energy is conserved. Energy itself can exist in a number of forms. The kinetic energy is connected to the motion of a mass, whereas the potential energy is a resultant of the spatial order of the elements of the system (Tipler, 1995). In case of a satellite system, the kinetic energy can be derived from the satellite's velocity. The potential energy relates to the gravitational field of the Earth and the distance between these two bodies. Remarkably, the mathematical framework for the energy balance approach was already developed in

the last century by the mathematician C. Jacobi (1804–1851) (Jacobi, 1836). Therefore, this approach is also referred to as *Jacobi integral* and it was considered for gravity field recovery purposes since the beginning of the satellite era (O'Keefe, 1957; Bjerhammer, 1967; Reigber, 1969; Jekeli, 1999). Its main advantage is its simplicity. Gravity field and orbit determination are separated in two subsequent steps. It avoids the initial state problem and enables the data processing on desktop computers. However, it relies on a precise orbit determination and, due to its integral nature, on long and uninterrupted time-series of velocity and accelerometer data. The lack of continuous data prevented the practical implementation for a long time. CHAMP data closed this gap for the first time due to the continuous GPS-tracking and the accelerometer measurements. It has been demonstrated by a number of groups that the derivation of a gravity field using this approach is qualitatively equivalent to the official CHAMP solutions EIGEN-1S and EIGEN-2S which are derived using classical methods, see Reigber (1989), Reigber et al. (2002, 2003), Gerlach et al. (2003b) and Han et al. (2002).

4.1.1 Derivation

The derivation of the energy integral starts from the equation of motion in the rotating frame (Schneider, 1992, §5.4). The basic steps are

1. the separation of static, time-variable and non-gravitational accelerations;
2. the substitution of accelerations by the gradient of the corresponding potential;
3. the multiplication with the velocity; and
4. the integration along the orbit.

In general, the derivation follows closely the one in Sneeuw et al. (2003) but time variable gravitational accelerations of known sources like, e.g., tides are handled differently here. All derivations are done per unit mass. The equation of motion in the Earth-fixed frame reads:

$$\ddot{\boldsymbol{x}} = \boldsymbol{a} - \boldsymbol{\omega} \times (\boldsymbol{\omega} \times \boldsymbol{x}) - 2\boldsymbol{\omega} \times \dot{\boldsymbol{x}} - \dot{\boldsymbol{\omega}} \times \boldsymbol{x}. \tag{4.1}$$

The acceleration $\ddot{\boldsymbol{x}}$ of a point mass on the left hand side is equal to all forces $\boldsymbol{a}$ acting on the mass minus the centrifugal acceleration $\boldsymbol{\omega} \times (\boldsymbol{\omega} \times \boldsymbol{x})$, the Coriolis acceleration $2\boldsymbol{\omega} \times \dot{\boldsymbol{x}}$ and the Euler term $\dot{\boldsymbol{\omega}} \times \boldsymbol{x}$. The position and velocity of the point mass in an Earth-fixed reference system are denoted by $\boldsymbol{x}$ and $\dot{\boldsymbol{x}}$. The Earth rotation rate and its change are denoted by $\boldsymbol{\omega}$ and $\dot{\boldsymbol{\omega}}$, respectively. In the following, the Euler term is neglected since the changes of the Earth rotation rate are of the order of $10^{-16}\,{}^{\mathrm{rad}}/_{\mathrm{s}^2}$ and can be assumed sufficiently constant.

The dynamic accelerations in equation (4.1) can be split into a static gravitational part $\boldsymbol{g}$, the sum of all time-variable gravitational accelerations $\sum_i \boldsymbol{g}_i$, and a non-gravitational part $\boldsymbol{f}$.

$$\boldsymbol{a} = \boldsymbol{g} + \sum_i \boldsymbol{g}_i + \boldsymbol{f} \tag{4.2}$$

The static gravitational component is the unknown in this problem and is the main subject of determination. The time-variable part consists on the one hand of parts which are known and on the other hand of all unknown time-variable gravitational effects. It is very important to take the time resolution into account. Currently, a common procedure to determine time-variable gravity field solutions is to derive monthly mean solutions and assume the data static within this month. It is obvious that any time-variable effect with a period lower than one month needs to be modelled in order to avoid aliasing effects, cf. Han (2004). A simple example are tidal effects with their daily and sub-monthly periods. Naturally, any errors in the model will cause aliasing as well.

For the time being let us follow the general idea of solving for monthly mean solutions and assume that every time-variable effect with a period smaller than one month can be sufficiently modelled or neglected. Therefore, $\sum_i \boldsymbol{g}_i$ in equation (4.2) consists only of all known time-variable gravitational effects, namely the astronomic, the solid Earth, the ocean and the solid Earth pole, which are described in section 3.5.

Non-gravitational forces like, e.g., solar radiation pressure or atmospheric drag can either be modelled or measured by the accelerometer onboard the satellite. A com-

prehensive overview about the modelling of non-gravitational forces and its interaction with the orbit parameters can be found in Milani et al. (1987). Here, we follow the second approach using the accelerometer measurements which make the satellite missions CHAMP and GRACE so unique. Hence the parameter $\boldsymbol{f}$ represents the accelerometer measurements.

Inserting equation (4.2) into equation (4.1) yields

$$\ddot{\boldsymbol{x}} = \boldsymbol{g} + \sum_i \boldsymbol{g}_i + \boldsymbol{f} - \boldsymbol{\omega} \times (\boldsymbol{\omega} \times \boldsymbol{x}) - 2\boldsymbol{\omega} \times \dot{\boldsymbol{x}} \tag{4.3}$$

The gravitational and centrifugal accelerations can be replaced by the gradient of the gravitational potential, ∇V, and of the centrifugal potential, ∇Z.

$$\ddot{\boldsymbol{x}} = \nabla V + \sum_i \boldsymbol{g}_i + \boldsymbol{f} + \nabla Z - 2\boldsymbol{\omega} \times \dot{\boldsymbol{x}} \tag{4.4}$$

The centrifugal potential can be calculated using equation (2.7). Equation (4.4) by itself can already be used for global gravity field recovery. This approach and its modifications is referred to as the acceleration approach, cf. Ditmar and van Eck van der Sluijs (2004); Reubelt et al. (2003). The advantage is that no integration is necessary and it was shown by several groups that the usage of the accelerometer data might not be necessary either. On the other hand, with the usage of kinematic positions a double differentiation is necessary in order to derive accelerations, which might lead to a higher amplification of noise in the data.

The next step is the scalar multiplication of equation (4.4) with the Earth-fixed velocity $\dot{\boldsymbol{x}}$. It yields the cancellation of the Coriolis term since this term is perpendicular to the cross product of the Earth rotation rate and the velocity vector.

$$\dot{\boldsymbol{x}} \cdot \ddot{\boldsymbol{x}} = \dot{\boldsymbol{x}} \cdot \nabla V + \dot{\boldsymbol{x}} \cdot \nabla Z + \dot{\boldsymbol{x}} \cdot \left(\boldsymbol{f} + \sum_i \boldsymbol{g}_i \right) \tag{4.5}$$

The scalar multiplication of the gradient of any potential Φ with the velocity can be deduced from the total derivative of the potential:

$$\begin{aligned} \frac{d\Phi}{dt} &= \underbrace{\frac{\partial \Phi}{\partial \boldsymbol{x}} \cdot \frac{\partial \boldsymbol{x}}{\partial t}}_{\nabla\Phi \cdot \dot{\boldsymbol{x}}} + \frac{\partial \Phi}{\partial t} \\ \Rightarrow \dot{\boldsymbol{x}} \cdot \nabla\Phi &= \frac{d\Phi}{dt} - \frac{\partial \Phi}{\partial t}, \end{aligned} \tag{4.6}$$

where $\frac{\partial \Phi}{\partial t}$ denotes the explicit time-variable part of the potential. As discussed before, we assume all time-variable parts to be taken into account by using $\sum_i \boldsymbol{g}_i$ or be negligible within one month.

This is one of the key steps of this approach. Due to the evaluation of the energy integral in the Earth-fixed frame $\frac{\partial V}{\partial t}$ becomes 0. The explicit time derivative of the centrifugal potential $\frac{\partial Z}{\partial t}$ also becomes 0, but in this case due to the assumption of a constant Earth rotation rate $\boldsymbol{\omega}$.

Doing the integration on the left hand side analytically and inserting into equation (4.5) yields

$$\frac{1}{2}\dot{\boldsymbol{x}}^{\boldsymbol{T}}\dot{\boldsymbol{x}} + c = V + Z + \int \left(\boldsymbol{f} + \sum_i \boldsymbol{g}_i \right) d\boldsymbol{x} \tag{4.7}$$

The left hand side can easily be recognized as the kinetic energy E^{kin} of a unit mass plus an integration constant c. Note also that the integration over time of a quantity that is multiplied by the velocity is equivalent to the integration along the orbit.

Splitting the gravitational potential V into a normal gravitational and a disturbing part $V = U + T$ and rearranging for the unknown disturbing potential gives the basis of the gravity field recovery — the energy balance approach.

$$T + c = E^{\text{kin}} - U - Z - \int \left(\boldsymbol{f} + \sum_i \boldsymbol{g}_i \right) d\boldsymbol{x} \tag{4.8}$$

Figure 4.1 gives an overview about the magnitude of each term (left panel) and the contribution to the disturbing potential (right panel). Each plot shows the corresponding energy for two revolutions or a period of approximately 3 hours.

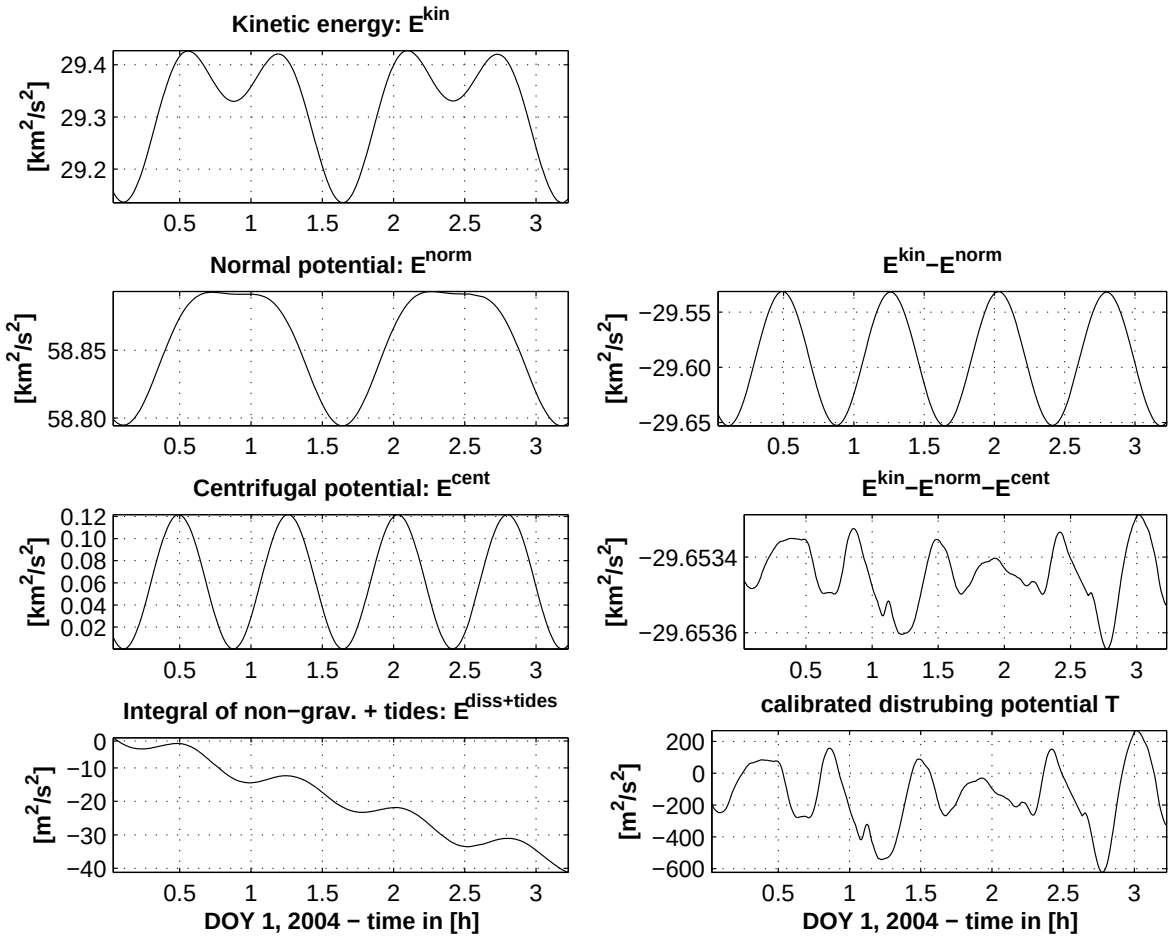

Figure 4.1: Magnitude of each energy term and contribution to the disturbing potential

The kinetic energy E^{kin} is at the level of approximately $30\,\mathrm{km^2/s^2}$ and shows primarily a 1 cycle per revolutions (CPR) signal, which is superimposed by a 2-CPR signal. The 1-CPR signal is related to the ellipsoidal shape of the Earth and is reduced by subtracting the normal field. The normal potential is derived from the position of the satellite and additional parameters (e.g., textscwgs84). The difference is not fluctuating around 0 but has an offset of approximately $29.6\,\mathrm{km^2/s^2}$. This gives already an idea about the magnitude and the effect of the integration constant c, which is also referred to as the *Jacobi constant*. It needs to be determined before or during a spherical harmonic analysis. Here, the constant is determined in a calibration procedure by a least-squares adjustment (cf. 4.2.2). Its application will center the disturbing potential around the

zero-line as the definition of the disturbing potential demands.

Sometimes it is suggested to subtract a mean value instead. However, this accounts for a continuous field only. The situation in a satellite orbit is different. The mean value of an orbit segment is not necessarily zero (cf. figure 4.1). For sufficiently long arcs, i.e., for several days, and a dense groundtrack coverage, the mean value would converge against the zero mean. In reality, such long arcs are usually not available due to data gaps and it is better to determine the difference to an *a priori* field over a continuous segment of the orbit in the calibration procedure.

The reduction reveals the 2-CPR signal, which is about 2 orders of magnitude smaller than the kinetic energy and normal potential. This signal is related to the centrifugal potential and can be modelled using the position of the satellite and the Earth rotation rate. Since the satellite is sensing the potential in an ascending orbit arc as well as in a descending orbit arc, the resulting signal has a frequency of 2-CPR. After reduction, the general shape of the disturbing potential along the orbit is already visible.

For the short period of two revolutions, the effect of the tides and the non-gravitational forces is barely visible, especially since the signal is 4 orders of magnitude smaller than the other energies. Nevertheless, their reduction is a very important step in the derivation. Only then the principle of energy balance is fulfilled. Non-gravitational forces are derived from the accelerometer data and velocity measurements of the satellite. Tides are calculated from the time and the position of the Sun, the Moon and the satellite. The bias in the accelerometer data yields a drift as shown in the lower left panel of figure 4.1 and needs to be removed in the calibration procedure.

The difference to the derivation in Sneeuw et al. (2003) is that the accelerations $\boldsymbol{g}_i$ are not integrated analytically to their corresponding potentials but integrated along the orbit. Gerlach (2003) showed that this is necessary since the models for these potentials do not take their temporal variations into account.

The final product is the disturbing potential along the orbit, which can be continued downward to the Earth surface and decomposed into spherical harmonic coefficients. It should be noted that the derivation can be done in a similar way in an inertial

reference frame (Jekeli, 1999). The result is the same but the individual energy terms have different meaning and magnitude.

4.1.2 Error analysis

The core component of the energy balance approach is the separation of orbit and gravity field determination, i.e., position and velocity determination are considered here as a preprocessing step. The disturbing potential along the orbit is derived using the integral and a spherical harmonic analysis is applied in order to decomposed the signal into spherical harmonic coefficients. In every step, the measurement errors need to be propagated, e.g., Niemeier (2001):

$$\Sigma_{yy} = A\,\Sigma_{xx}\,A^T, \tag{4.9}$$

where A is the Jacobi matrix of a linear or linearized system $\boldsymbol{y} = A\boldsymbol{x}$ and Σ_{xx} and Σ_{yy} are the covariance matrices of the input and the output, respectively. This means that measurement errors need to be propagated first into position and velocity errors, then into errors of the disturbing potential along the orbit and finally into standard deviations of the spherical harmonics.

The usage of the full covariance matrix of the GPS-observations is obviously a computationally very demanding task. For a single day and a data sampling of 30 s, the matrix has already the size of 8640×8640 samples. Each sample consumes 8 bytes of memory, which results in an overall memory usage of 569 MB just to store the matrix. Fortunately, it seems that the matrix is mainly block-diagonal due to correlations between observation points. These correlations depend likely on the ambiguity resolution, which forms a block structure for periods of fixed ambiguity (D. Švehla, personal communication). This correlation is the reason for the high accuracy of the positions and velocities, respectively. For a simple example, the reader is referred to Austen and Reubelt (2000, §8). However, since the usage of the full covariance matrix is not workable due to its size and an error model is not available, the best way is either to use just the main diagonal of the covariance matrix or to assume the measurement to

be of equal accuracy and the errors to behave like white noise. Practical experience has shown that this is a reasonable assumption.

The objective of the error analysis here is to estimate the sensitivity of the output quantity $\boldsymbol{y}$ on the input quantities, i.e.: *How precise do we need to know a certain quantity in order to reach a certain accuracy of the final product?* For this, the total differential towards all input quantities is built.

Firstly, the relevant input quantities need to be defined. Obviously position, velocity and accelerometer data are the most important quantities. Other quantities are either defined ones, like, e.g., GM or the Earth radius R, or assumed to be negligible like, e.g., errors in the position of Sun and Moon in tidal models. Additionally, the effect of position errors of the satellite in the tidal models is neglected here, as well. The total differential of the energy integral is given as:

$$dT = \frac{\partial T}{\partial \|\dot{\boldsymbol{x}}\|}\, d\|\dot{\boldsymbol{x}}\| + \frac{\partial T}{\partial \|\boldsymbol{x}\|}\, d\|\boldsymbol{x}\| + \frac{\partial T}{\partial \|\boldsymbol{f}\|}\, d\|\boldsymbol{f}\| \tag{4.10}$$

Instead of using the three dimensional coordinates, the vectors are replaced with their length and errors in the length, respectively. Furthermore, in order to simplify the situation, each of the components of the energy integral is discussed separately. In general, an accuracy at the dm-level for the geoid height ($\approx 1\,\mathrm{m^2/s^2}$ in the disturbing potential) is anticipated for single satellite missions like CHAMP.

Kinetic energy. The partial derivative for the kinetic energy term is given as:

$$\frac{\partial T}{\partial \|\dot{\boldsymbol{x}}\|} = \frac{\partial E^{\mathrm{kin}}}{\partial \|\dot{\boldsymbol{x}}\|} = \|\dot{\boldsymbol{x}}\| \tag{4.11}$$

Solving the first term in equation (4.10) for $d\|\dot{\boldsymbol{x}}\|$ yields an estimate for the necessary accuracy in the velocity. It is illustrated in figure 4.2. The x-axis shows the aspired error in the disturbing potential; the y-axis the corresponding accuracy demand on the velocity determination. The dm-level geoid is approximately equal to a $1\,\mathrm{m^2/s^2}$ level in terms of the disturbing potential. Consequently, in order to reach this, an accuracy in the velocity of $\approx 0.1\,\mathrm{mm/s}$ is necessary, which is at the edge of the achievable accuracy by numerical differentiation from kinematic positions (cf. section 3.4).

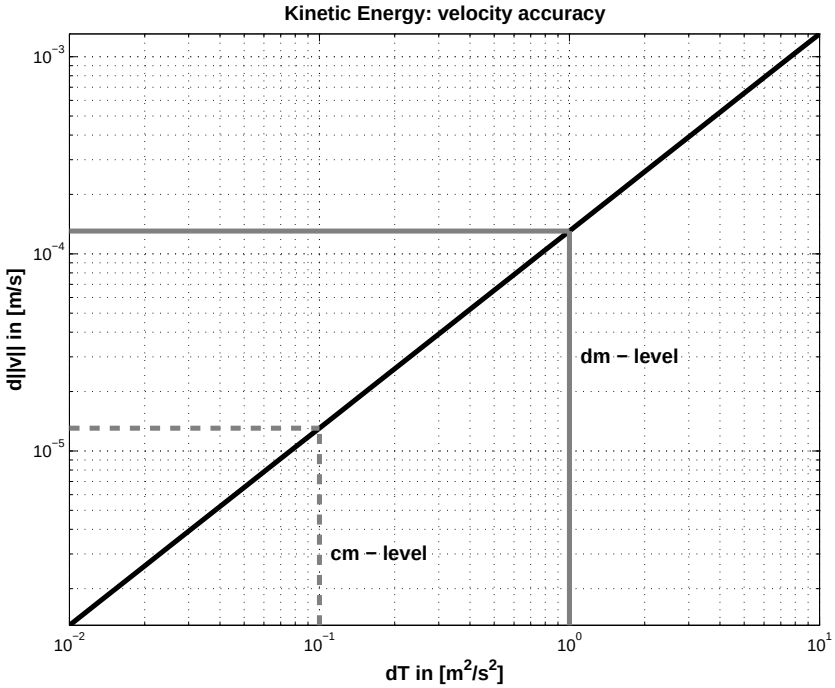

Figure 4.2: Error analysis of the kinetic energy term using $\|\dot{\boldsymbol{x}}\| = 7.7\,\mathrm{km/s}$ and $r = 6778\,\mathrm{km}$

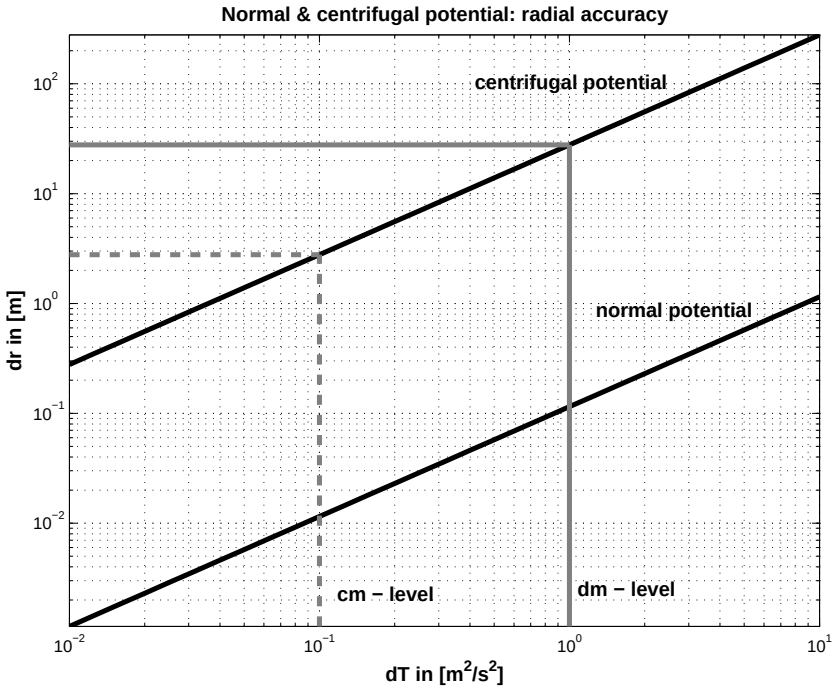

Figure 4.3: Error analysis of the normal & centrifugal energy term using $\|\dot{\boldsymbol{x}}\| = 7.7\,\mathrm{km/s}$ and $r = 6778\,\mathrm{km}$

Normal potential. The normal part of the energy integral is calculated from a spherical harmonic analysis of the even zonal terms till degree 8. For simplicity, only the degree 0 and degree 2 terms are taken into account in the error analysis . The normal potential is then given as:

$$U = \frac{GM}{r}\left[1 - J_2\left(\frac{R}{r}\right)^2 P_2\left(\sin\phi\right)\right], \tag{4.12}$$

where GM is the gravitational constant multiplied with the mass of the Earth, r the radius of the satellite, J_2 the unnormalized cosine coefficient of degree 2 and order 0, R the Earth radius and $P_2\left(\sin\phi\right)$ the Legendre polynomial of degree 2 which depends on the latitude ϕ. The partial derivative towards the radius r is given as:

$$\frac{\partial U}{\partial r} = -\frac{GM}{r^2}\left[1 - 3J_2\left(\frac{R}{r}\right)^2 P_2\left(\sin\phi\right)\right] \tag{4.13}$$

For the radius, an accuracy of 1 dm in the geoid height demands an accuracy of 1 dm in position. The kinematic positions of the IAPG, TU Munich, are provided with an accuracy of $2-5$ cm (Švehla and Rothacher, 2004), i.e., the accuracy demand is fulfilled by the provided data, cf. figure 4.3.

Certainly, there is also a dependence of the error in the normal potential on the latitude. For a dm-level accuracy in geoid height, the latitude must be known with an accuracy better than one arcsec which is equivalent to a position accuracy of 60 m on satellite height. Considering that cm-precision is provided by the kinematic orbit, this condition is fulfilled.

Centrifugal potential. The centrifugal term is also shown in the same figure and the situation is even more relaxed than in the case of the normal potential. An accuracy of several meters is sufficient. For completeness, the partial derivative of the centrifugal potential is given as:

$$\frac{\partial Z}{\partial r} = \omega^2 r \tag{4.14}$$

Dissipative energy. The integration of the non-gravitational forces $\boldsymbol{f}$ along the orbit can be expressed as an integration over time and a scalar multiplication of $\boldsymbol{f}$ with the velocity $\dot{\boldsymbol{x}}$. The scalar multiplication of the two vectors can be rewritten as the multiplication of the magnitude of the accelerometer and the velocity with the cosine of the angle between the two vectors. Using the Cauchy-Schwarz inequality the maximum effect can be derived:

$$E^{\text{diss}} = \int \boldsymbol{f} \cdot \dot{\boldsymbol{x}} \, dt = \int \|\boldsymbol{f}\| \, \|\dot{\boldsymbol{x}}\| \cos\phi \, dt \leqslant \int \|\boldsymbol{f}\| \, \|\dot{\boldsymbol{x}}\| \, dt \tag{4.15}$$

Taking the partial derivative with respect to $\|\boldsymbol{f}\|$ yields the integration of the magnitude of the velocity over time. The magnitude has an average of approximately 7650 $^{\text{m}}/_{\text{s}}$ and a variation of ± 15 $^{\text{m}}/_{\text{s}}$.

$$\frac{\partial E^{\text{diss}}}{\partial \|\boldsymbol{f}\|} = \int \|\dot{\boldsymbol{x}}\| \, dt \tag{4.16}$$

The average of the magnitude will cause a drift after integration as shown in the left panel of figure 4.4 for one day. Since the accelerometer bias will also cause a drift and a calibration procedure is applied on a daily basis (cf. section 4.2.2) to remove this error,

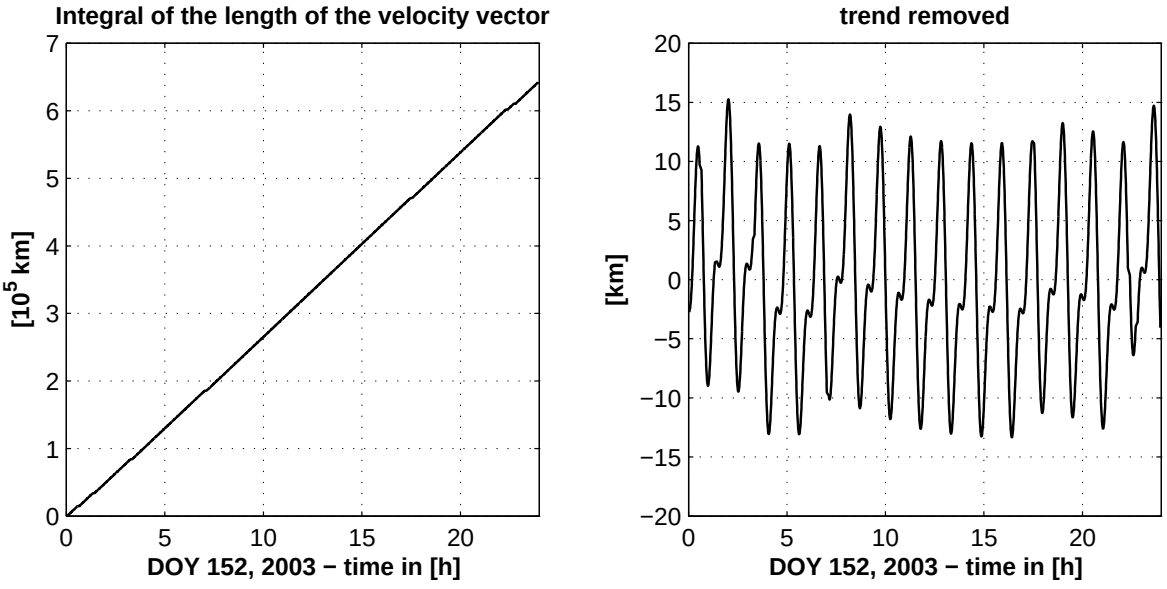

Figure 4.4: Integral of the length of the velocity vector (left panel) and after removal of the trend (right panel)

the drift caused by the velocity will be removed as well. The important point for the error analysis is the variation of the integral after detrending. The variation is shown in the right panel of figure 4.4 to be up to $\pm 15\,\mathrm{km}$ per day.

For a dm-level in geoid height an accuracy in the accelerometer measurement of $\approx 6{\cdot}10^{-5}\,\mathrm{m/s^2}$ is necessary. The accuracy of the CHAMP mission accelerometer is specified as $\leqslant 3 \cdot 10^{-9}\,\mathrm{m/s^2}$ (Touboul et al., 1998). Thus the accelerometer easily fulfills the necessary requirements to derive a dm-level geoid. It is emphasized that the error estimate is only valid if the bias and a scale are removed properly in a calibration procedure. Otherwise, the error can contaminate the results and yield a severe degradation of the spherical harmonic coefficients.

In summary, the error analysis showed that the restricting factor in the gravity field recovery using the energy balance approach will be the kinetic energy term and thus the velocity determination. For every other term, the provided position and accelerometer data is precise enough to reach the expected dm-level geoid accuracy or even better.

4.2 Global spherical harmonic analysis by least-squares adjustment

The energy balance approach yields the disturbing potential pointwise along the orbit. The term "in situ data" is also in use. The advantage is that the method can be used for global as well as for local gravity field solutions. This section will focus on the global part and aims at the spherical harmonic analysis. In section 4.2.1 the data processing steps are described starting with the reading of the raw data and finishing with a least-squares adjustment to derive the spherical harmonic coefficients. Section 4.2.2 will focus on the accelerometer calibration. Although it is part of the processing chain, it is discussed in a separate section since a refinement of the procedure led to a sub-centimeter accuracy in the cumulative geoid error for very low degrees.

The results of the spherical harmonic analysis are discussed in section 4.2.3. CHAMP

was expected to provide time-variable gravity field information on a monthly basis already. Sneeuw et al. (2005) showed among others that this was not possible using CHAMP-only solutions and suggested the variable groundtrack pattern besides accuracy itself as the main reason. This is investigated in section 4.2.4 and extended to the mapping of spectral content in section 4.2.5.

4.2.1 Data processing strategy

For the calculation of spherical harmonic coefficients from position, velocity and accelerometer data using the energy integral, the data handling is conveniently split into three parts:

1. data reading;
2. application of the energy principle; and
3. analysis.

All these steps are implemented by the author during the preparation of the thesis. For this, more than 30000 lines of Matlab code have been developed. The data comes from three different data sources (see figure 4.5), namely the Institute for Astronomical and Physical Geodesy (IAPG), TU Munich, the International Earth Rotation Service (IERS) and the GeoForschungsZentrum Potsdam (GFZ).

Reading. Kinematic and dynamic positions and dynamic velocities are provided by the Institute for Astronomical and Physical Geodesy (IAPG), TU Munich (Švehla and Rothacher, 2004). Positions and velocities are given in an Earth-fixed coordinate system and both are transformed to the inertial frame (cf. section 3.2). The data is time-stamped using GPS-time, which is also provided in the files and used as the time reference throughout the calculations.

Earth Orientation Parameters (EOP) are read from the long term Earth orientation data "`EOPC04`" provided by the International Earth Rotation Service (IERS, 2002).

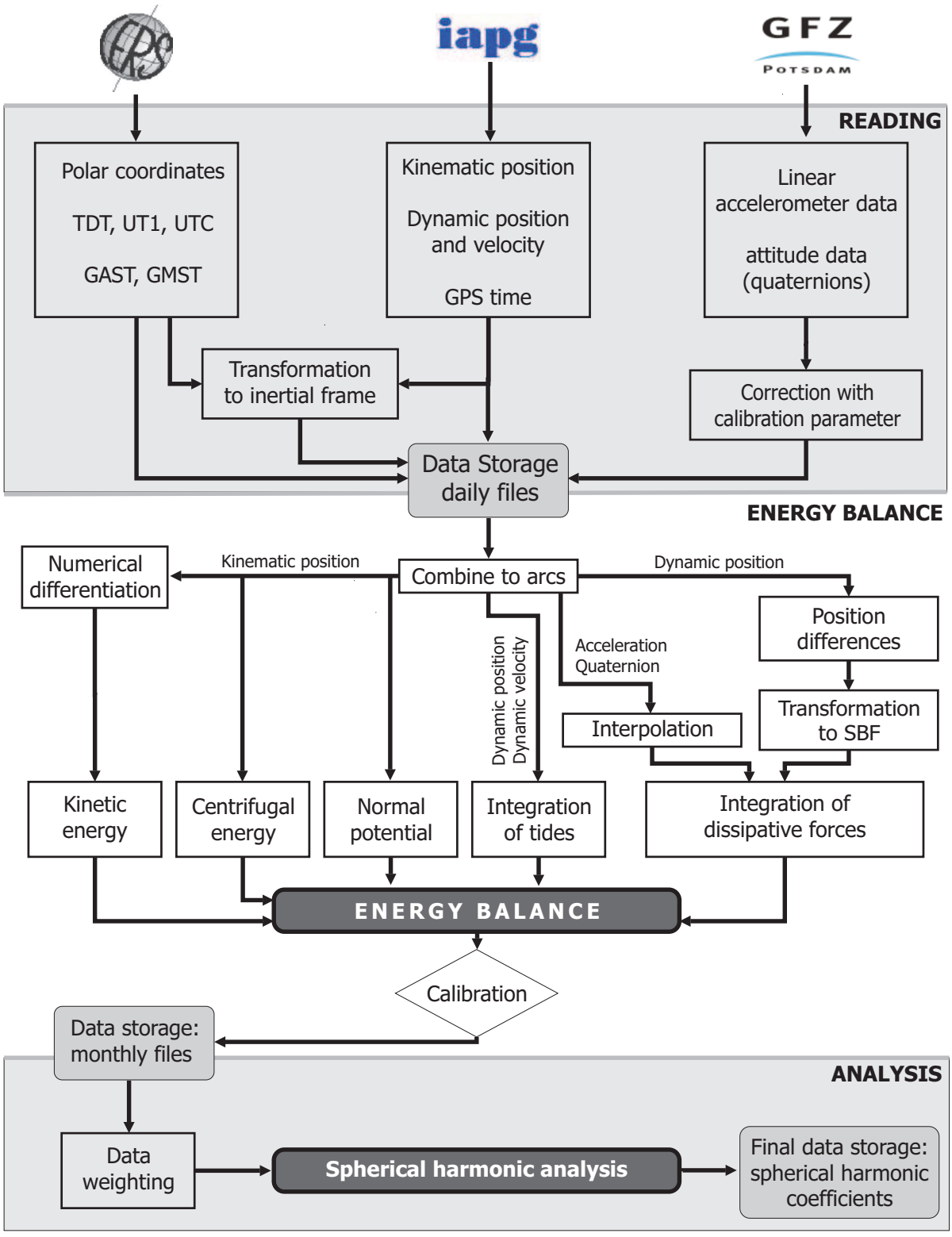

Figure 4.5: Processing structure in case of CHAMP

Different time systems, like e.g., UTC and $GMST$, are derived from the GPS-time and then stored (for transformations, see section 3.1).

The last data source is the GeoForschungsZentrum Potsdam, which provides accelerometer and quaternion data (GFZ Potsdam, 2000). Together with the raw data, parameters for the Lorentz effect, for the deficient radial component, for the bias and the scale of each axis are applied for a preliminary calibration. All the data is saved in Matlab files on a daily basis.

Energy balance. The daily files are then combined to contiguous arcs interpolating small data gaps and separating large data gaps into subsequent arcs. The separation is necessary due to the integral nature of the energy balance approach. Data gaps that cannot be closed by interpolation will cause an error which will propagate to subsequent data points. It is emphasized that proper data handling is essential for the successful implementation of the energy integral (and any method, in general).

Short arcs are dismissed as for the calibration a reasonable long arc is necessary. If short arcs are used, the calibration tends to model long wavelength gravitational signal which must be avoided. A general rule for how to define "small" and "large" cannot be given but, from numerous practical tests, 400 s were accepted as a good compromise for the interpolation and arcs shorter than 12000 s ($\approx$ 2 revolutions) were dismissed. Note that this only applies to data which is integrated, namely dynamic position, velocity, accelerometer data and quaternions.

The kinematic position does not need to be contiguous and data gaps are denoted with 'NaN' in Matlab in order to preserve the structure and the dimensions of the vectors. The kinematic positioning, however, is done in a least-squares adjustment and its accuracy relies heavily on the geometry of the satellite constellation. The residuals of the adjustment do not always identify outliers. Therefore, the data is screened using the following criteria:

$$\Delta_i = \|\boldsymbol{x}_i^{\mathrm{kin}} - \boldsymbol{x}_i^{\mathrm{dyn}}\| \leqslant \epsilon_1 \tag{4.17}$$

$$\Delta_{ij} = |\Delta_i - \Delta_j| \leqslant \epsilon_2. \tag{4.18}$$

The first one is by taking the difference of kinematic and dynamic position. If the length of the difference vector exceeds $\epsilon_1 = 20\,\text{cm}$, the measurement is dismissed. Another effective tool to identify outliers is to take differences between two epochs of the previously mentioned differences. If the value exceeds $\epsilon_2 = 5\,\text{cm}$, the measurement is also dismissed.

In the calculation step, the left two thirds in the center of figure 4.5 are straightforward and the corresponding formulas can be found in the previous sections. The integration of the tidal accelerations differs from the integration of the dissipative forces since it is performed using dynamic velocities in the Earth-fixed frame. The latter uses differences of inertial positions. They are rotated to the space body frame with the help of the quaternions which simplifies the accelerometer calibration. It would also be possible to rotate the accelerations into the inertial or Earth-fixed system but the bias will be mapped into a periodic function due to the time-dependent rotation and its determination will be more difficult.

Short gaps in the accelerometer data are interpolated using cubic spline interpolation and data gaps in the quaternion data are interpolated using spherical linear interpolation (cf. section 3.3). It is not completely consistent to use dynamic positions and velocities instead of kinematic for the integration but the error is small and the data handling is much easier since dynamic positions do not depend as much on the geometry of the system as kinematic positions do. They are supported by the underlying model and the number of data gaps is significantly reduced. Kinematic orbits would yield a number of short arcs and many need to be dismissed due to the calibration procedure.

After the application of the energy integral formula, the data is calibrated and outliers are eliminated. The decision criteria for the outlier test is set to four times the RMS-value of the difference of the calculated disturbing potential to an *a priori* reference (e.g., EGM96). This procedure is repeated for every arc. The arcs are combined for storage. Data gaps, which are denoted so far by 'NaN', are eliminated. For each time point with a complete set of measurements, the disturbing potential is now available at the location of the satellite.

Analysis. The third and final step includes the downward continuation and the spherical harmonic analysis using a least-squares approach. The basic theory of least-squares can be found in numerous publications, e.g., Niemeier (2001), and is only briefly outlined here. The least-squares principle is applied in order to solve an equation system:

$$\begin{aligned} \boldsymbol{l} + \boldsymbol{\epsilon} &= A \cdot \boldsymbol{x} && (4.19) \\ E\{\boldsymbol{\epsilon}\} &= 0 \\ D\{\boldsymbol{l}\} &= Q_{ll}, && (4.20) \end{aligned}$$

where $\boldsymbol{l}$ denotes the observations. The stochastic quantity $\boldsymbol{\epsilon}$ denotes the errors in the measurement. The expectation E of the measurement errors is zero, i.e., the estimation is unbiased and the expectation of the estimated unknowns $\hat{\boldsymbol{x}}$ is equal to the true value of $\boldsymbol{x}$.

$$E\{\hat{\boldsymbol{x}}\} = \boldsymbol{x} \tag{4.21}$$

The coefficient matrix A is a non-stochastic quantity and is formed by the functional model. If the dispersion D is known, i.e., covariance information is available, a stochastic model is included:

$$\Sigma_{ll} = \sigma_0^2 \, Q_{ll} \qquad \text{with} \qquad Q_{ll} = P^{-1} = \frac{1}{\sigma_0^2} \begin{pmatrix} \sigma_1^2 & \sigma_{12}^2 & \cdots & \cdots \\ \sigma_{21}^2 & \sigma_2^2 & \cdots & \cdots \\ \vdots & \vdots & \ddots & \\ \vdots & \vdots & & \sigma_n^2 \end{pmatrix}, \tag{4.22}$$

where σ_0^2 is the variance factor. The cofactor matrix Q_{ll} contains information about the relationships between the observations. The covariance matrix Σ_{ll} consists of the variances and covariances of the observations. For the case of CHAMP, the a priori variance factor was set to one due to the lack of the covariance information or an error model as discussed in section 4.1.2.

If there are more observations than unknowns, the system is overdetermined and the least-squares principle can be applied. The basis of the least-squares principle is the minimization of the weighted square sum of the corrections:

$$\boldsymbol{\epsilon}^T \, P \, \boldsymbol{\epsilon} \Rightarrow \min. \tag{4.23}$$

Equation (4.20) and (4.22) form an approach which is generally known as the *Gauß-Markov* model. If A is regular, the solution vector $\hat{\boldsymbol{x}}$ can be calculated by:

$$\hat{\boldsymbol{x}} = \underbrace{\left(A^T P A\right)^{-1}}_{N^{-1}} \underbrace{A^T P \boldsymbol{l}}_{\boldsymbol{y}} = N^{-1}\boldsymbol{y}. \tag{4.24}$$

The cofactor matrix Q_{ll} is inverted for this application and consequently data with a high variance σ_i^2 or covariance σ_{ij}^2 gets a small weight in the solution. The weighting does not need to be dependent on the covariance information of the data only. The denser data distribution in these areas would lead to a biased solution (Sansò, 1990) but data weighting can also take into consideration the convergence of the orbit towards the polar areas. However, it was not applied here, since it led to a poorer overall performance of the solution than in the unweighted case.

The unknown vector $\hat{\boldsymbol{x}}$ consists of the spherical harmonic coefficients, which can be sorted according to Colombo (1983) as:

$$\hat{\boldsymbol{x}} = \begin{bmatrix} \hat{\boldsymbol{x}}^0 & \hat{\boldsymbol{x}}^1 & \dots & \hat{\boldsymbol{x}}^L \end{bmatrix}^T, \tag{4.25}$$

where each of $\hat{\boldsymbol{x}}^m$ denotes a vector of spherical harmonic coefficients of all degrees l for a specific order m, i.e., $\hat{\boldsymbol{x}}^m = \left[\bar{C}_{m,m}\bar{C}_{m+1,m}\dots\bar{S}_{m,m}\bar{S}_{m+1,m}\dots\right]$. This ordering is beneficial since the corresponding normal matrix is blockdiagonal as can be seen in figure 4.6(b). The off-block-diagonal elements indicate aliasing. Figure 4.6(a) shows a schematic view of the reordering. Note that figure 4.6(a) suggests a separation of even and odd elements, which is neglected here for simplicity.

Each element of the coefficient matrix A is calculated from the spherical harmonic synthesis formula (cf. section 2.1) as

$$a_{ij} = \frac{GM}{R}\left(\frac{R}{r}\right)^{n(j)+1} \begin{Bmatrix} \cos\lambda_i \\ \sin\lambda_i \end{Bmatrix} P_{n(j),m(j)}(\cos\theta_i). \tag{4.26}$$

Each measurement i fills a line in the coefficient matrix. The columns depend on the ordering, i.e., j is a combination of the degree l and the order m. If a cosine or a sine coefficient is calculated, the cosine or sine of the longitude λ_i is to be used, respectively.

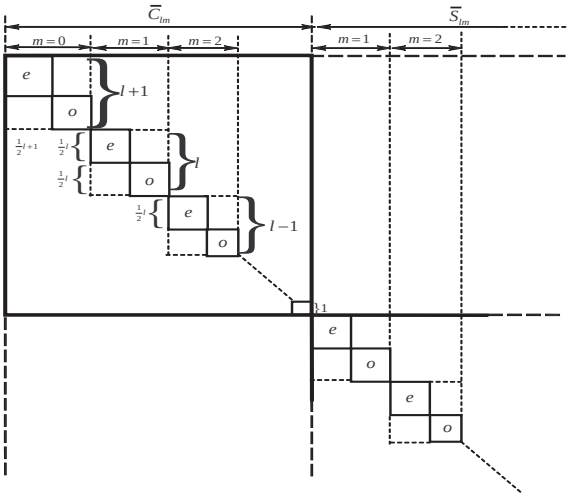

(a) General shape of a block diagonal matrix (Koop, 1993; Xu et al., 2006)

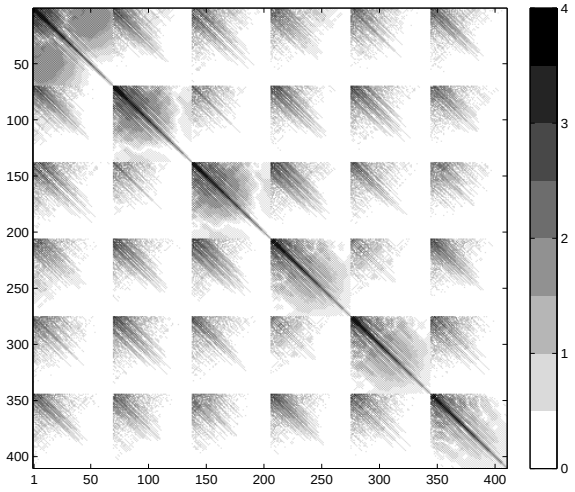

(b) Normal matrix in case of CHAMP (logarithmic scale), maximum degree $L = 70$, order $m = 1 \ldots 6$

Figure 4.6: Block diagonal structure after ordering

A monthly solution has on average 80 000 data points and for a maximum degree of $L = 70$ the number of unknowns is 5041. The A matrix in the least-squares adjustment is subsequently of the dimension $[80\,000 \times 5041]$ which normally cannot be handled by desktop computers. Instead, the normal matrix is build sequentially (e.g., in steps of 1000 measurements). In Matlab code, the procedure is:

```
% build the normal matrix N and the normal vector y
for i = 1:length(data)
    idx = (i-1)*1000+1:i*1000;
    A = f(theta(idx),lambda(idx),r(idx));
    N = N + A'*P*A
    y = y + A'*P*l(idx)
end
```

Subsequently, the system is solved and the unknown vector is reordered to the storage format. On a 2.1 GHz Pentium V with 1 GB of memory a monthly solution is calculated within 15–20 minutes excluding the reading step. Most of the time ($\approx 80\%$) is spent

building the normal matrix N.

This direct method of spherical harmonic analysis has the advantage, that no assumptions are made and it provides the full variance-covariance matrix. The disadvantage is that it is a computationally costly method. Even with a sequentially build normal matrix, the number of elements to be stored is of the order of L^4. For CHAMP, the direct method can be implemented but for GRACE with a maximum degree of $L = 140$ alternative methods must be used. One possibility is the pre-conditioned conjugate gradient method (PCCGM) which is introduced in section 5.3.

Building the normal equations is a trade-off to the memory consumption and must be used with care. If κ is the conditioning number of A, the matrix $N = A^T A$ has a condition number of κ^2. The solution is in best case (Trefethen and Bau III., 1997)

$$\frac{\|\hat{\boldsymbol{x}} - \boldsymbol{x}\|}{\|\boldsymbol{x}\|} = O\left(\kappa^2 \epsilon_{\text{machine}}\right), \tag{4.27}$$

i.e., of the order of the machine precision $\epsilon_{\text{maschine}}$ times the square of the conditioning number. Consequently, the normal equations can yield an unstable system more easily than other methods like the Householder triangularization or the Gram-Schmidt orthogonalization. These provide a solution of the order of $O\left(\kappa \epsilon_{\text{machine}}\right)$ but cannot be applied due to the size of their matrices.

As an alternative, a semi-analytical approach could be used; e.g., Sneeuw (2000); Xu et al. (2006). The method relies on the assumption of an orbit with constant inclination and orbit height. The solution is reached in two steps. In the first step, lumped coefficients are formed from the data using FFT techniques. In order to apply these the satellite must either be in a repeat orbit or the data needs to be interpolated to a regular grid on a torus. The interpolation error is compensated using an iterative scheme. Coefficients with different order m are independent and form a block-diagonal system, which can be solved blockwise in the second step.

4.2.2 Accelerometer calibration

Energy dissipation takes primarily place due to the friction of the satellite in the atmosphere. The accelerometers onboard CHAMP and GRACE enable the measurement of non-gravitational forces but every accelerometer suffers from errors like bias, drift and a scaling factor in each axis. Using them with the energy balance approach, the accelerations are integrated along the orbit and these errors will cause an undesired linear and/or quadratic drift in the energy, thus violating the principle of energy conservation. This effect can be seen in figure 4.7. By ignoring the non-gravitational forces (case:

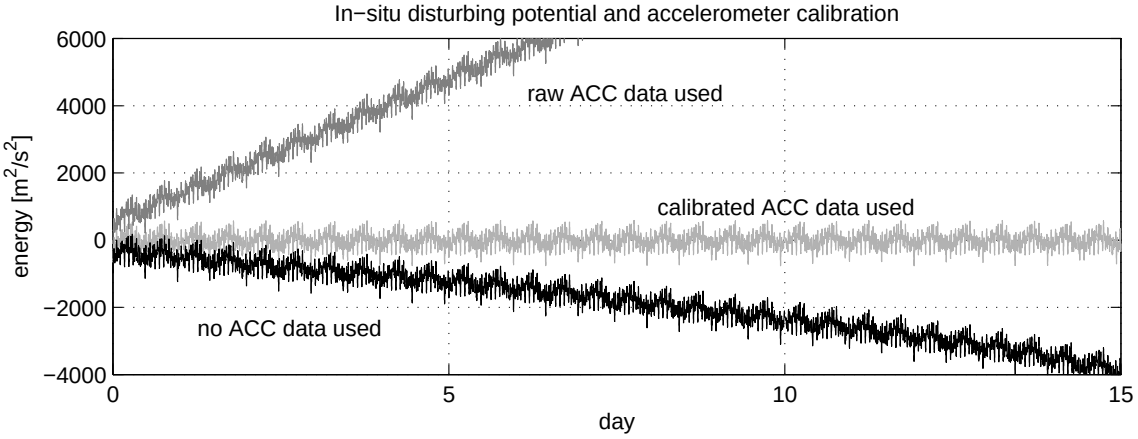

Figure 4.7: Time-series of disturbing potential along the orbit without considering energy dissipation, using uncalibrated and calibrated accelerometer data.

no ACC data used), the disturbing potential T clearly drifts away from a constant level with about $220\,\mathrm{m^2/s^2}$ per day. If raw accelerometer data is used (case: *raw ACC data used*), i.e., the data is used as provided by the GFZ, the drift increases to about $1100\,\mathrm{m^2/s^2}$ per day due to the inherent bias in the measurements. After the calibration (case: *calibrated ACC data used*), the disturbing potential is fluctuating around zero thus representing the principle of energy conservation.

Error modelling. The error model for an accelerometer includes primarily a scaling matrix S, a bias $\boldsymbol{b}$, and a linear drift term $\boldsymbol{d}$, which need to be determined in a least-

squares adjustment. The relation between the true non-gravitational forces and the measurement of an accelerometer can be described as:

$$\boldsymbol{f} = S\boldsymbol{f}^{\text{true}} + \boldsymbol{b} + \boldsymbol{d}t \ , \text{ with } \quad S = \begin{bmatrix} s_1 & 0 & 0 \\ 0 & s_2 & 0 \\ 0 & 0 & s_3 \end{bmatrix} . \tag{4.28}$$

The model might be extended using a quadratic and/or a cubic drift term. Introducing equation (4.28) into the energy balance approach, the measurements are integrated along the orbit:

$$E^{\text{diss}} = \int_{\boldsymbol{x}(t_0)}^{\boldsymbol{x}(t)} S\boldsymbol{f}^{\text{true}} d\boldsymbol{x} + \int_{\boldsymbol{x}(t_0)}^{\boldsymbol{x}(t)} \boldsymbol{b} d\boldsymbol{x} + \int_{\boldsymbol{x}(t_0)}^{\boldsymbol{x}(t)} \boldsymbol{d}\,(t - t_0)\, d\boldsymbol{x} \tag{4.29}$$

Note that the position vector $\boldsymbol{x}$ is rotated to the SBF. For simplicity, the scale, bias and drift coefficients are considered as scalar. Consequently, the parameters will loose their physical meaning and just serve as an empirical error model. The model becomes:

$$E^{\text{diss}} = s \int_{\boldsymbol{x}(t_0)}^{\boldsymbol{x}(t)} \begin{pmatrix} 1 \\ 1 \\ 1 \end{pmatrix} \boldsymbol{f}^{\text{true}} d\boldsymbol{x} + b \int_{\boldsymbol{x}(t_0)}^{\boldsymbol{x}(t)} \begin{pmatrix} 1 \\ 1 \\ 1 \end{pmatrix} d\boldsymbol{x} + d \int_{\boldsymbol{x}(t_0)}^{\boldsymbol{x}(t)} \begin{pmatrix} 1 \\ 1 \\ 1 \end{pmatrix} (t - t_0)\, d\boldsymbol{x} \tag{4.30}$$

Interestingly, the integration $\int_{\boldsymbol{x}(t_0)}^{\boldsymbol{x}(t)} (1,1,1)^T d\boldsymbol{x}$ will yield a linear and the integration $\int_{\boldsymbol{x}(t_0)}^{\boldsymbol{x}(t)} (1,1,1)^T\,(t - t_0)\, d\boldsymbol{x}$ a quadratic drift as shown in figure 4.8. This can be more easily understood if the integration along the orbit, i.e, $\int d\boldsymbol{x}$, is considered as an integration in time, i.e., $\int \boldsymbol{v} dt$. The velocity $\boldsymbol{v}$ of the satellite in the SBF is, in good approximation, a constant value in the alongtrack direction. Its integration yields the drift. Consequently, the bias will result in a linear drift, and the linear drift term in a quadratic drift.

Another way of simplification is suggested by Han (2003). Considering just the alongtrack component of the accelerometer, the determination of the bias and scaling factor retain its physical meaning. It is a good approximation since the atmosphere is the strongest non-gravitational force affecting the satellite and will act primarily in the alongtrack component. Other effects like, e.g., the solar radiation pressure will however

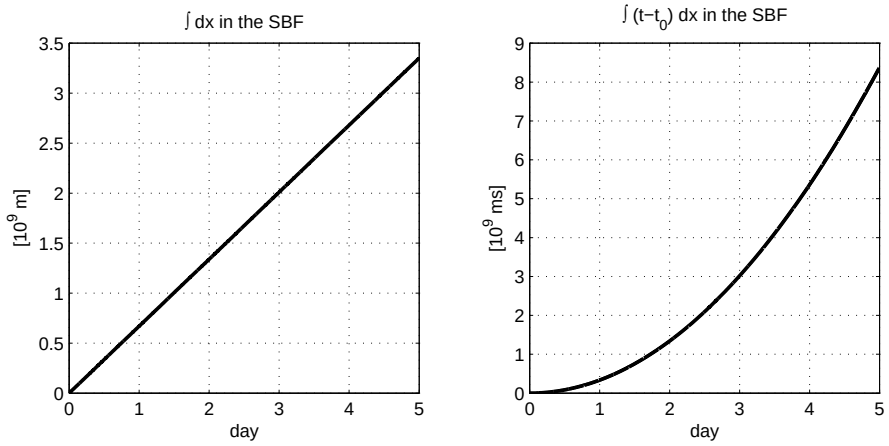

Figure 4.8: Integration of $d\boldsymbol{x}$ and $(t - t_0)\, d\boldsymbol{x}$ in the SBF

continuously change their working point on the satellite due to its motion. An error, though small, is introduced and the energy balance is theoretically not valid anymore.

At the same time, considering the scale, bias and drift coefficient equal in all three directions is a compromise to the solvability of the parameters in a least-squares adjustment. Theoretically, for each direction one parameter must be estimated. The corresponding error equation is:

$$\begin{aligned} E^{\text{diss}} = {} & s_x \int_{x(t_0)}^{x(t)} f_x^{\text{true}} dx + s_y \int_{y(t_0)}^{y(t)} f_y^{\text{true}} dy + s_z \int_{z(t_0)}^{z(t)} f_z^{\text{true}} dz \\ & + b_x \int_{x(t_0)}^{x(t)} dx + b_y \int_{y(t_0)}^{y(t)} dy + b_z \int_{z(t_0)}^{z(t)} dz \\ & + d_x \int_{x(t_0)}^{x(t)} (t - t_0)\, dx + d_y \int_{y(t_0)}^{y(t)} (t - t_0)\, dy + d_z \int_{z(t_0)}^{z(t)} (t - t_0)\, dz \end{aligned} \tag{4.31}$$

The input for the least-squares adjustment are differences ΔT of the disturbing potential either to a reference field or from a crossover determination. The disturbing potential is a one-dimensional quantity given along the orbit. The three-dimensional accelerometer data is mapped by the integration to the one-dimensional quantity, and the directional information is lost, which makes the inversion impossible (Raizner et al., 2006).

On the other hand, the primary aim of the calibration is not the derivation of physical meaningful parameter for the accelerometer but the calibration of the disturbing

potential. For gravity field determination, the most important target is the removal of the drift and thus the fulfillment of energy balance.

At the time of the accelerometer calibration, the constant c from the energy integral (4.8) might or might not be included. The full model for the calibration is given as:

$$\Delta T\left(t\right) = c + s\int_{\boldsymbol{x}(t_0)}^{\boldsymbol{x}(t)} \begin{pmatrix}1\\1\\1\end{pmatrix} \boldsymbol{f}^{\text{true}} d\boldsymbol{x} + b\int_{\boldsymbol{x}(t_0)}^{\boldsymbol{x}(t)} \begin{pmatrix}1\\1\\1\end{pmatrix} d\boldsymbol{x} + d\int_{\boldsymbol{x}(t_0)}^{\boldsymbol{x}(t)} \begin{pmatrix}1\\1\\1\end{pmatrix} \left(t - t_0\right) d\boldsymbol{x} \quad (4.32)$$

Calibration techniques. In standard INS applications, the bias can be determined by aligning the accelerometer with the local gravity vector in two different directions. The sum of the two measurements yields the bias. However, since the accelerometer in the satellite is inaccessible and is not measuring any gravity, other calibration methods need to be applied.

The first possibility includes the **application of high- or band-pass filters** (Gerlach et al., 2003b). The basis for the filtering approach is the fact that the accelerometer is designed for a specific bandwidth, and applying a high- or band-pass filter will remove in the ideal case any signal in the frequency part outside the bandwidth of the accelerometer. However, this approach is disregarded here since it is difficult to design the proper filter without filtering gravity signal.

The second possibility is to use a **crossover adjustment**. A crossover occurs, when the satellite track is crossing its own path from an earlier revolution. Neglecting time-variable changes between the crossings the difference between these two measurements should be zero. Any deviation is the result of errors in the measurements and can be modelled. The advantage of the crossover calibration is that no *a priori* information is necessary. The disadvantage is that the measurements are not taken in the exact crossover location and the arcs normally do not cross in a 3D sense, cf. figure 4.9. This means that interpolation along the orbit and radial up- or downward continuation is necessary. The second disadvantage is that every ascending arc must be crossed with all descending arcs and vice-versa, which becomes quickly computational costly.

Several procedures to find crossover locations are suggested for different cases and the calculations can be of theoretical nature (Kim, 1997), rely on certain properties, or be numerical (Schrama, 1989).

Another problem is the assignment of the point in time when the crossover really occurs. The crossover location could be attributed to the time of the pass of the satellite in the crossover point either of the ascending or the descending arc. On the other hand, the accelerometer bias causes a drift, which means that the longer the time between the two passes of the satellite at the crossover location, the bigger the difference in the energy. Figure 4.10 illustrates this by showing the differences in energy versus the time difference. A more rigorous approach is to divide the energy difference by the time difference and interpret the result as a 1storder Taylor differentiator, thus determining a time series of the first derivative, see also Weigelt and Sneeuw (2004).

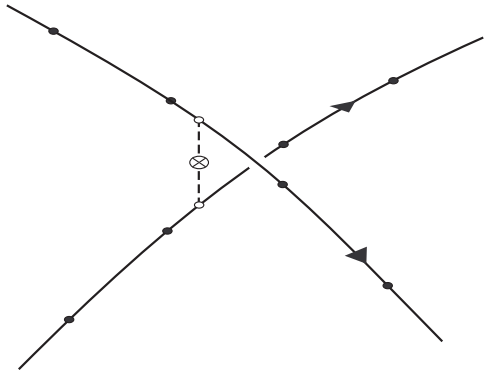

Figure 4.9: Crossover of ascending and descending arcs

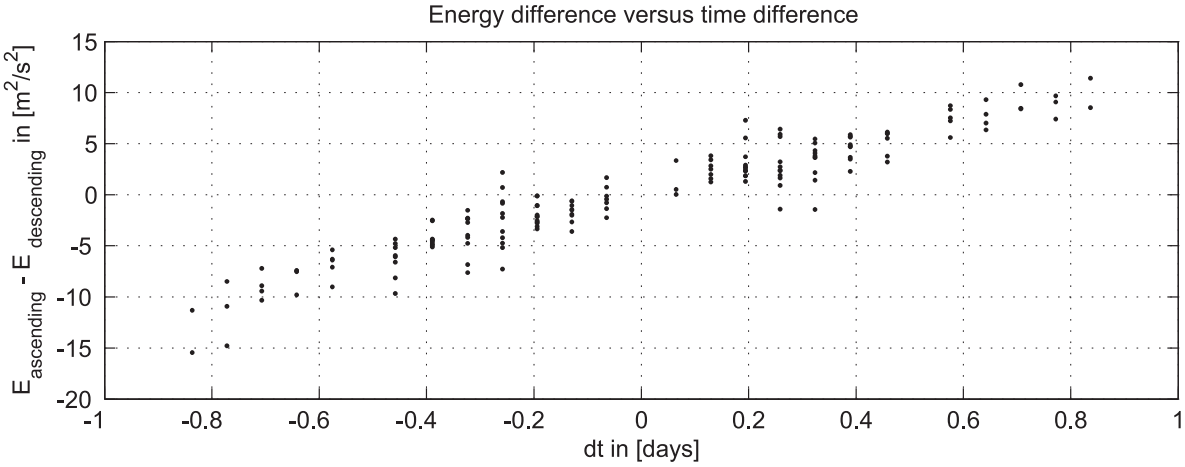

Figure 4.10: Crossover calibration: energy difference vs. time difference

The last and maybe simplest approach is the **calibration with *a priori* data**. The difference ΔT on the left hand side of equation (4.32) is calculated by differencing the disturbing potential derived from the satellite measurement and a corresponding time-series from an existing *a priori* gravity field model. According to Han et al. (2002), every current *a priori* gravity field can be used for this purpose since differences between them are negligible and won't affect the calibration results. Collecting several differences over time, the unknown calibration parameter c, s, b and d can be estimated in a least-squares adjustment. Since the calibration parameters are not constant over time, the data is divided in daily arcs and one set of parameters is determined per day. Figure 4.11 shows that the calibration method removes any drift reliably. The

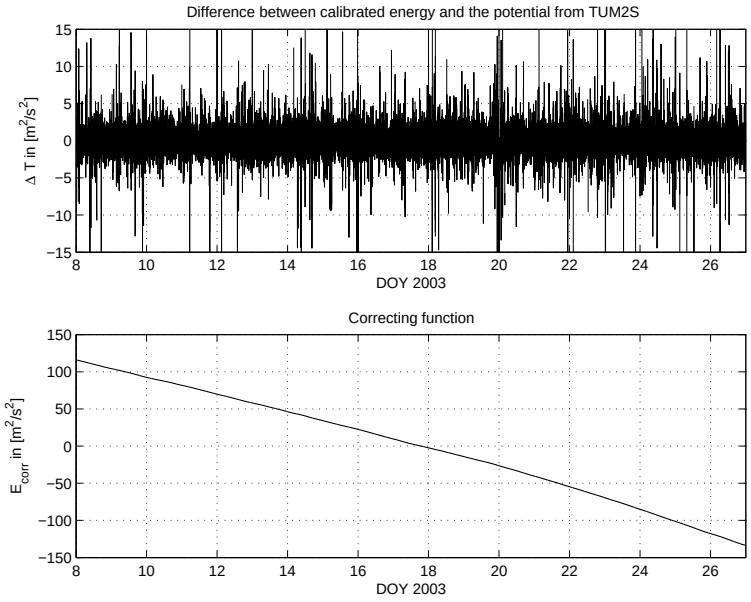

Figure 4.11: Modelling with *a priori* data: difference between calibrated energy and the disturbing potential from TUM2S (top); the correcting function (bottom)

advantage of this approach is that every data point can be used for the calibration. Arbitrarily short arcs could be calibrated. Nevertheless, the arcs should be reasonably long in order to avoid the removal of gravity information. This is avoided by selecting arcs with a minimum length of 12 000 s as discussed in section 4.2.1. The technique is applied throughout the rest of the thesis.

4.2.3 Quality analysis

Two years of CHAMP data for the period from April 2002 to February 2004 is processed, in total. By comparing the results to GGM02s, which is derived from GRACE data, the results can be validated with independent and more accurate data. This enables the investigation of effects like, e.g., the groundtrack pattern and other aliasing phenomena on a single satellite mission. Throughout the computations of the monthly as well as the two year solution, all background models and transformations are handled consistently.

Global gravity field using two years of CHAMP data. Gerlach et al. (2003b) showed that the usage of kinematic data yields qualitatively the same gravity field solutions but has the advantage of the independence from any *a priori* data. Dynamic orbits depend on the choice of the *a priori* data and the gravity field solution is biased towards it. Kinematic data is derived without the use of any *a priori* data at the cost of higher noise in the position data and the necessity to derive velocities numerically. Wermuth et al. (2004) presented the two year solution TUM2s for the same period as discussed here. Although more data is now available, the emphasis is here on the usage of kinematic data which are currently provided only for the presented period.

The solution using the two years of data is denoted as UofC and is compared first to EGM96, which is a pre-CHAMP multi-satellite and multi-terrestrial gravity field. It was the standard gravity field before the satellite missions. Figure 4.12 shows the difference till degree and order 60 in the spatial domain and as mean values along the meridians and parallels, respectively. On average, the difference along parallels is 41.5 cm and along meridians 37.3 cm. In particular, the difference in Antarctica is clearly visible and is in the range of ± 2 m. Interestingly, the ocean area between 40° and 140° co-latitude has a fairly good agreement with EGM96, which is most likely related to the usage of altimetry data in EGM96. Noticeable are also the deficiencies in EGM96 in remote continental areas, like, e.g., the Amazon basin, the Himalayan, the Alps and other areas. The improvement in these areas is up to 1 m.

Comparing with TUM2s, UofC is expected to be on the same level. Figure 4.13 shows

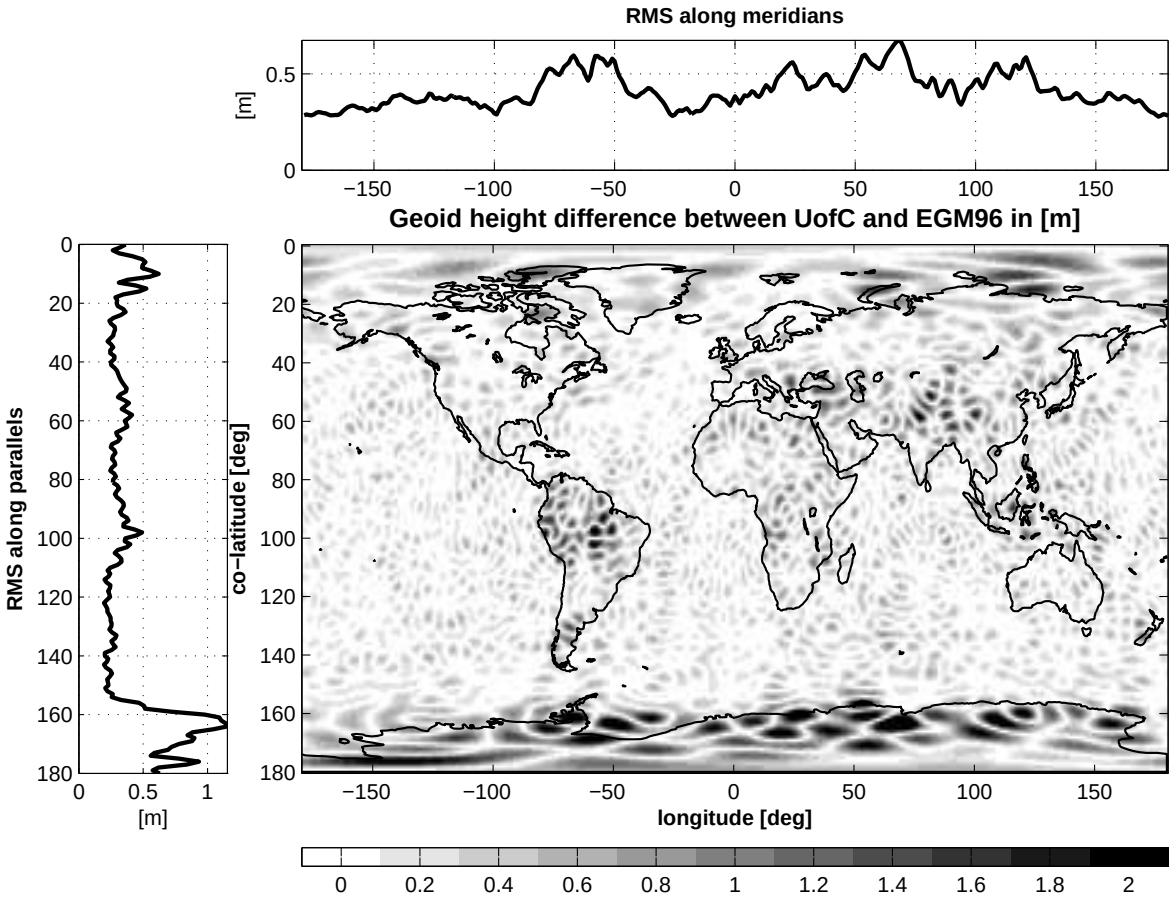

Figure 4.12: Geoid height difference between UofC and EGM96 in [m]: spatial (center), RMS along the meridians (top) and along parallels (left). $L^{\max} = 60$.

the difference. Note that the scale is changed to $\pm 0.2\,\mathrm{m}$ and the degree is restricted to 40. The spatial plot shows differences in the polar areas and north-south stripes, which are likely related to the orbit of the satellite. One critical point in the derivation of TUM2s was the filtering procedure in order to calibrate the data. The disturbing potential of an *a priori* field (EGM96) was removed, the residuals filtered with a Butterworth high-pass filter, and the *a priori* information restored. The filter, however, removed not only the drift but also gravity signal which led to less signal power in the low degree harmonics. The comparison of TUM2s and GGM02s in figure 4.14 shows the same north-south stripes as figure 4.13. In the calibration of TUM2s, gravity signal was filtered along the orbit, causing the pattern. The mean difference of TUM2s along paral-

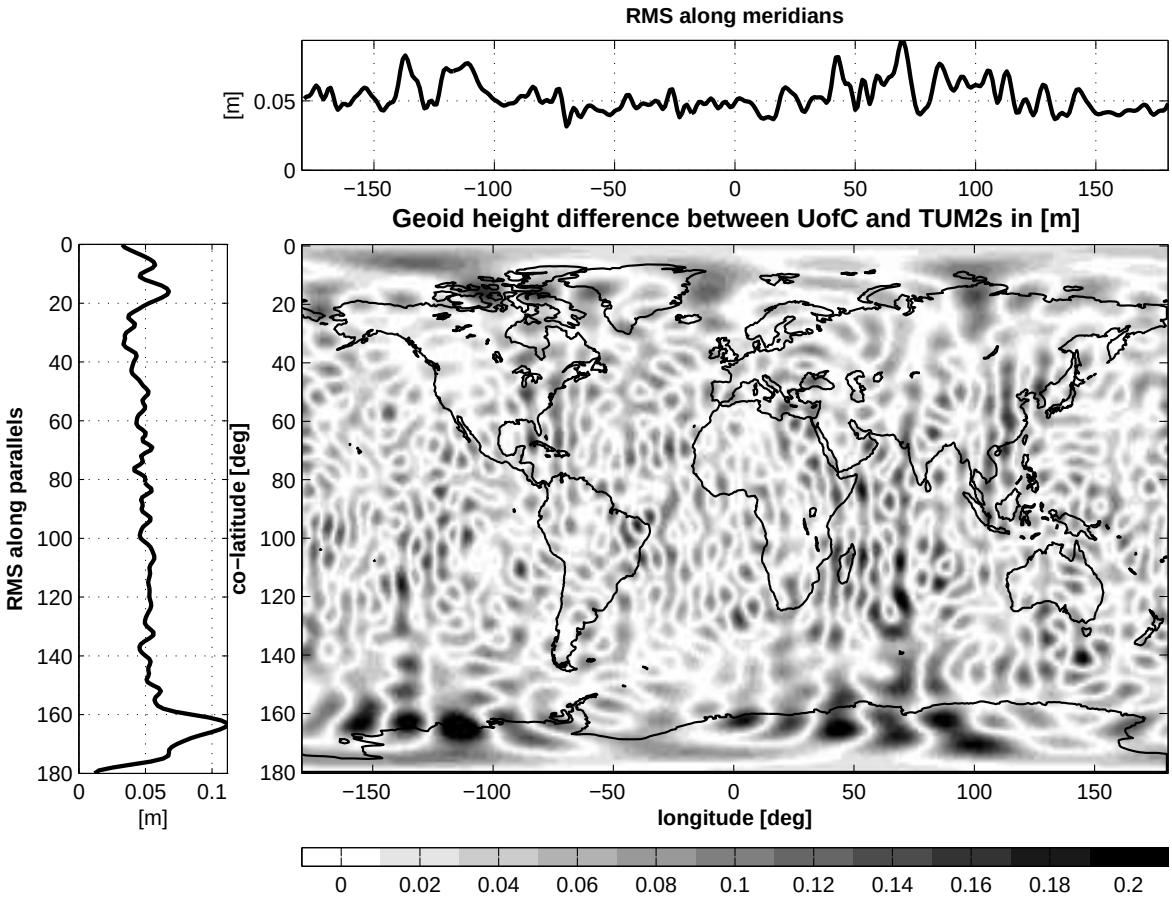

Figure 4.13: Geoid height difference between UofC and TUM2s in m: spatial (center), RMS along the meridians (top) and along parallels (left). $L^{\max} = 40$.

lels is in both comparisons, i.e., to UofC and GGM02s, in the range of a few centimeters and on average 5.2 cm. There is also an increase towards the polar areas visible.

Finally, the comparison of UofC and GGM02s shows the quality of the newly derived solution. The difference between UofC and TUM2s is primarily the refined calibration procedure as discussed in section 4.2.2, which yields a better solution up to degree and order 40 (cf. also figure 4.16). The spatial pattern of UofC is fairly random in contrast to the one of TUM2s, which suggests that no systematic effect is involved anymore and the solution up to degree 40 is of higher quality. The average difference in the RMS along parallels is 4.22 cm and thus approximately 19.1% better than the one of TUM2s. The average RMS along meridians is 4.28 cm and the improvement is approximately

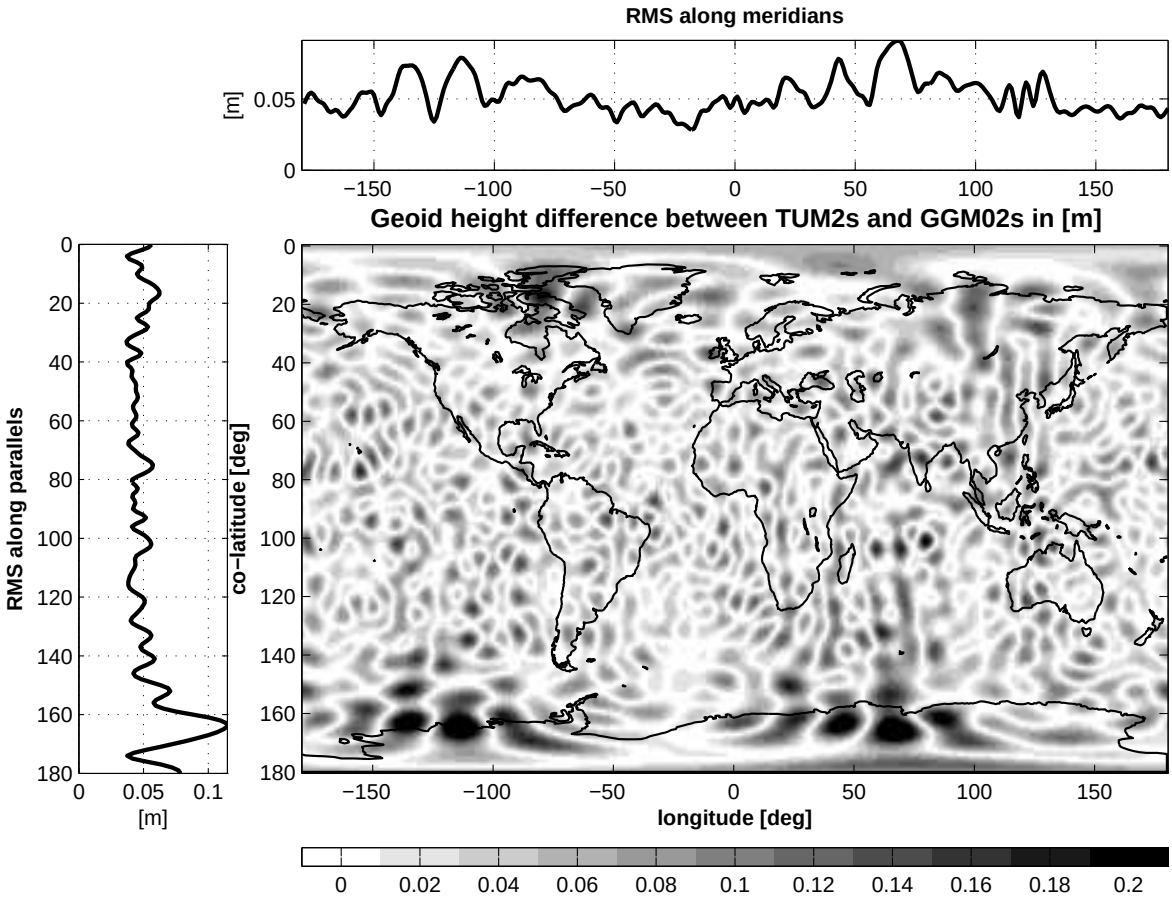

Figure 4.14: Geoid height difference between TUM2s and GGM02s in m: spatial (center), RMS along the meridians (top) and along parallels (left). $L^{\max} = 40$.

18%. Besides, UofC shows a slight increase from the pole towards the equator in the RMS along the parallels. This might be related to the data distribution which favors the high-latitude areas.

The quality can also be quantified in the difference spectrum (figure 4.16). The comparison in the spectral domain is done using the differences between the signal of UofC, TUM2s and EGM96 w.r.t. GGM02s as an error estimate. The standard deviations derived from the coefficients matrix of the unknowns $Q_{\hat{x}\hat{x}}$ is available, too, but was found in general to be overoptimistic for the low degrees. For verification, it is shown in figure 4.16 as a dashed line. The difference w.r.t. GGM02s is a comparison with an external, independent and more accurate data source and therefore gives a better insight into

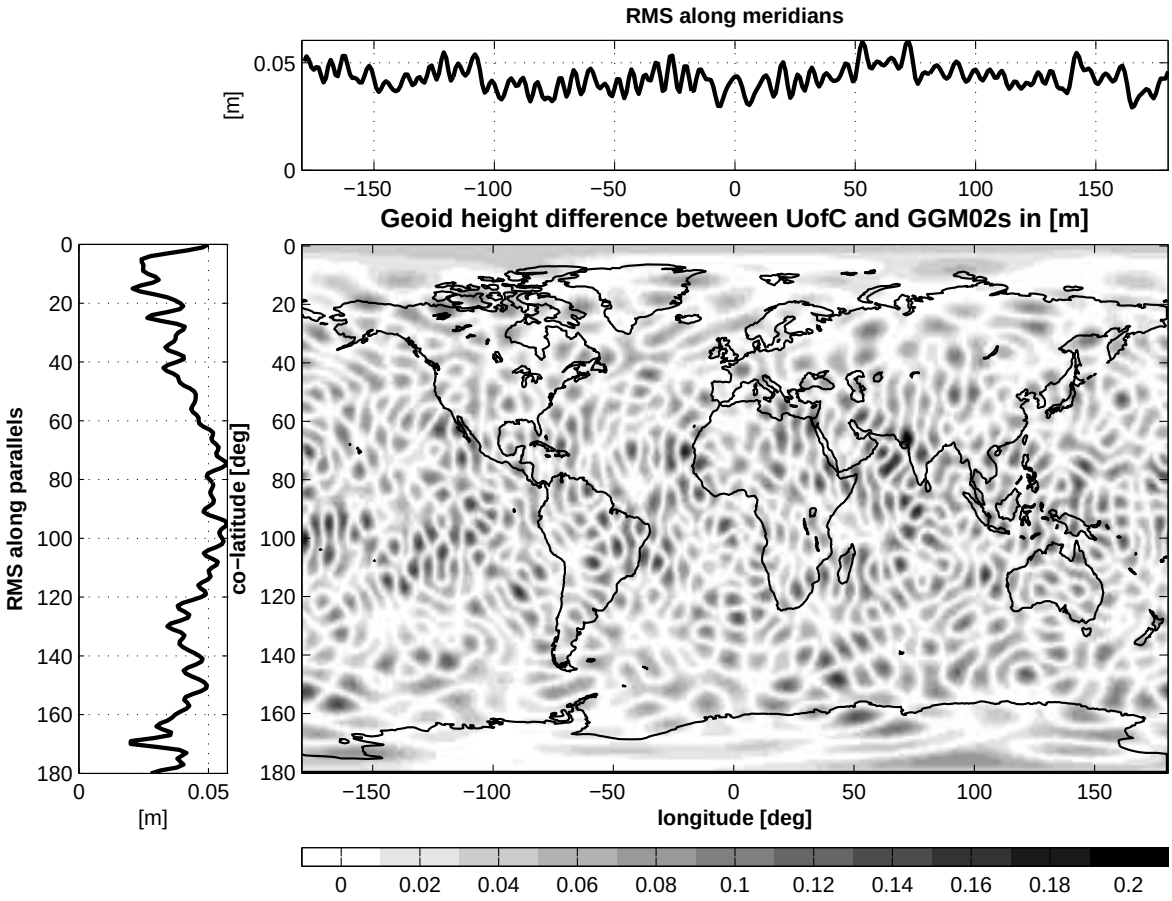

Figure 4.15: Geoid height difference between UofC and GGM02s in m: spatial (center), RMS along the meridians (top) and along parallels (left). $L^{\max} = 40$.

the quality of the solution. Nevertheless, conclusions for the very low degrees are not as reliable since GRACE is known to be deficient in the low degrees.

The top left panel of figure 4.16 shows the difference degree RMS, which gives a very good idea of the quality of each gravity model. Both TUM2s and UofC outperform EGM96 up to degree and order 60, with the exception of degree 4. The SH-coefficient $\bar{C}_{40}$ was found to be deficient and causing a loss of accuracy by approximately one order of magnitude. Substituting this value with the one provided by EGM96 fixes the peak and yields a considerable improvement in the cumulative geoid error. The cause for this peak is not clear yet. Interestingly, also the models TUM2s, EIGEN-2, EIGEN-3p (Reigber et al., 2005a) and GIS-CHAMP (Reubelt et al., 2006) show the same peak. In general,

UofC shows an improved performance for the low degrees compared to TUM2s due to the calibration.

The interpretation of the cumulative geoid error obviously depends on the handling of $\bar{C}_{40}$. If the value is unchanged, the level of 1 cm is exceeded with degree 4, i.e., the 1 cm geoid height accuracy is only reached with a spatial resolution of more than 5000 km. However, fixing the value of $\bar{C}_{40}$ yields a considerable improvement. The 1 cm-level is exceeded at degree 14, i.e., UofC reaches a 1 cm geoid height accuracy with a spatial resolution of 1400 km half wavelength. In the following, the effect of the calibration is visible. TUM2s exceeds the 2 cm-level at degree 10 and UofC at degree 25. From degree

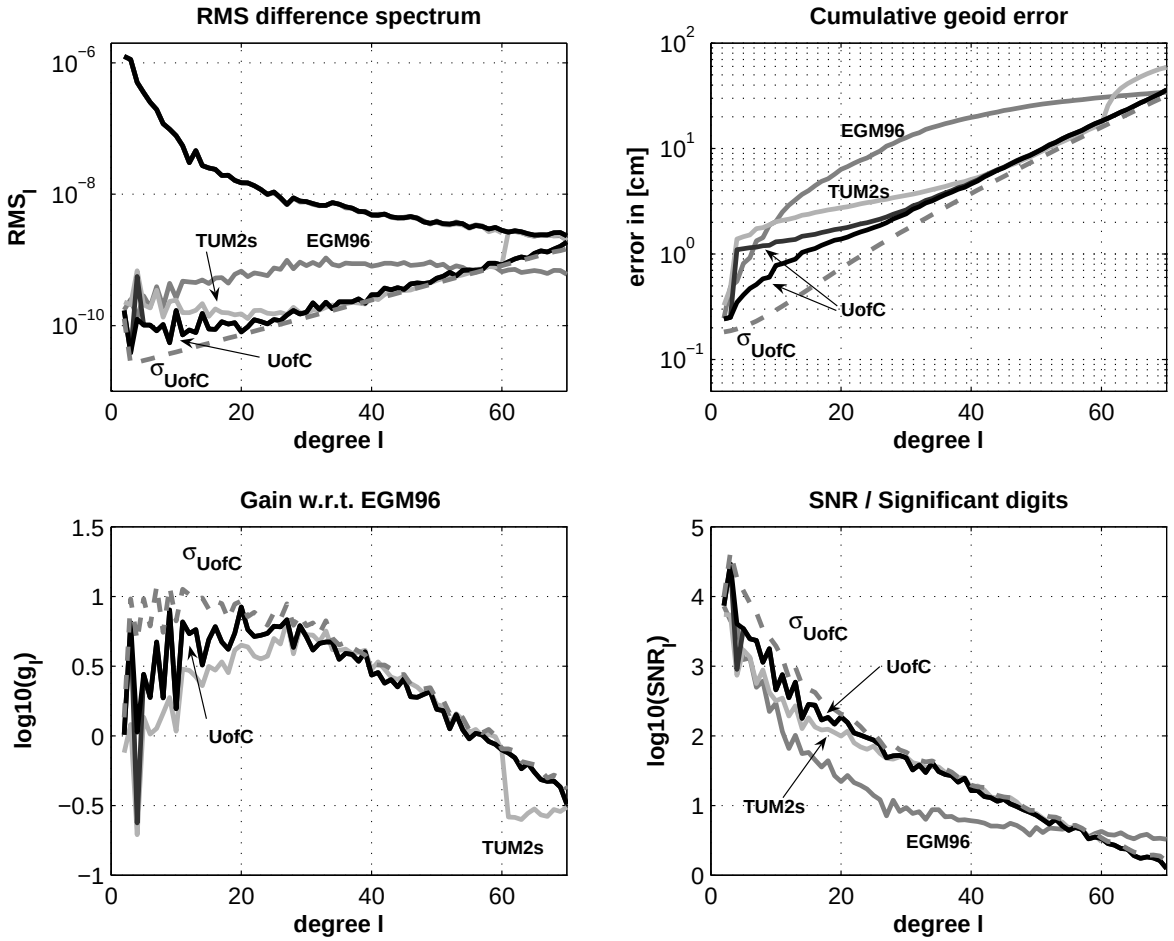

Figure 4.16: Difference spectrum w.r.t. GGM02s: degree RMS (top left), cumulative geoid error (top right), gain w.r.t. EGM96 (bottom left), significant digits (bottom right)

40 on, the error of both is identical.

The bottom left panel shows the gain with respect to EGM96, i.e., it is the ratio of the difference of UofC to GGM02s and the difference of EGM96 to GGM02s (cf. section 2.2.4). A positive value shows an improvement, a negative value a degradation. The maximum improvement is for degree 20 where the gain is almost one order of magnitude. Degree 4 has the aforementioned degradation if it is unchanged. Beyond degree 60, the errors in the kinematic velocity set the limit of the recovery of the gravity field from CHAMP. The same conclusion can be drawn from the signal-to-noise ratio (cf. figure 4.16, bottom right).

Overall, the analyses in the spatial and the spectral domain show that CHAMP improved the accuracy of the spherical harmonics up to one order of magnitude in the low degrees up to 60 and has its most significant impact around degree 20. Due to the velocity determination, CHAMP-only solutions are limited to degree 60. Note that dynamic orbits will yield a similar picture, but with improved performance for degrees higher than 40 due to the lower noise in the velocity. However, due to the reasons explained before, only kinematic results are discussed here.

Monthly gravity field recovery. It is currently accepted that the derivation of monthly gravity field information from CHAMP-only solutions is not successful. Reigber et al. (2005a) concluded that monthly gravity solutions solely from CHAMP observations reveal an unrealistic large scattering. Sneeuw et al. (2005) tried to recover time-variable gravity signal with the energy balance approach and kinematic orbits. For their investigations, TUM1s, which contains one year of CHAMP data, was used. Their investigation was restricted to degree 4, i.e., a half wavelength of approximately 5000 km. They showed that the error level of the monthly CHAMP solutions is insufficient for revealing time-variations. Orbit decay and consequently the groundtrack variation is one of the main contributors to this effect. Due to the improved calibration and the increased signal power, the computations are repeated here.

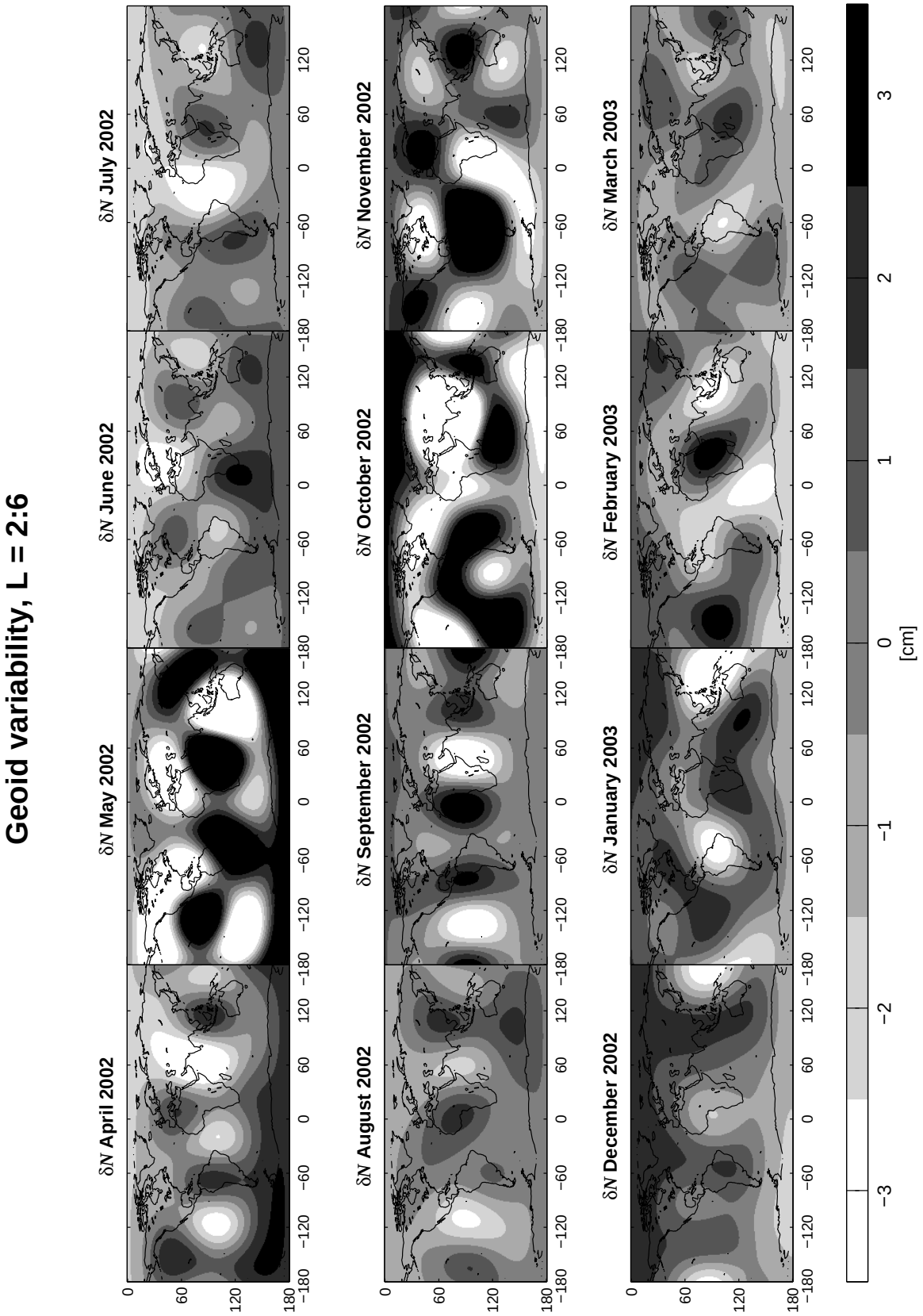

Figure 4.17: Variability in geoid height for low degree harmonics: April 2002 - March 2003

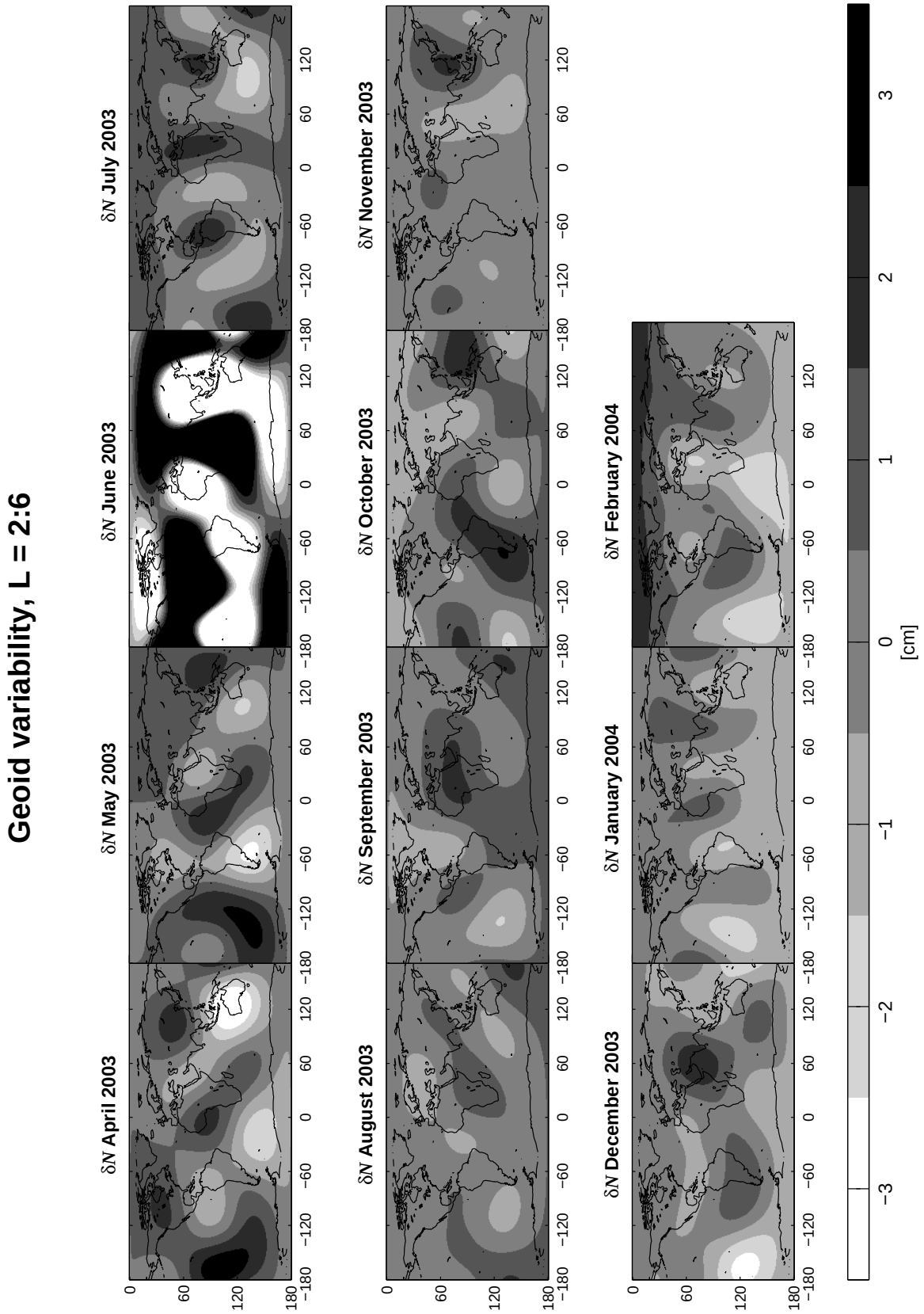

Figure 4.18: Variability in geoid height for low degree harmonics: April 2003 - February 2004

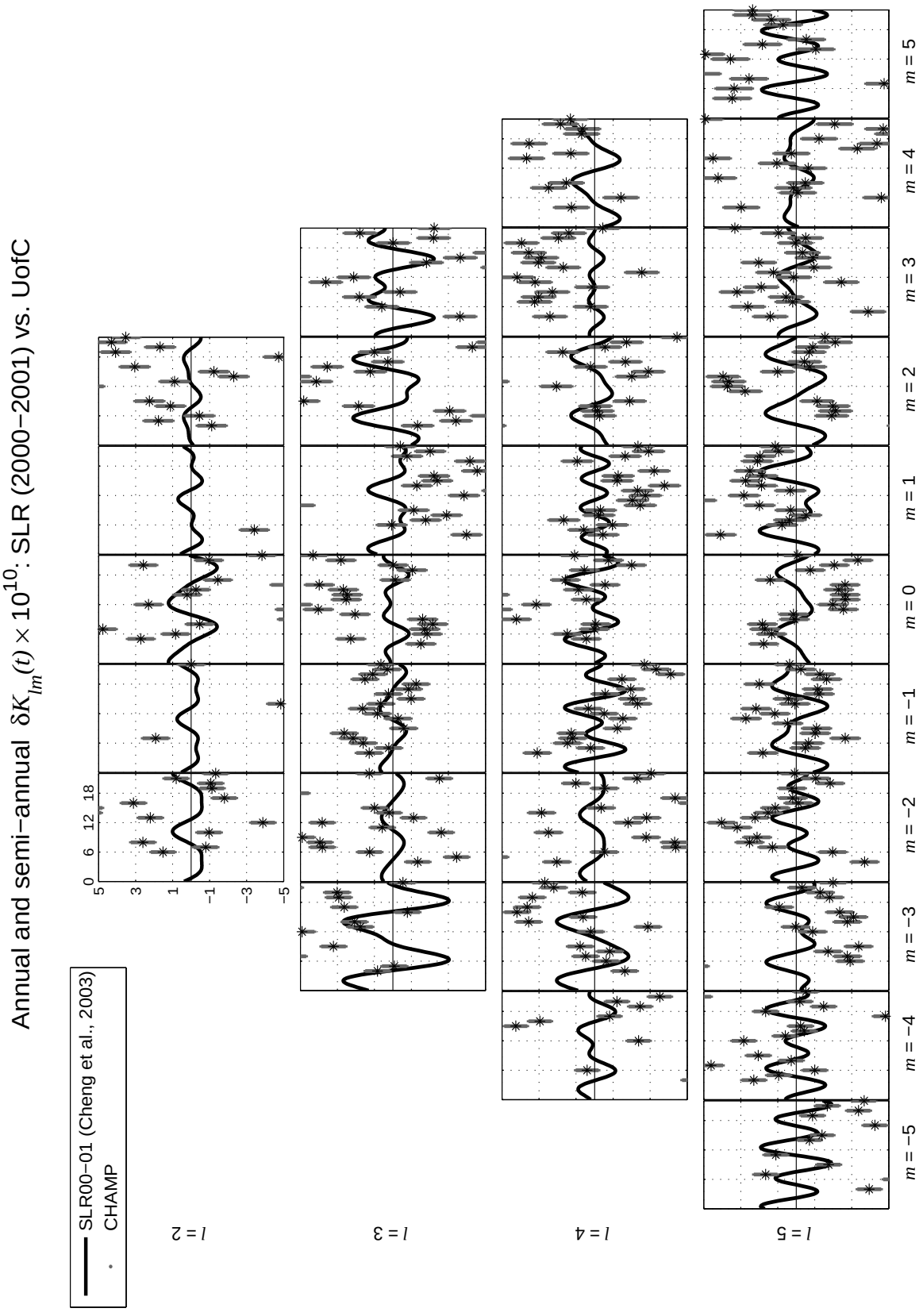

Figure 4.19: Comparison of low degree harmonics with SLR from Cheng et al. (2004)

Figures 4.17 and 4.18 show the monthly variations in the spatial domain after the subtraction of UofC for the very low degrees from 2 to 6. Expected patterns are seasonal variations between northern and southern hemisphere due to, e.g., precipitation and runoff. April 2002 and December 2002 show such a behavior. However, one year later the same months do not show any similar pattern. Other areas like the Amazon basin also show no annual or semi-annual signal but a random change instead. Immediately obvious are also the artifacts in May 2002, October 2002, November 2002 and especially in June 2003.

In the spectral domain, the monthly solutions are compared to Satellite Laser Ranging (SLR) data (Cheng et al., 2004) in figure 4.19. Only the annual and semi-annual signal is compared, i.e., the trend in the monthly CHAMP solutions was removed beforehand. Note that the y-axis of each plot is restricted to $\pm 5 \cdot 10^{10}$ and due to their high variations some of the monthly values of the CHAMP solution do not appear. Each value of a CHAMP coefficient is denoted by a "$\star$". The errorbars denote an average error of the solutions. It seems that the values are spread randomly around the signal of the SLR model.

l = 2				4.93	14.82	5.03	16.58	4.94			
l = 3			8.96	4.45	2.61	6.58	8.98	6.29	5.39		
l = 4		12.66	8.78	3.52	10.81	7.35	7.37	4.39	6.18	6.74	
l = 5	13.31	4.49	4.29	4.63	1.58	6.64	7.28	6.36	3.32	4.33	8.66
	m=-5	m=-4	m=-3	m=-2	m=-1	m=0	m=1	m=2	m=3	m=4	m=5

Table 4.1: Difference RMS between $\delta K_{lm}^{\mathrm{SLR}}(t) \times 10^{10}$ and $\delta K_{lm}^{\mathrm{CHAMP}}(t) \times 10^{10}$

Table 4.1 shows the difference RMS between the low degree harmonics derived from CHAMP and the SLR model. It confirms the bad agreement with the SLR model. For many of the coefficients the difference is exceeding the predicted signal. In particular, the coefficients S_{55}, S_{44}, S_{41}, S_{21} and C_{21} show a very poor performance. Note that the latter two were estimated and not set to the values suggested by the IERS.

Although the improved low wavelength behavior of UofC seemed promising, the results still point to the conclusion that even with the improved calibration technique the derivation of time variable gravity field information is not possible.

4.2.4 Influence of the groundtrack on the monthly static solution

Assuming that no time variable gravity field can be derived, the variability of the monthly solutions needs another explanation. The changes in May 2002, October 2002, November 2002 and June 2003 of figure 4.17 and 4.18 cannot be explained by random errors but suggest a systematic effect. Figure 4.20 shows the RMS of geoid height

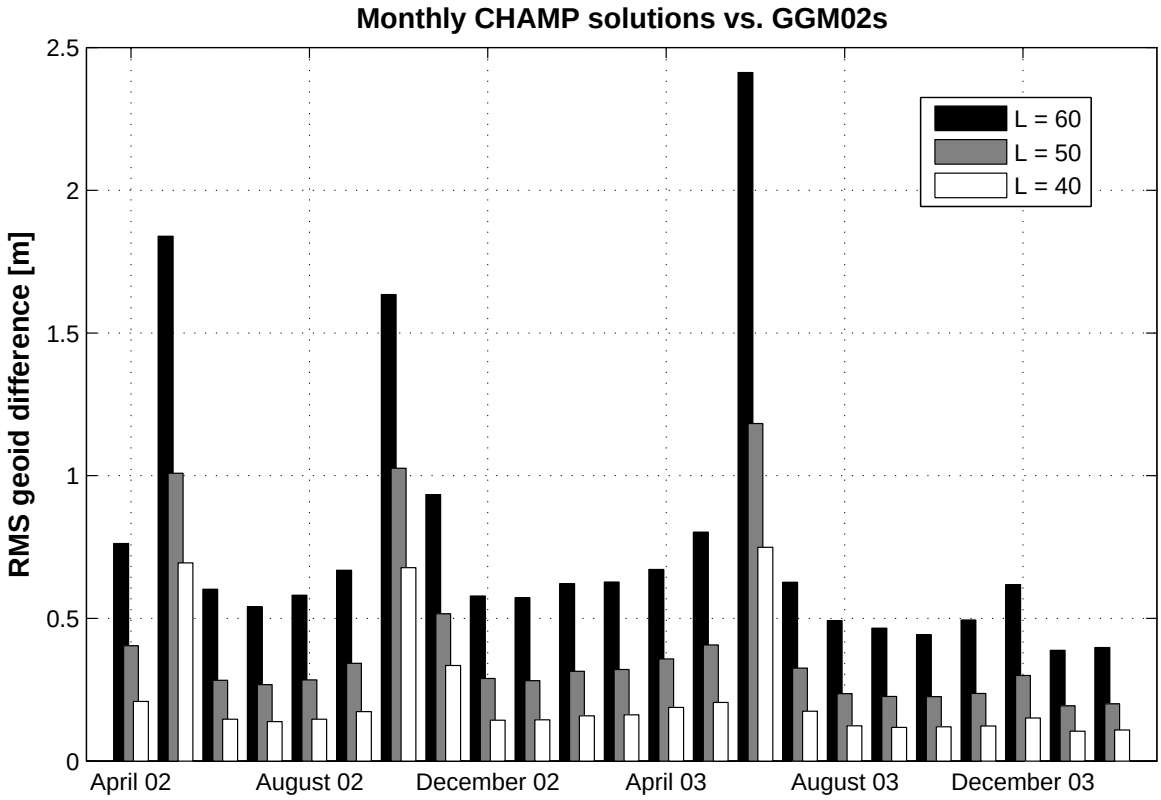

Figure 4.20: RMS of the difference between CHAMP monthly solutions and GGM02s in terms of geoid height

differences w.r.t. GGM02s for the monthly solutions in the spatial domain. The bars are grouped by month for three different degrees of development. The months May 2002,

October 2002 and June 2003 have RMS values of over 1 m for degree $L = 60$ whereas all other months are, on the average, around 0.75 m. A decay from the beginning to the end of the period is also visible and can be connected to the decaying orbit of the satellite. CHAMP is slowed down primarily due to atmospheric drag and looses height (cf. figure 4.22). The quality of the gravity field solution naturally improves since the satellite is getting closer to the masses.

Figure 4.21 shows the groundtrack for months with obviously poor quality and, in comparison, January 2004, which has a particular good coverage. Comparing it with figure 4.20 reveals the connection between the quality of a monthly CHAMP solutions and the groundtrack pattern. The satellite has a particular sparse groundtrack coverage, i.e., the satellite is in a near-repeat orbit.

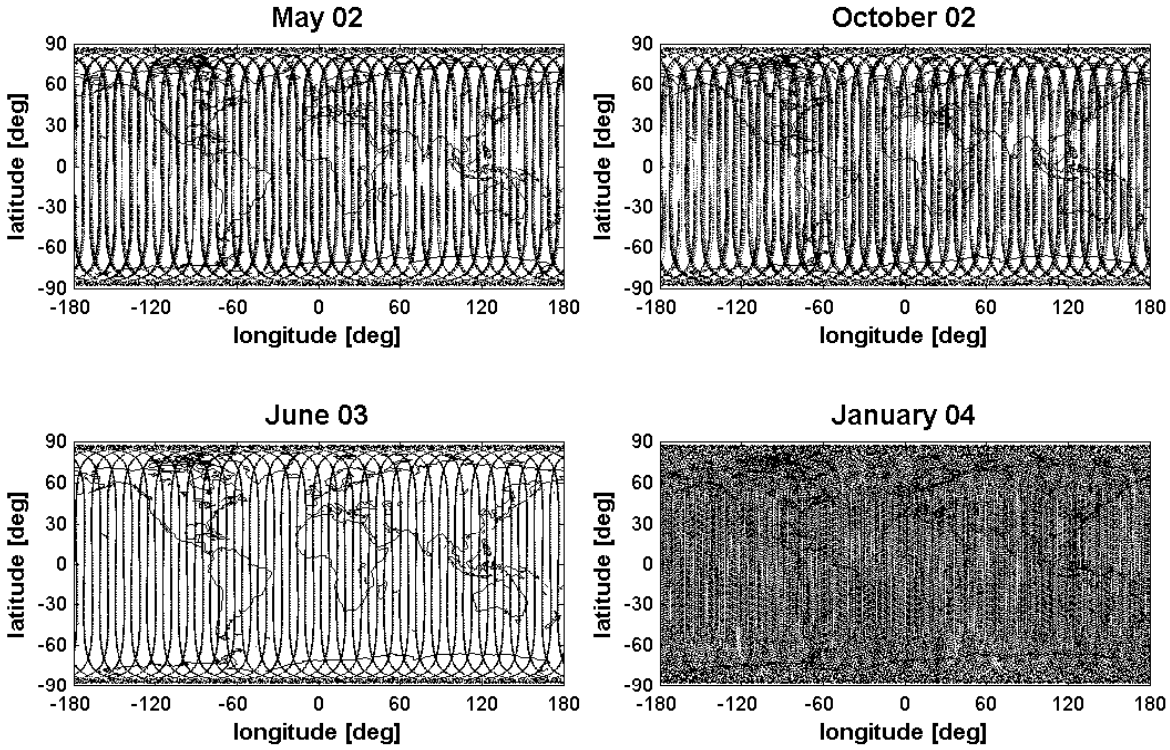

Figure 4.21: Groundtrack coverage: May 02 (top left), October 02 (top right), June 03 (bottom left), January 04 (bottom right)

The variation of the groundtrack coverage is caused by the changing orbit height.

The relation of the orbit height and the gravity field recovery can be understood, if the orbit perturbation spectrum is considered. Since CHAMP is in a near-circular orbit, the simplified perturbation spectrum can be used:

$$\dot{\psi}_{mk} = k\dot{u} + m\dot{\Lambda} \ , \ \text{with} - L \leqslant m, k \leqslant L \ , \tag{4.33}$$

where $\dot{\psi}_{mk}$ is the perturbation frequency and L is the maximum degree of the spherical harmonic representation of the potential. The drift in the argument of latitude $\dot{u}$ is the sum of the perigee drift $\dot{\omega}$ and the change in the mean anomaly $\dot{M}$. The drift in the longitude of the ascending node $\dot{\Lambda}$ is the sum of the nodal drift $\dot{\Omega}$ and the change in the Greenwich Apparent Sidereal Time GA$\dot{\text{S}}$T. For more details and derivations of the simplified perturbation spectrum, the reader is referred to Sneeuw (2000).

The satellite experiences resonances with the gravity field, if the perturbation spectrum becomes equal to zero. Consequently:

$$k\dot{u} = -m\dot{\Lambda} \Rightarrow \frac{k}{m} = \frac{-\dot{\Lambda}}{\dot{u}} = \frac{T_u}{T_\Lambda} = \frac{\alpha}{\beta} \ , \tag{4.34}$$

where T_u denotes the orbital revolution period, T_Λ one nodal day, β the number of revolutions and α the number of nodal days. Since k and m are integers and $\frac{k}{m}$ consequently an integer ratio, the ratio $\frac{\beta}{\alpha}$ is also an integer ratio, i.e., after β revolutions exactly α nodal days have passed. Note that all the ratios need to be relative primes, i.e., they can not have a common divisor. Furthermore, the smaller the relatives primes are, the sparser will be the groundtrack. Geometrically the satellite is in a repeat orbit.

During the months May 2002, October 2002 and June 2003 the satellite is passing through a satellite height of $\approx 400\,\text{km}$ and is experiencing a $\frac{31}{2}$ repeat mode, i.e., the satellite makes 31 revolutions in 2 nodal days. CHAMP is passing three times through this height since it was lifted two times in between (cf. figure 4.22).

Note that the degradation in May and October 2002 seems not as bad as in June 2003, which is related to the choice of the data. In the calculations, one month contained data from the first to the last day of the month. It takes about one month to pass through the repeat mode and for June 2003 the period falls exactly into this month whereas

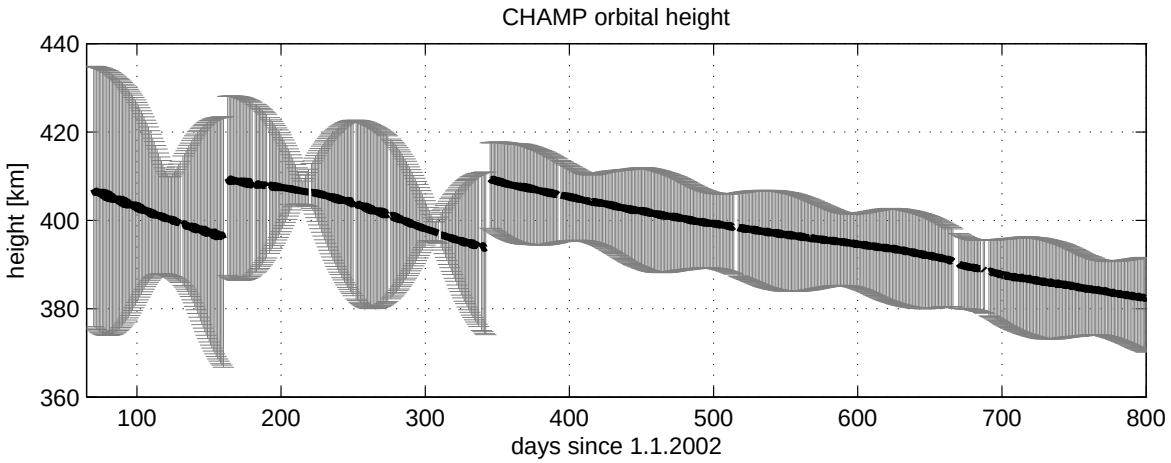

Figure 4.22: Mean orbit height and variability of CHAMP from April 2002 till February 2004

for May and October parts of this repeat mode take place in April and November, respectively, which can also be seen in the poorer performance for these months (cf. figure 4.20).

Yamamoto et al. (2005) investigated a similar effect for the GRACE satellite mission using simulations. In their study they showed that in times of a near-repeat mode the global standard deviations of the geoid height increase up to one order of magnitude and the data distribution is insufficient for a gravity field recovery up to degree and order 30 only.

Wagner et al. (2006) investigated the $\frac{61}{4}$ repeat mode of GRACE in September 2004. They come to the same conclusion and confirm that for a full solution up to degree L the number of orbit revolutions before repeat must be greater than $2L$. Similarly to GRACE, the solutions for CHAMP during the $\frac{31}{2}$ near-repeat mode will also be only valid up to degree and order 30. Since the satellite is still sensing signal beyond degree L, this signal will alias into lower degree coefficients; this is investigated in more detail in the next section.

4.2.5 Aliasing

Comparing the error spectra for January 2004 and June 2003, it is obvious that the groundtrack has a severe influence on the solution (cf. figure 4.23). However, it is

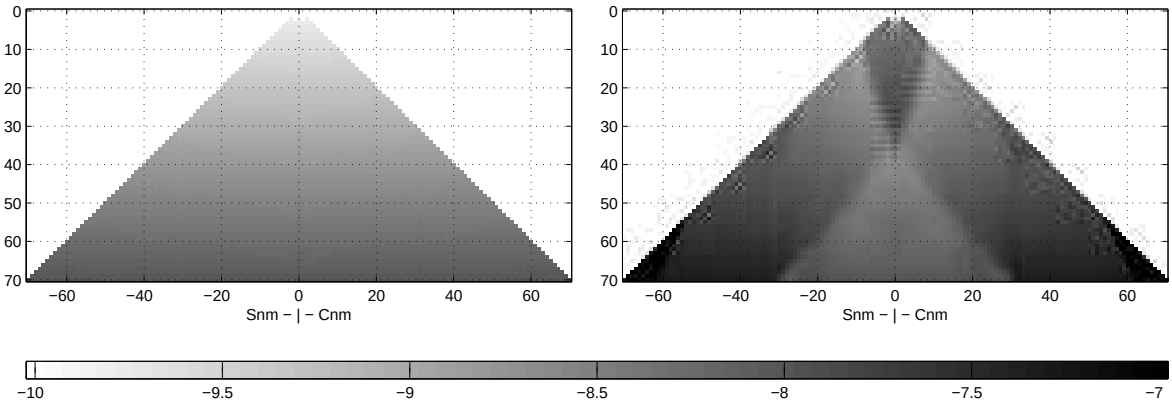

Figure 4.23: Error spectra: monthly solutions for January 2004 (left) and June 2003 (right)

not the only reason for changes in the spectrum. Signal is projected into different parts of the spectrum for various reasons and a clear separation of each cause is not always possible. All these phenomena are referred to as *aliasing* and are many times neither reversible nor preventable. In general, aliasing occurs if the sampling theorem is violated, which states that at least 2 samples are necessary in order to recover one frequency of a signal correctly (Buttkus, 1991). Given a specific sampling, the maximum resolvable frequency is consequently half the sampling frequency $f_{\max}$.

$$f_{\mathrm{Nyq}} = \frac{f_{\max}}{2} \tag{4.35}$$

This frequency is referred to as *Nyquist frequency* and should be only understood as a theoretical boundary. In reality, noise will contaminate the measurements and considerable more samples are necessary in order to recover a signal correctly. Lyons (1997) suggests at least 5 samples as a more realistic rule of thumb.

Before the sampling problem and the subsequent mixed spectral mapping is discussed in more detail, it should be mentioned for the sake of completeness that aliasing is also

caused by:

- signal sampling interactions;
- satellite orbit geometry; and
- omission errors.

In the first case, the satellite senses at a specific time a certain gravity signal. If the satellite is returning next time to this point the input signal changed due to the inherent time-variable parts (Han, 2003, §5). Whether this time-variable part can be recovered or not will depend strongly on the time resolution. Any satellite system will in general deliver measurements with a specific time- and spatial-sampling according to the choice of its instruments and orbit. The full spectral bandwidth of the input signal can normally not be covered. Signal outside the bandwidth needs to be modelled and reduced in a preprocessing step in order to avoid its projection.

As part of the orbit geometry itself the signal strength depends quadratically on the satellite height (Heiskanen and Moritz, 1967). Additionally, polar gaps cause a degradation of the spherical harmonic coefficients. It affects primarily the zonal and near-zonal coefficients and the degradation increases with increasing degree (Sneeuw and van Gelderen, 1997).

Last but not least, the omitted high degree signal aliases into lower frequencies which occurs primarily in the degree-direction of the spectrum (Sneeuw, 2000, §6.3). From the numerical point of view, there is a strong overlap between the omission error and the temporal and spatial aliasing. However, the former is caused by the usage of a deficient model whereas the latter should be understood as the loss of information due to a insufficient sampling.

Temporal and spatial aliasing. It is important to understand aliasing as an undersampling of a signal causing mapping of high frequency content into lower frequencies. The undersampling might occur in a temporal and a spatial sense.

In the first case, the data is seen as a one-dimensional time series along the orbit. CHAMP data is sampled in 30 s steps, which leads to a separation of data points along the track by about 210 km assuming a speed of approximately 7 $^{\mathrm{km}}/_{\mathrm{s}}$. Taking the sampling theorem into account, this would correspond to a degree and order of approximately 90. In reality, due to noise in the data the maximum resolvable degree is lower.

In the second case, the samples are related to the location where the measurements are taken. Spacewise the signal is sampled on a closed surface (sphere). Assuming a sufficient long time period and a static field, the surface could be covered arbitrarily densly. With perfect coverage the aliasing problem would disappear but the data distribution might lead to a biased estimation as was shown by Sansò (1990).

Aiming at the recovery of the gravity field on a monthly basis, the coverage will be dependent on the data distribution within the month. In general, the sampling along the equator is sparser than in polar areas due to the convergence of the orbit tracks. Consequently, the distribution of the equator crossings of the orbit governs the maximum solvable degree.

Figure 4.24 shows the sampling along parallels for a section of 60 ° around the Greenwich meridian. In January the data is spread homogeneously over the equator but in June the measurements are clustered. Obviously, in January sine and cosine functions with higher periodicity can be fitted into the data. The resulting error spectrum is homogeneous. In June 2003, the satellite has 31 revolutions before it is repeating its own track, i.e., the satellite pattern has 62 ascending and descending arcs and the solution is effectively only valid up to degree and order 31. Nevertheless, the satellite is sensing signal beyond degree 31 and, consequently, aliasing occurs primarily in the order-direction of the spectrum.

Jekeli (1996) discusses this thoroughly for the case of gridded simulated data and suggests the usage of spherical cap averages as a de-aliasing filter. Here, the data is given along the orbit and interpolation is to be avoided. The development of corresponding filters for irregular sampled data using, e.g. wavelets, is an interesting aspect for future work. For now, it can only be concluded that the time period in the months May and

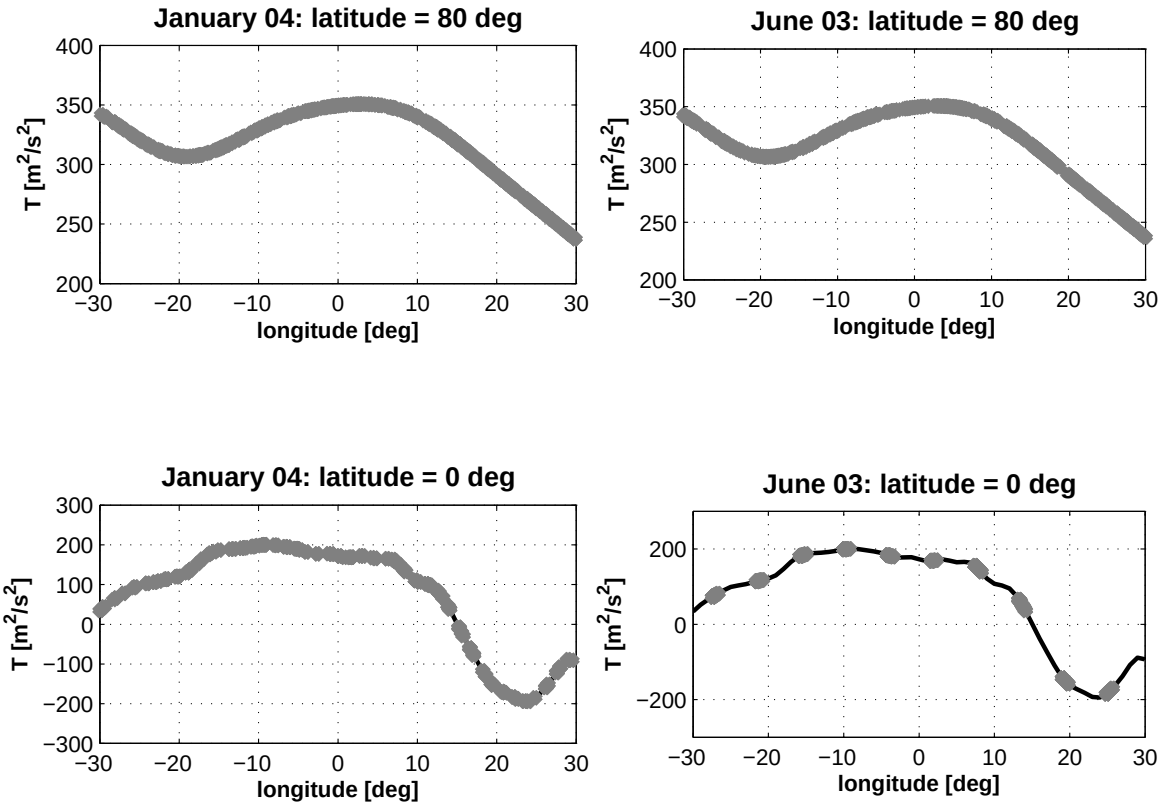

Figure 4.24: Sampling along latitude bands: January 2004 (left) and June 2003 (right)

October of 2002 and June 2003 is not long enough in order to cover the area sufficiently. The situation might be improved only by adding additional data.

Note that due to the convergence of the orbit tracks the sampling at the pole is rather constant, which is one motivation for local calculations in high-latitude areas, cf. chapter 6.

Mixed spectral mapping: Orthogonality of the Legendre Functions. In the measurement process, the two-dimensional gravity field is mapped on a one-dimensional time series along the orbit of the satellite and subsequently into spherical harmonic coefficients. The later step can be done in several ways, e.g., on a torus or on a sphere. Here, a least-squares adjustment on the sphere is used. In the continuous case, the orthogonality property of the Legendre functions ensures the separation into spherical

harmonic coefficients. Sneeuw (1994) showed, among others, that due to the use of discrete data the Legendre function loses its orthogonality property. Depending on the severeness of discretization more and more signal is projected elsewhere instead of the anticipated degree and order. If the exact behavior is known, a weighting matrix could be designed to restore the orthogonality. Sneeuw (1994) demonstrated this for the case of gridded data using the Neumann approach and it might be possible to derive numerically a similar weighting matrix for irregular sampled data. First, the question should be answered whether the loss of orthogonality influences the solution in such a way that the pattern in the error spectra of figure 4.23 can be explained.

The orthogonality property is verified by integrating the multiple of two Legendre functions along the latitude which is approximated by the summation over all measurements when discretized.

$$2\ (2-\delta_{m,0})\ \delta_{ln} = \int_0^{\pi} \bar{P}_{lm}\bar{P}_{nm}\sin\theta d\theta \approx \sum_{i=1}^{N} \bar{P}^i_{lm}\bar{P}^i_{nm}\sin\theta_i\Delta\theta_i \Rightarrow P^T\,W\,P, \qquad (4.36)$$

where δ is the Kronecker symbol and P contains the Legendre functions for a specific order m and all degrees of interest arranged in a matrix and W has the factor $\sin\theta_i\Delta\theta_i$ for each measurement on its main diagonal. This means that for a particular order m a range of degrees can be evaluated and the resultant is a matrix. On its main diagonal, the value should be 2 for $\{l = n, m = 0\}$, 4 for $\{l = n, m \neq 0\}$ and all off-diagonal elements should be zero.

In the following, the order with the largest degradation is used for the investigations. As a measure for the largest effect, the RMS of the matrix P^TWP is determined for $m \in [0 \ldots 70]$ after reducing the nominal value from the main diagonal. It is plotted in figure 4.25. The effect is largest for order 2 and decreases up to order 7 by approximately three orders of magnitude. There is virtually no difference between the RMS of January 2004 and June 2003, which is a first indication that the loss of the orthogonality in the Legendre functions due to discretization is not the reason for the pattern in the error spectrum.

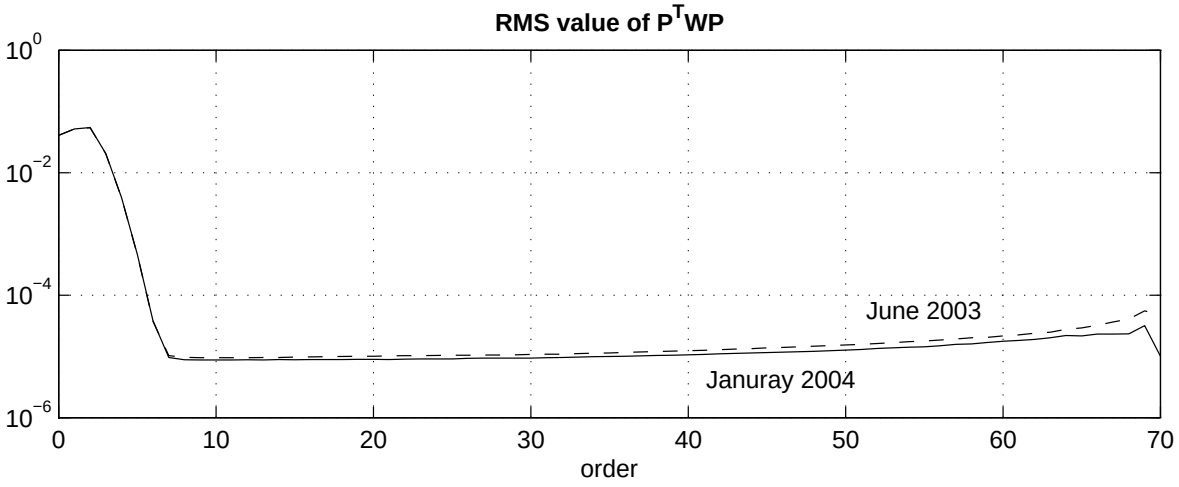

Figure 4.25: RMS of $P^T W P$ as function of the order m

Figure 4.26 shows the orthogonality matrix up to degree 70 for order 2. The month January 2004 is on the left panel and June 2003 on the middle panel. For the first one, 82882 data points are processed and $\Delta\theta$ has an average value of 10.63 arcsec or 349 m at satellite height. In the latter, 80450 data points are used and $\Delta\theta$ is slightly higher with 10.93 arcsec or 359 m. The degree is ordered in $l-m$ even and $l-m$ odd along the x-

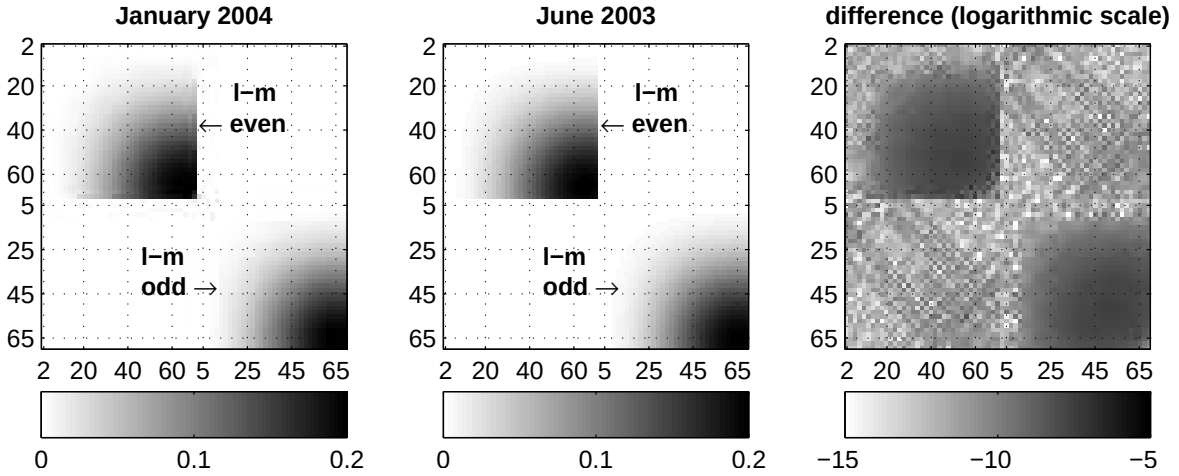

Figure 4.26: Orthogonality matrices for order 2: January 04 (left), June 03 (middle), difference on a logarithmic scale (right)

and y-axis. The diagonal elements have been removed according to equation (4.36) in order to reveal the off-diagonal pattern. In the continuous case these elements are zero and any deviations are a measure of the discretization error. The integration of an even and an odd pair is naturally zero due to the development of the Legendre functions and the numerical evaluation verifies this. The integration of even and odd pairs shows symmetry w.r.t. the main diagonal and an increasing loss with increasing degree. The difference of the two months on the right panel is shown in a logarithmic scale. It reflects the influence of the data distribution on the mapping of the spectral content. The pattern follows the general shape of the other two orthogonality matrices but the magnitude is of the order of 10^{-10}, i.e., the influence is small and barely reflected in the matrix.

The main diagonal is affected similarly to the off-diagonal elements. This is also confirmed in figure 4.27, which shows the difference of the main diagonal to the nominal value of equation (4.36). The difference is small for low degrees and is constantly increasing. This behavior and the drop in figure 4.25 up to order 7 suggests that the influence of the polar gap is reflected in the matrix. The polar gap mainly affects the zonal and near-zonal coefficients.

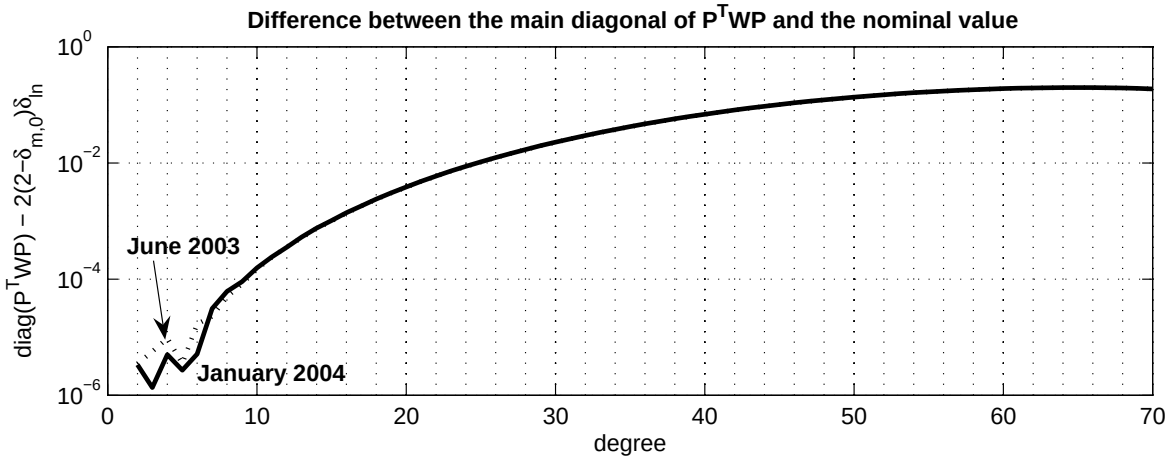

Figure 4.27: Difference between the main diagonal of $P^T\,W\,P$ and the nominal value 2 for order 2.

The loss of orthogonality, though present, is similar for both months and the difference in the error spectra cannot be explained this way. The conclusion is also supported if the number of points are counted in 1°-latitude- and longitude-bands. Looking at the number of points in the latitude direction, figures 4.28 and 4.29 show virtually no difference.

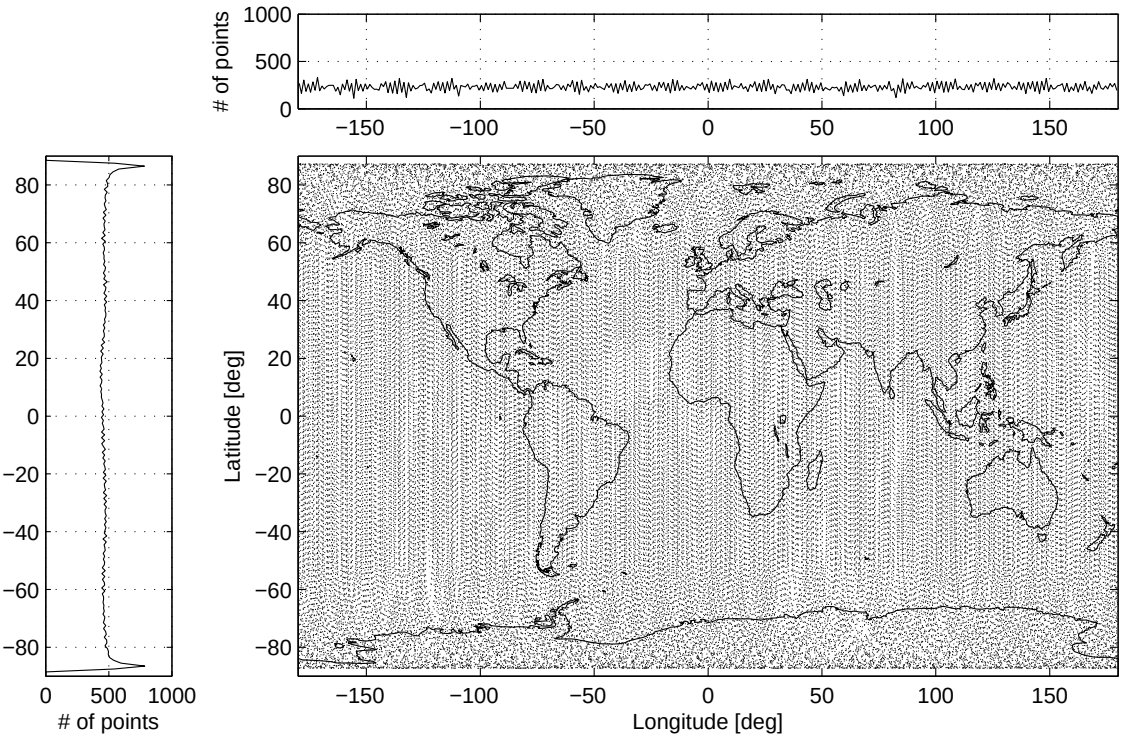

Figure 4.28: Groundtrack and number of points per 1°-band: January 2004

On the other hand, there is a strong modulation in the longitude direction. The data is clustered due to the near-repeat mode and the sparse groundtrack coverage. The longitude direction is evaluated using $\cos m\lambda$ and $\sin m\lambda$, which means that there is no dependency on the degree. Cosine and sine only retain their orthogonality if the data sampling is on an equidistant grid, which is not the case here due to the satellite orbit. The orthogonality can be evaluated similarly to equation (4.36) but different cases for

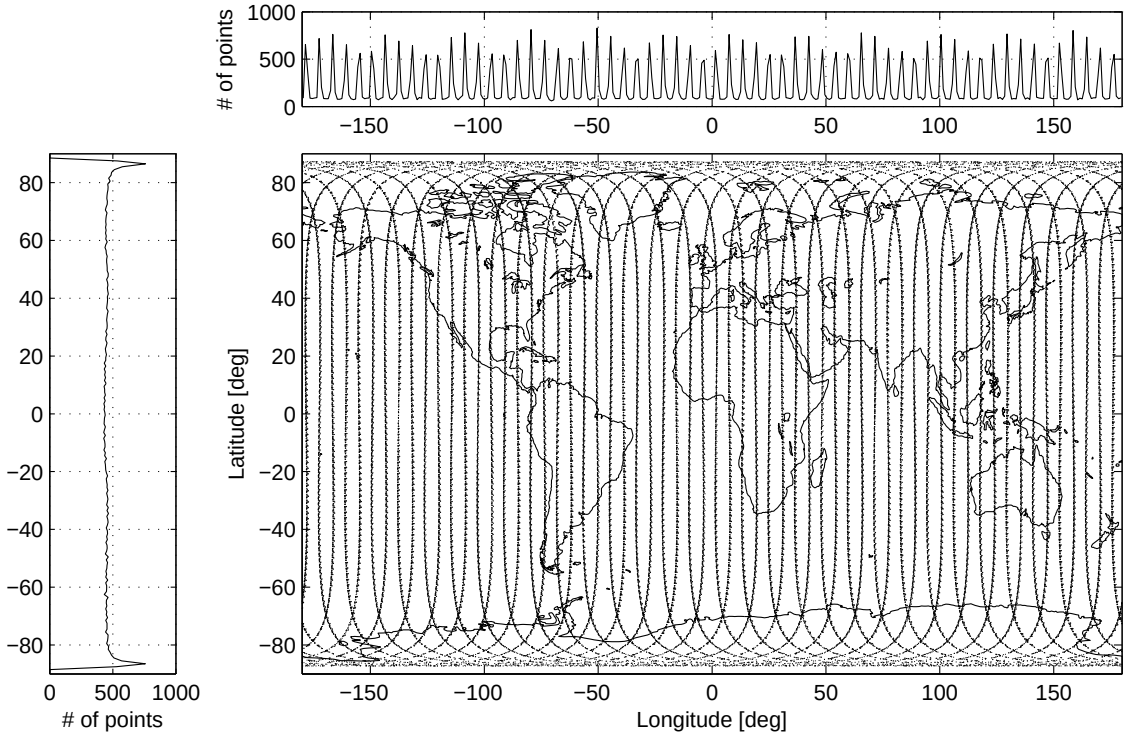

Figure 4.29: Groundtrack and number of points per 1°-band: June 2003

the combination of cosine and sine functions must be evaluated.

$$\begin{aligned}\frac{1}{2}\left(1+\delta_{m,0}\right)\delta_{mk} &= \frac{1}{2\pi}\int_0^{2\pi}\cos\left(m\lambda\right)\cos\left(k\lambda\right)d\lambda \\ &\approx \sum_{i=0}^{N}\cos\left(m\lambda_i\right)\cos\left(k\lambda_i\right)\Delta\lambda_i = C^T\,W\,C\end{aligned} \tag{4.37}$$

$$\begin{aligned}0 &= \frac{1}{2\pi}\int_0^{2\pi}\cos\left(m\lambda\right)\sin\left(k\lambda\right)d\lambda \\ &\approx \sum_{i=0}^{N}\cos\left(m\lambda_i\right)\sin\left(k\lambda_i\right)\Delta\lambda_i = C^T\,W\,S\end{aligned} \tag{4.38}$$

$$\begin{aligned}\frac{1}{2}\left(1-\delta_{m,0}\right)\delta_{mk} &= \frac{1}{2\pi}\int_0^{2\pi}\sin\left(m\lambda\right)\sin\left(k\lambda\right)d\lambda \\ &\approx \sum_{i=0}^{N}\sin\left(m\lambda_i\right)\sin\left(k\lambda_i\right)\Delta\lambda_i = S^T\,W\,S,\end{aligned} \tag{4.39}$$

where C and S contain the cosine and sine functions for all orders of interest and W comprehends the factor $\Delta\lambda$ on its main diagonal. Since the data sampling depends on

the latitude, the orthogonality must be investigated in different latitude bands.

The orthogonality matrices are shown in figure 4.30 for a 10 ° polar band and in figure 4.31 for a 10 ° equator band. The matrices contain in the upper left corner the combination of two cosines (4.37), in the upper right and lower left corner a cosine-sine pair (4.38) and in the lower right corner the combination of two sine functions (4.39). The diagonal elements have again been removed according to equations (4.37)–(4.39) in order to reveal the off-diagonal pattern.

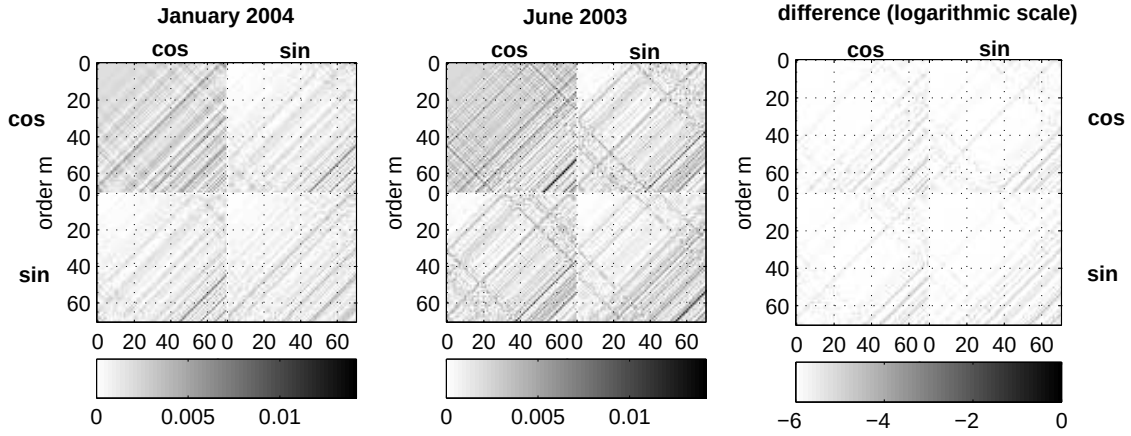

Figure 4.30: Cosine/sine orthogonality matrix for a polar band: $\phi \in [75° \ldots 85°]$

In the high latitude area a loss of orthogonality is visible for both months, but the difference is of the order of 10^{-6}. This means that the irregular data distribution leads to a loss of orthogonality, but the effect again is similar for both months since the data distribution in this area is congenerous (cf. figures 4.28 and 4.29) .

In the equator area the measurements are clustered in June 2003 and, consequently, the effect is maximum. Figure 4.31 shows strong off-diagonal pattern and thus a severe loss in the orthogonality. Cosine pairs are more affected at low orders and sine pairs at high orders, which suggests that low order $\bar{C}_{lm}$-coefficients and high order $\bar{S}_{lm}$-coefficients are more deficient. The error spectrum for June 2003 in figure 4.23, however, does not reveal such behavior. Instead, a symmetric pattern about order 0 is visible. The spectrum seems folded around the center line, i.e., signal of cosine coefficients is

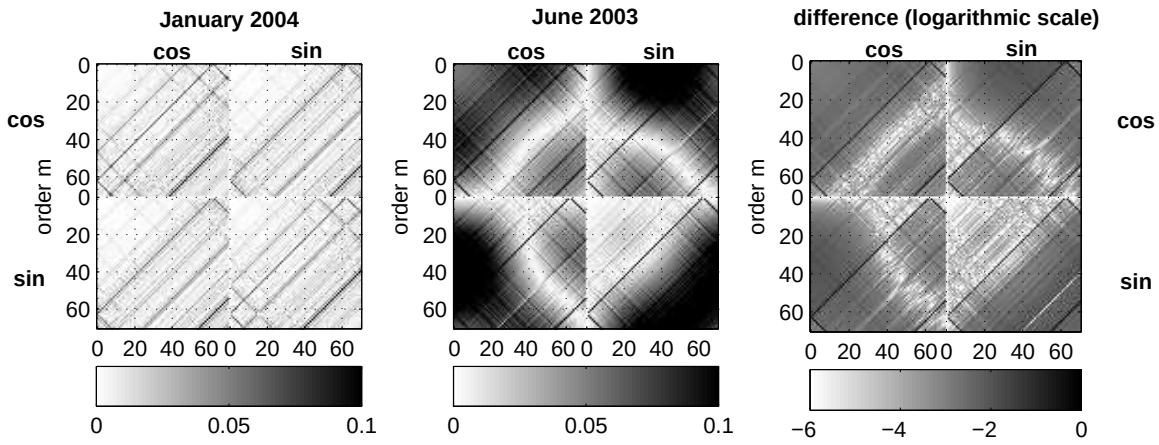

Figure 4.31: Cosine/sine orthogonality matrix for an equatorial band $\phi \in [0° \ldots 10°]$

mapped to sine coefficients and vice-versa. This effect can be explained by the cosine-sine combinations. In particular, the cosine at orders 0 to 20 and the sine at orders 20 to 40 show strong deviations from their nominal value of zero. This means that either low-order cosine signal is mapped into mid-order sine coefficients or vice versa, and might be an explanation for the triangularly shaped pattern.

In conclusion, it has been shown that the loss of orthogonality of the Legendre functions is not responsible for the pattern in the error spectrum but most likely it is the behavior of the cosine and sine functions. The situation is very complicated, however, since the data distribution varies along the latitude and, consequently, there is loss of orthogonality as well. Aside from this, both functions are processed here in one step, which makes the numerical determination of a weighting matrix difficult. For future work, it should be investigated if the separation into two steps and thus the separation of Legendre and cosine/sine functions is more favorable. The theoretical framework for the spherical harmonic analysis using two steps is outlined in Colombo (1983).

4.3 Combination of single satellite missions

In the last sections it was shown that the groundtrack pattern is responsible for the degradation of the monthly solutions. Currently, the situation can only be improved by adding information which can either come from terrestrial measurements or, more importantly, from other satellite missions. Ideally, the added measurements should be taken globally in the same period as the CHAMP data with similar accuracy. The GRACE mission enables exactly this. Note that for this case study the K-band measurement is **not** used. Instead, each of the two GRACE satellites is considered as a single satellite mission of the CHAMP-type. Before looking at the combination of the data, the monthly variability of the GRACE data is analyzed.

Figures 4.32 and 4.33 show, similar to figure 4.20 for the case of CHAMP, the RMS of the geoid height differences w.r.t. GGM02s for the monthly solutions of GRACE A and GRACE B, respectively. The solutions start in August 2002 due to data availability. Consequently, the situation for May 2002 cannot be improved. Data for the months of December 2002 and January 2003 is also not published, most likely due to poor quality. With the exception of September 2002, when the satellites were passing a $\frac{76}{5}$ repeat mode (Ameele, 2004) and the spatial distribution of the data was sparse, the solutions are more consistent but generally worse than CHAMP-only ones due to the altitude of GRACE. The two GRACE satellites were at a higher orbit for the period of interest and, assuming a similar error level, the downward continuation will amplify the noise more in case of GRACE than in the case of CHAMP.

Figure 4.34 shows the spread of the monthly solutions in a degree-RMS plot and yields the same conclusion. The lower limit is defined by the minimum difference and the upper limit by the maximum difference to GGM02s. CHAMP has the widest spread but also the best solution especially for higher degrees due to its lower orbit. For the two GRACE satellites, the downward continuation yields an increasing degradation with increasing degree.

Clearly, the question of an optimal combination of the data arises. The simplest

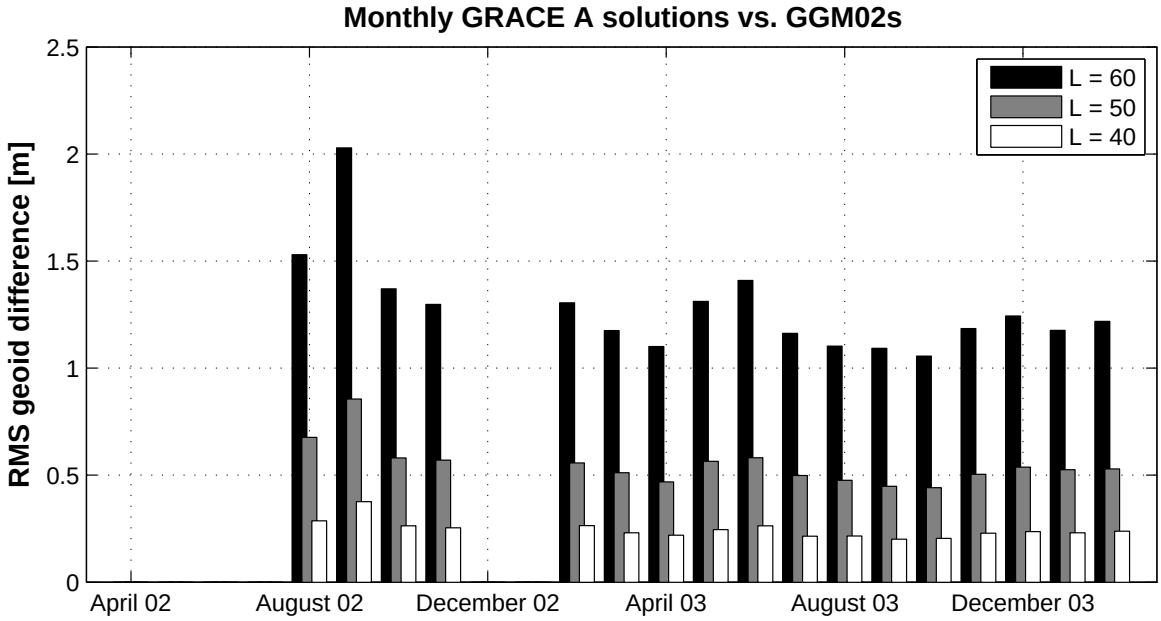

Figure 4.32: RMS of the geoid height difference between GRACE A monthly solutions with respect to GGM02s

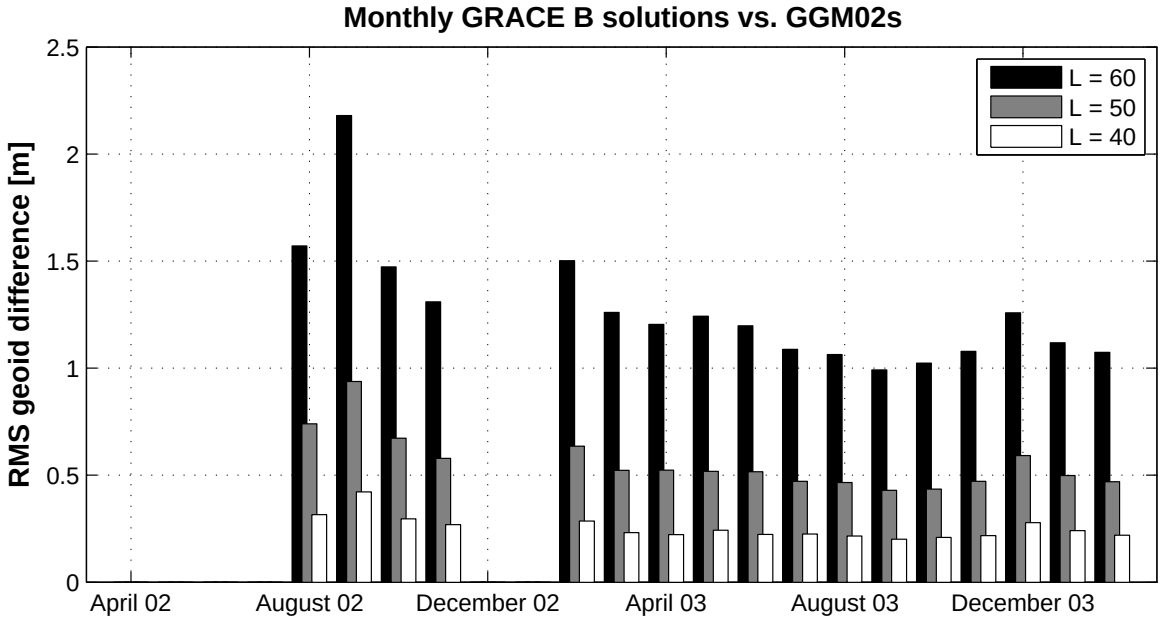

Figure 4.33: RMS of the geoid height difference between GRACE B monthly solutions with respect to GGM02s

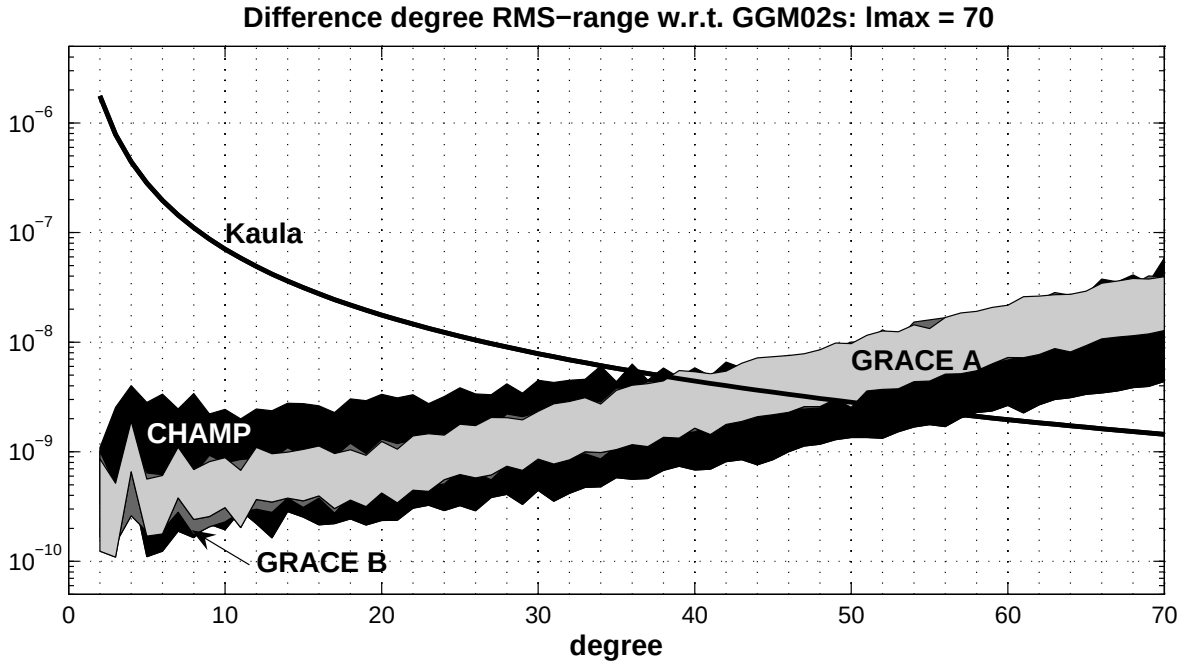

Figure 4.34: Spread of the difference degree RMS of the monthly solutions

approach is to combine the data with equal weight but especially for months with a dense groundtrack coverage the combined solution will be worse than a CHAMP-only solution. The ratio between GRACE and CHAMP data is 2:1 which results in an undesired bias towards GRACE. The downward continuation effect will then worsen the results.

Lerch (1991) suggested the usage of subset least-squares solutions. The differences between a subset and the complete solution should be in agreement with their error estimates which is achieved by adjusting the weights. Applying this method to CHAMP and GRACE, the solution did not converge and, instead, the method of variance component estimation was employed.

Variance component estimation. Variance component estimation enables the combination of different data types using relative weights between the variance factors σ_i^2 of each subset i of the data. Subsets can either be formed from the same data source, e.g., monthly solutions of CHAMP, or by different types of data. Therefore, variance

component estimation provides the platform for the combination with terrestrial, airborne, shipborne and altimetry data for future applications. The applied methodology follows closely the one outlined in Koch and Kusche (2002) except that regularization is not included here and a stochastic trace estimation is not necessary. The estimates of the unknown parameters $\hat{\boldsymbol{x}}$ are calculated from

$$\left(\frac{1}{\sigma_1^2}\,A_1^T\,P_1\,A_1 + \frac{1}{\sigma_2^2}\,A_2^T\,P_2\,A_2 + \ldots\right)\hat{\boldsymbol{x}} = \frac{1}{\sigma_1^2}\,A_1^T\,P_1\,\boldsymbol{l}_1 + \frac{1}{\sigma_2^2}\,A_2^T\,P_2\,\boldsymbol{l}_2 + \ldots \tag{4.40}$$

Introducing the ratio $\omega_i = \sigma_1^2/\sigma_i^2$ which expresses the relative weighting of the observation $\boldsymbol{l}_i$ with respect to $\boldsymbol{l}_1$, yields:

$$\left(A_1^T\,P_1\,A_1 + \omega_2\,A_2^T\,P_2\,A_2 + \ldots\right)\hat{\boldsymbol{x}} = A_1^T\,P_1\,\boldsymbol{l}_1 + \omega_2\,A_2^T\,P_2\,\boldsymbol{l}_2 + \ldots \tag{4.41}$$

The variance factors σ_i^2 are unknown random parameters since the weighting of different types of observations is normally unknown. They are estimated iteratively in a best invariant quadratic unbiased estimation (BIQUE) from

$$\hat{\sigma}_i^2 = \frac{\hat{\boldsymbol{v}}_i^T\,P_i\,\hat{\boldsymbol{v}}_{\boldsymbol{i}}}{r_i}, \tag{4.42}$$

where $\hat{\boldsymbol{v}}$ are the residuals after one calculation step and r_i is the partial redundancy of one subset of observations. It denotes the contribution of this subset i to the solution and can be calculated as:

$$r_i = n_i - \mathrm{tr}\left(\frac{1}{\hat{\sigma}_i^2}\,A_i^T\,P_i\,A_i\,N^{-1}\right), \tag{4.43}$$

where n_i is the number of observation in the subset, "tr" the trace operator and N the normal matrix of the complete solution. As discussed in section 4.1.2, the measurements are assumed to be of equal accuracy due to the lack of the covariance information. Consequently, the weight matrix P_i is the unit matrix. Koch and Kusche (2002) continue with a stochastic trace estimation, which is necessary if the inverse of the normal matrix N^{-1} is not available. This can be the case if the equation system is not inverted but only solved by, e.g., a preconditioned conjugate gradient method, which might be interesting for the case of GRACE including the K-band. In this application, the inverse of N is available and a stochastic trace estimation is therefore not necessary.

Monthly CHAMP/GRACE gravity field recovery. Subsequently, the monthly solutions are analyzed and compared again in different domains. The first and maybe most impressive one is the comparison of the RMS of the difference between the combined CHAMP/GRACE monthly solutions and GGM02s (figure 4.35). The figure should be

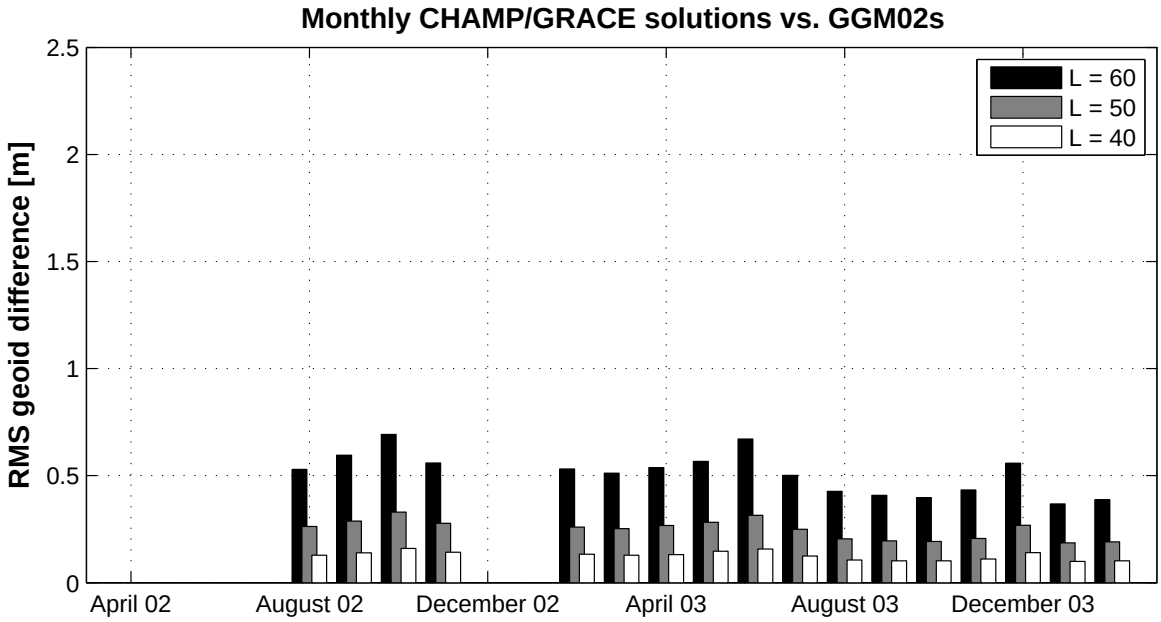

Figure 4.35: RMS of the difference between the combined CHAMP/GRACE monthly solutions and GGM02s in terms of geoid height

compared to the CHAMP-only (fig. 4.20), GRACE A-only (fig. 4.32) and the GRACE B-only solutions (fig. 4.33). The scale is kept the same throughout all four graphs for easy comparison. The RMS of all the months is relatively constant about 0.5 m with a small variability around ± 0.2 m. Clearly, the monthly solutions are vastly improved, especially the months with poor groundtrack coverage, though the effect is still visible. In October 2002 and June 2003 the RMS dropped from 1.4 m and 2.5 m, respectively, to 0.7 m for degree 60, which is an improvement by a factor of 2 to 3.5. The trend due to the decreasing orbit height is still visible. This suggests that the combination can reduce the influence of the groundtrack pattern but cannot improve significantly the inherent problem of the downward continuation and the error propagation.

The second point of view is the spread between the best and the worst difference degree-RMS w.r.t. GGM02s. Figure 4.36 shows for easy comparison the spread of all three

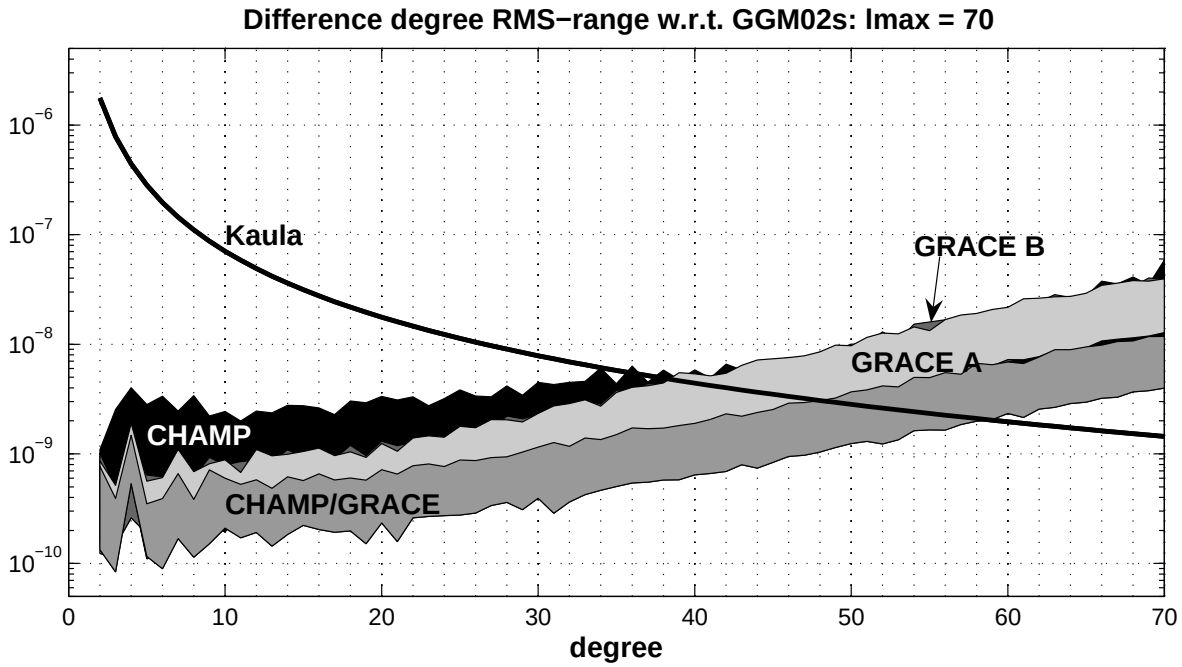

Figure 4.36: Spreading of the monthly solutions

single satellite solutions and of the combined solution. Obviously, the combination gives the best of both worlds. GRACE data reduces the spread of the CHAMP-only solutions by one order of magnitude. At the same time, the downward continuation effect in the GRACE-solutions is improved by CHAMP. The combined solutions are, therefore, more consistent and homogeneous, which is important for time-variable investigations.

The question is whether the combined solutions show any time-variable patterns. Figure 4.37 shows the monthly solution for the period of March 2003 to February 2004. As seen above, due to the decreasing orbit height these results should be the best available.

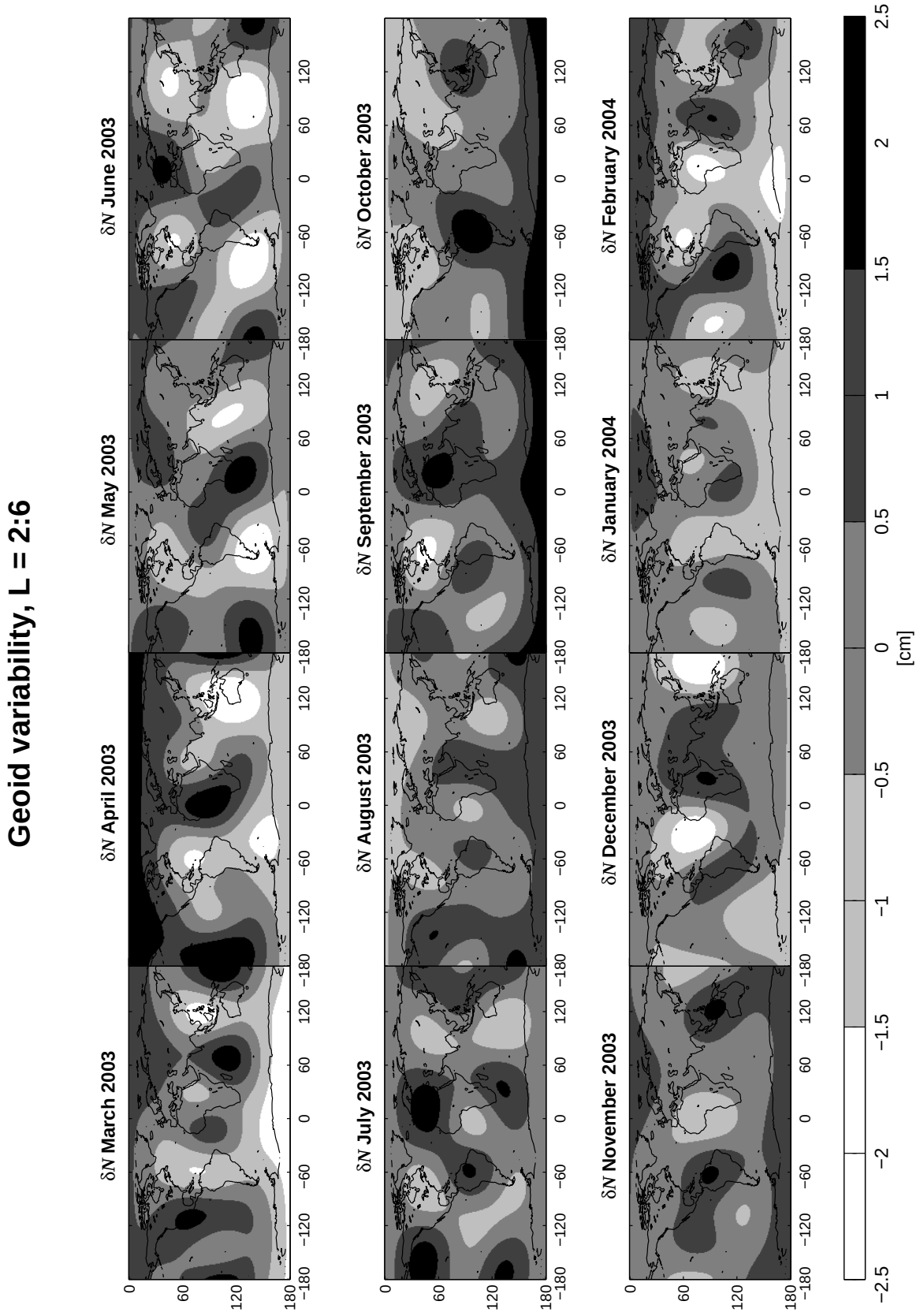

Figure 4.37: Variability in geoid height for low degree harmonics: March 2003 - February 2004

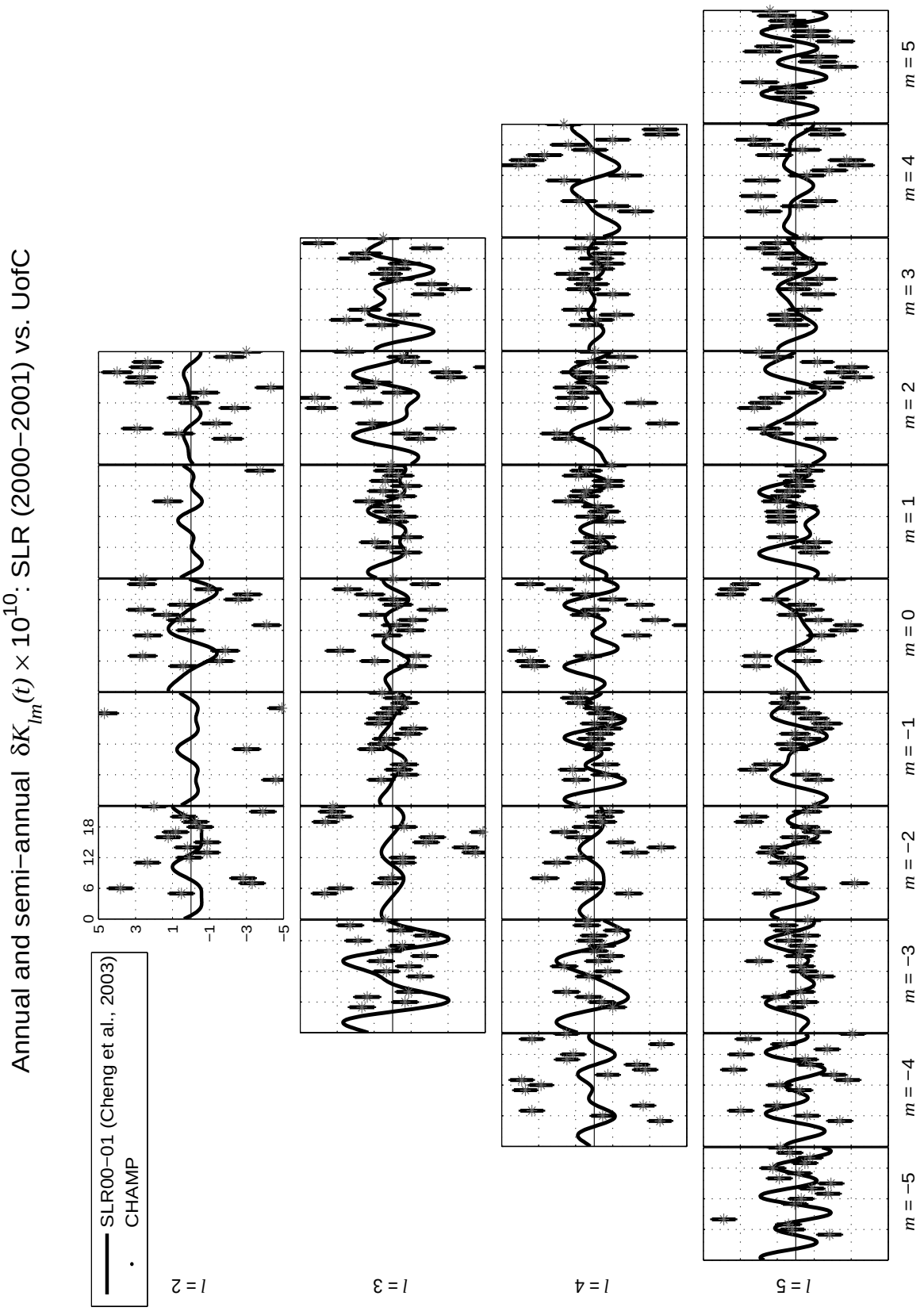

Figure 4.38: Comparison of low degree harmonics with SLR from Cheng et al. (2004): March 2003 - February 2004

The two-year solution UofC is again removed as an average field and only the very low degrees 2 to 6 are shown. The northern hemisphere shows an increase in the geoid height for the months of March and April 2003, and January and February 2004. The southern hemisphere experiences a decrease at the same time. Since the summer months show the opposite behavior, it could be an indication for mass redistribution with an annual cycle and a signal range of ± 2 cm. The Amazon basin shows now a more consistent behavior throughout the year, as well. During the winter and spring months, there is a decrease in the geoid height visible; in the summer and fall months, there is an increase. Unrealistic, however, seem the variations over Europe and northern Africa.

The comparison with the SLR data from Cheng et al. (2004) (figure 4.38) also shows improved results but only single coefficients have a similar behavior as the SLR data, e.g., the order one terms with the exception of degree 2. Other coefficients experience a phase shift like, e.g., $\bar{C}_{52}$ and $\bar{S}_{33}$, and some like $\bar{C}_{22}$ or $\bar{S}_{44}$ show again completely random behavior.

l = 2				1.91	16.52	2.40	18.04	2.55			
l = 3			1.97	2.50	0.80	1.36	0.96	1.81	2.13		
l = 4		3.24	1.55	1.52	1.05	3.33	0.75	1.66	0.70	2.79	
l = 5	2.07	2.50	1.12	1.41	1.61	2.54	1.13	2.21	0.76	1.88	1.87
	m=-5	m=-4	m=-3	m=-2	m=-1	m=0	m=1	m=2	m=3	m=4	m=5

Table 4.2: Difference RMS between $\delta K_{lm}^{\mathrm{SLR}}(t) \times 10^{10}$ and $\delta K_{lm}^{\mathrm{CHAMP/GRACE}}(t) \times 10^{10}$

Table 4.2 shows again the difference RMS between the low degree harmonics derived from the combined solution and the SLR model. It confirms the improvement in the comparison. Table 4.3 shows the relative improvement in the difference RMS between the low degree harmonics derived from the combined solution and the one from the CHAMP-only solution. With the exception of S_{21}, C_{21} and S_{51}, the improvement is between 44% and 90%.

l = 2				61.2	-11.4	52.3	-8.8	48.4			
l = 3			78.0	43.9	69.3	79.4	89.4	71.2	60.6		
l = 4		74.4	82.3	56.7	90.3	54.7	89.8	62.1	88.6	58.6	
l = 5	84.5	44.4	73.8	69.5	-1.8	61.8	84.4	65.3	77.0	56.7	78.5
	m=-5	m=-4	m=-3	m=-2	m=-1	m=0	m=1	m=2	m=3	m=4	m=5

Table 4.3: Relative improvement in the difference RMS of $\delta K_{lm}(t) \times 10^{10}$ in percentage

Summarizing, the recovery of the time-variable signal cannot be considered conclusive. The situation improved in comparison to the CHAMP-only solution and some patterns seem reasonable. Yet, a clear identification of an annual or semi-annual signal in the coefficients is only possible for individual coefficients. The results suggest that the monthly solutions are now most likely at the edge of the recoverability of a time-variable signal. Nevertheless, the signal is still contaminated, though minimized, by the influence of the groundtrack. Furthermore, the overall accuracy and, in particular, the noise level in the velocity determination still prevents the successful derivation of a time-variable signal from CHAMP.

As a final comparison, one can take a look at the weighting factors themselves. Especially in June 2003 the CHAMP solution should be downweighted, which is the case (cf. figure 4.39). Interestingly, the two GRACE satellites do not have the same or similar weight in some months. This is on the one hand related to the data availability and on the other hand to the instrumentation of the satellites itself. For example, the atomic clock onboard GRACE A is known to be problematic.

Initially, September 2002 was identified as a month of poor performance for the GRACE-system. Nevertheless, the weighting between the GRACE satellites and CHAMP is approximately equal. This and the remaining effect of the groundtrack in figure 4.35 could be an indication that the combination is still not optimal. In fact, the variance component estimation as discussed in Koch and Kusche (2002) uses the residuals of the reconstructed signal from the combined model with the measurements. This primarily

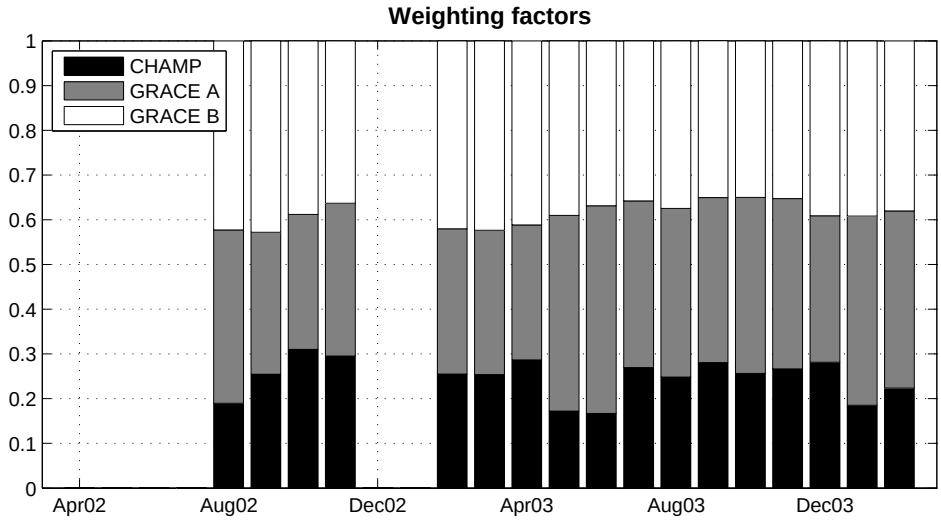

Figure 4.39: Relative weighting factors for each combined month

gives insight into the internal fit of the solution. All the comparisons in the spatial and spectral domain are done with external data (GGM02s), which suggests that the method can be improved by introducing external information. Further, one variance factor is determined for each subset. The influence of the groundtrack, however, is not equal for all coefficients. A degree- and/or order-dependent weighting scheme would be more desirable.

Global gravity field recovery using two years of CHAMP and GRACE data. The combination of the two satellite systems can also be applied to the full set of data in order to derive an improved mean solution. Figure 4.40 shows similar to figure 4.16 the comparison of the combined CHAMP/GRACE solution to UofC as a difference spectrum to GGM02s. The two solutions are very similar except for the very low degrees. The high degrees show a slightly smaller noise level, but obviously the solution has more problems with the degree 2 and degree 4 terms, which is an interesting observation. The two satellite systems are affected similarly which might be an indication that the error is not specific to the CHAMP satellite system. Since both satellites are processed in the same way, likely the error is hidden in the data processing (including the GPS-data

processing) and must be investigated in the future.

On the other hand, only a minor improvement can be expected from the combination. It yielded improved monthly solutions because of the improved data distribution. Over the two years, the data is well distributed for both the CHAMP-only and the combined case. The limiting factor is the velocity determination. The figure proves also the usefulness and reliability of the comparison with a different data source. The variances of the combined solutions are clearly better since about 3 times the amount of data is used. However, the variances indicate only the internal fit whereas the difference

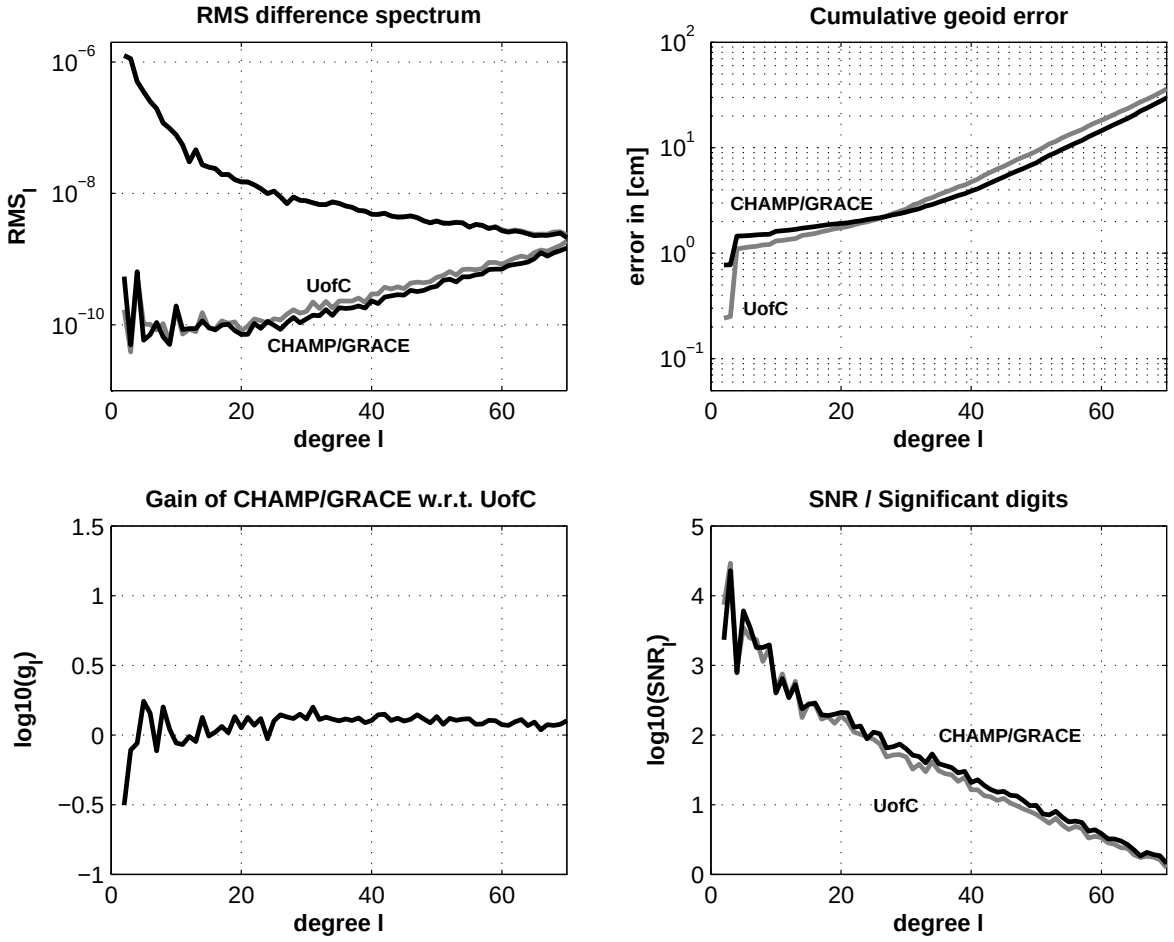

Figure 4.40: Difference spectrum w.r.t. GGM02s: degree RMS (top left), cumulative geoid error (top right), gain of combined solution w.r.t. UofC (bottom left), significant digits (bottom right)

spectrum shows the limit of the data.

4.4 Summary

In this section, the energy integral is derived from the equation of motion in a moving reference frame. The error analysis shows that the limiting factor is the velocity determination, either dynamically or by numerical differentiation from kinematic positions. The data processing includes the preprocessing of the data, the derivation of ancillary quantities like, e.g., tides, the application of the energy principle, the accelerometer calibration with a priori data, and the subsequent least-squares adjustment.

From two years of kinematic data, the solution UofC is derived and compared to EGM96, TUM2s and GGM02s. The solution shows an improved behavior in the low degrees up to degree and order 40 due to the improved calibration procedure. The derivation of monthly CHAMP-only gravity fields does not provide the anticipated time variability of the gravity field. The degradation is caused mainly by the groundtrack pattern, which causes aliasing of the gravity signal. The solutions in months with sparse groundtrack coverage are effectively only valid up to degree and order 31, which is related to the repeat mode of 31 orbits within 2 revolutions of the Earth. The loss of orthogonality due to the discretization of the Legendre functions is present but similar for all months, and is therefore not causing the degradation. On the other hand, a severe loss of orthogonality of cosine and sine functions is observable in equatorial areas.

Combining CHAMP data with GRACE data, where the two GRACE satellites are considered as two independent satellites, yields improved monthly solutions due to an improved data distribution. However, the determination of time variability is inconclusive so far. The two year combined solution also does not show any improvement compared to the CHAMP-only solution. The combination minimizes the effect of the groundtrack pattern but cannot remove the inherent problem of noise amplification due to downward continuation.

Chapter 5

Global gravity field recovery from low-low satellite-to-satellite tracking

This chapter starts in section 5.1 with the application of the energy integral to the case of a low-low satellite-to-satellite tracking mission. The derivation in the Earth-fixed frame is shown in section 5.1.1. Particular emphasis is placed on the exact representation of the kinetic energy in terms of the K-band measurement. The sensitivity to the input quantities is investigated in section 5.1.2. The newly developed concept of the exact representation is proven in section 5.2 and the feasibility of processing real GRACE data is investigated in section 5.3.

5.1 Energy balance approach for the low-low case

In the low-low satellite-to-satellite tracking case, the relative motion of the two satellites is measured with a highly accurate microwave ranging system (K-band) in addition to the positions and velocities of two satellites which are constantly measured by GPS. The system is implemented in the GRACE satellite mission, and the recent gravity field GGM02s outperforms CHAMP-solutions by a factor of 10. Error estimates indicate a 1 cm geoid height at spherical harmonic degree 70 or 285 km half wavelength (Tapley et al., 2005). The solutions are derived using a conventional dynamic orbit and a gravity adjustment process using least-squares. The objective of this section is to investigate the applicability of the energy balance approach to the GRACE system, i.e., to incorporate the K-band measurement into the approach and to investigate its error behavior and its feasibility. Jekeli (1999) derived the energy integral for the case of GRACE in the inertial frame. Part of this derivation is the approximation of the gravitational potential

difference V_{12} by

$$V_2 - V_1 \equiv V_{12} \approx |\dot{\boldsymbol{x}}_1|\dot{\rho}_{12}, \tag{5.1}$$

where $\dot{\boldsymbol{x}}_1$ is the velocity of the first satellite and $\dot{\rho}_{12}$ the range rate between the two satellites. The motivation here is to derive the energy integral in the Earth-fixed frame, as in section 4.1 for the case of a single satellite mission, and to incorporate an *exact* representation of the gravitational potential difference in terms of the K-band measurement.

5.1.1 Derivation

The energy balance approach is applicable to each of the two satellites as was already shown in section 4.3. The difference yields:

$$T_2 - T_1 \equiv T_{12} = E_{12}^{\text{kin}} - U_{12} - Z_{12} - \int \left(\boldsymbol{f}_2 - \boldsymbol{f}_1 + \sum_i \left(\boldsymbol{g}_2^i - \boldsymbol{g}_1^i \right) \right) d\boldsymbol{x} - c_{12}, \tag{5.2}$$

where the subscript '12' always denotes the difference of one component of the second satellite minus the same component of the first satellite. Otherwise, the notation is kept consistent with the energy integral in equation (4.8). In order to find a connection between the potential at the position of the two satellites and their relative motion, the geometry of the system needs to be understood (figure 5.1). The two satellites are travelling with velocities $\dot{\boldsymbol{x}}_1$ and $\dot{\boldsymbol{x}}_2$, respectively. Their relative velocity $\dot{\boldsymbol{x}}_{12} = \dot{\boldsymbol{x}}_2 - \dot{\boldsymbol{x}}_1$ is projected onto the line of sight, which is expressed as the direction vector $\boldsymbol{e}_{12}$. The result is the relative velocity $\dot{\rho}$ in the along track direction. This is the K-band measurement. On the other hand, the distance between the two satellites is the projection of the relative position vector onto the line of sight:

$$\boldsymbol{x}_{12} = \rho \boldsymbol{e}_{12} \tag{5.3}$$

Taking the derivative splits the relative velocity vector into the alongtrack measurement $\dot{\rho}\boldsymbol{e}_{12}$ and a crosstrack part $\boldsymbol{c} = \rho\dot{\boldsymbol{e}}_{12}$:

$$\dot{\boldsymbol{x}}_{12} = \dot{\rho}\boldsymbol{e}_{12} + \rho\dot{\boldsymbol{e}}_{12} \tag{5.4}$$

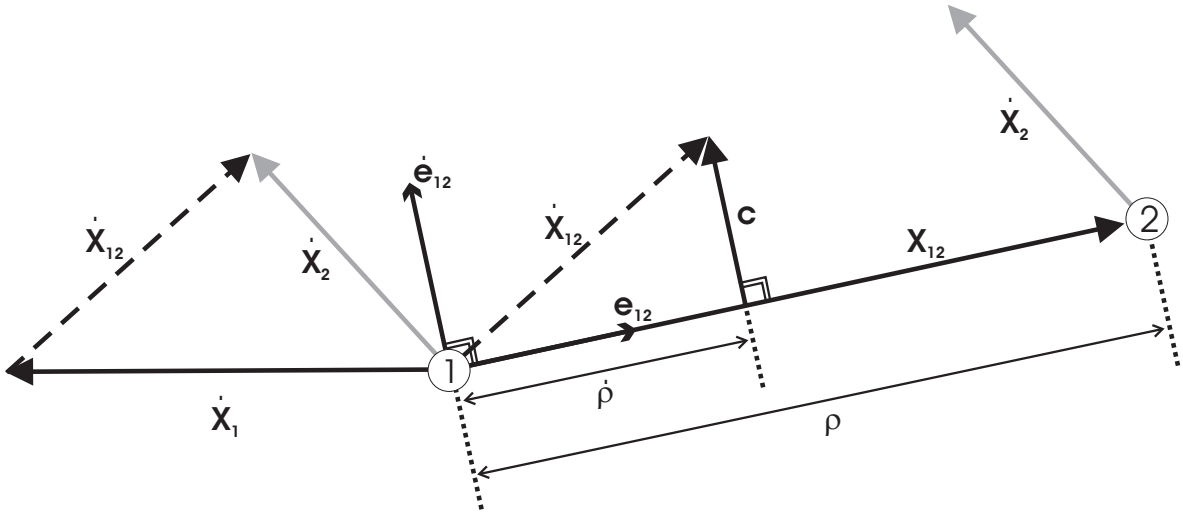

Figure 5.1: Geometry of the GRACE systems, from Rummel et al. (1978)

The crosstrack term is perpendicular to the line of sight and is represented by the change of the direction vector $\dot{\boldsymbol{e}}_{12}$, which does not necessarily have unit length. Having an expression for the relative velocity, this term can be combined with the kinetic energy term. The latter contains the difference of the squared velocity for each satellite and can be expanded as follows:

$$E_{12}^{\text{kin}} = \frac{1}{2}\left(|\dot{\boldsymbol{x}}_2|^2 - |\dot{\boldsymbol{x}}_1|^2\right) = \frac{1}{2}\left(\dot{\boldsymbol{x}}_2 - \dot{\boldsymbol{x}}_1\right)^T\left(\dot{\boldsymbol{x}}_2 + \dot{\boldsymbol{x}}_1\right). \tag{5.5}$$

Inserting equation (5.4) in (5.5) yields:

$$E_{12}^{\text{kin}} = \frac{1}{2}\left[\dot{\rho}\left(\dot{\boldsymbol{x}}_2 + \dot{\boldsymbol{x}}_1\right)^T \boldsymbol{e}_{12} + \rho\left(\dot{\boldsymbol{x}}_2 + \dot{\boldsymbol{x}}_1\right)^T \dot{\boldsymbol{e}}_{12}\right] \tag{5.6}$$

which is an exact representation of the relative kinetic energy in terms of the microwave measurement.

Wolff (1969) suggested to approximate equation (5.6). Half the sum of the velocities of the two satellites is equal to the mean velocity $\dot{\bar{\boldsymbol{x}}}$ of the two satellites and, assuming the distance to be small, the relative velocity will primarily be in the alongtrack direction. Considering all other terms in equation (5.2), it simplifies to:

$$T_{12} \approx \dot{\rho}|\dot{\bar{\boldsymbol{x}}}| - U_{12} - Z_{12} - \ldots \tag{5.7}$$

which is a rough approximation for the system. Wolff (1969) developed his model in 1969, when a meter accuracy in geoid height was acceptable.

Nowadays, millimeter accuracy or better is expected for GRACE, and this method needs to be refined. Jekeli (1999) used the same basic equation as Wolff but applied it to residuals of the disturbing potential ΔT_{12}, i.e., a reference orbit was subtracted at first. The reference data must consequently also be subtracted from the microwave measurement which yields the basic model:

$$\Delta T_{12} = T_{12} - T_{12}^0 = \Delta\dot{\rho}|\dot{\boldsymbol{x}}| \tag{5.8}$$

Han et al. (2003) proved the feasibility of static and time-variable gravity field recovery using this approach with simulations and investigated several aliasing phenomena. Nevertheless, the approach can still be considered an approximation and the exact representation in equation (5.6) should outperform it if all elements are available with sufficient accuracy.

5.1.2 Error analysis

The first step in the validation of the approach is the error analysis of the kinematic energy term or, similarly to section 4.1.2, answering the question: *How precise does each component need to be known?* Using the Cauchy-Schwarz inequality, the partial derivatives w.r.t. the range-rate $\dot{\rho}$, the range ρ and the magnitude of each velocity $|\dot{\boldsymbol{x}}_i|$ are given as:

$$\text{range-rate:} \quad \frac{\partial E_{12}^{kin}}{\partial\dot{\rho}} \leqslant \frac{1}{2}\,|\dot{\boldsymbol{x}}_2 + \dot{\boldsymbol{x}}_1| \tag{5.9}$$

$$\text{range:} \quad \frac{\partial E_{12}^{kin}}{\partial\rho} \leqslant \frac{1}{2}\,|\dot{\boldsymbol{x}}_2 + \dot{\boldsymbol{x}}_1|\,|\dot{\boldsymbol{e}}_{12}| \tag{5.10}$$

$$\text{velocity:} \quad \frac{\partial E_{12}^{kin}}{\partial|\dot{\boldsymbol{x}}_i|} \leqslant \frac{1}{2}\,(\,\dot{\rho} + \rho|\dot{\boldsymbol{e}}_{12}|\,) \tag{5.11}$$

The error estimates are shown in figure 5.2. Note that for the range-rate the unit of the y-axis is [μm/s], for the range [cm] and for the velocity [mm/s]. The aspired accuracy in geoid height is 1 mm which is denoted by the first vertical black line. Accordingly, the

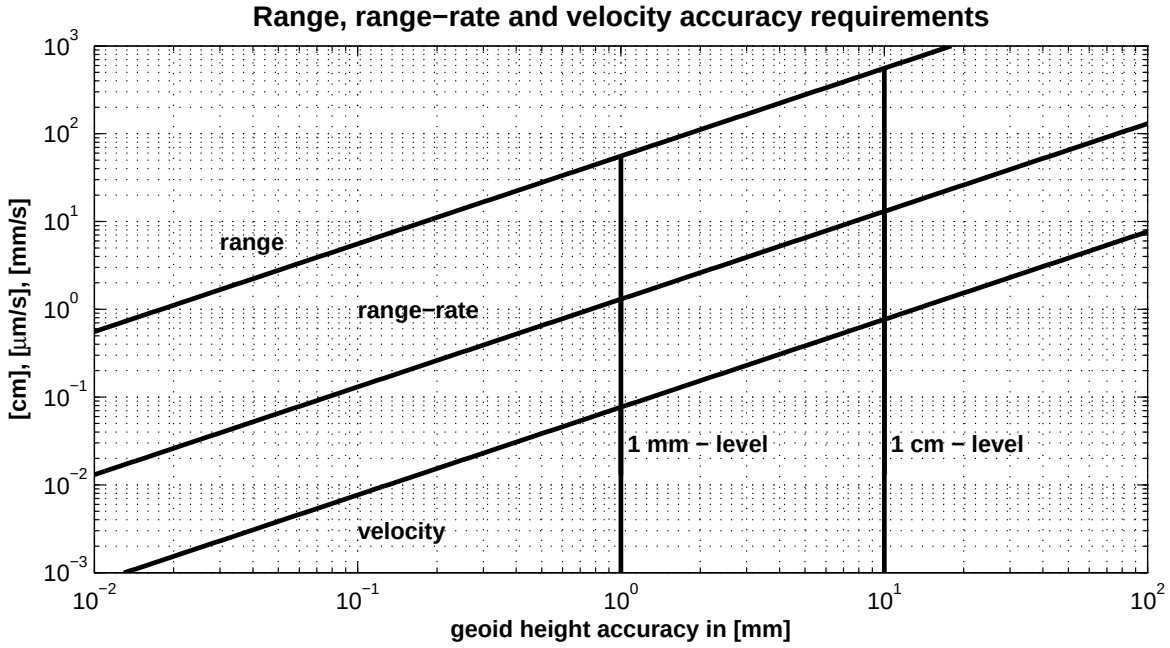

Figure 5.2: Error estimates for range-rate in $[\mu\mathrm{m/s}]$, range in $[\mathrm{mm}]$ and velocity in $[\mathrm{mm/s}]$

range-rate must be known with an accuracy of $1.3\,\mu\mathrm{m/s}$ which is achievable. The range needs to be calculated from the GPS positions since the K-band range is biased. The necessary accuracy is 55 cm, which is easily achievable. However, the limiting factor is once more the velocity determination. The energy balance approach for the case of GRACE demands an accuracy of $0.077\,\mathrm{mm/s}$ which is half an order of magnitude smaller than the achievable $0.14\,\mathrm{mm/s}$ (cf. section 3.4). This already indicates that the aspired accuracy of 1 mm in geoid height cannot be achieved with this approach. However, surprisingly, it is a less stringent condition than Jekeli (1999) proposed. He stated a value of $0.02\,\mathrm{mm/s}$.

An alternative way was suggested by Han et al. (2006). An accuracy in the geopotential differences at the level of $0.002\,\mathrm{m^2/s^2}$ is achievable by simultaneously adjusting the orbits of the GRACE satellites with the range rate measurements. As input, an a priori orbit with an uncertainty of 2 cm in position and $20\,\mathrm{mm/s}$ in velocity is sufficient.

5.2 Proof of concept: simulation study

The next step is the validation of the concept itself. For this, simulated data from the IAG special commission SC7 (Ilk, 2001) is used. Noiseless positions and velocities are provided for a period of one month with 5 seconds sampling. The two satellites are released into the same orbit with a 6 seconds time difference. The distance is in the beginning approximately 230 km and slowly decreasing to 228 km. Tidal accelerations are neglected as well as non-gravitational forces. Therefore, equation (5.1.1) simplifies and contains the kinematic energy, the normal potential and the centrifugal potential term only. A reference difference in the disturbing potential is derived from a spherical harmonic synthesis for each of the satellites using EGM96 to degree and order 300 as input.

$$T_{12}^{EGM96} = T_2\left(\lambda_2, \phi_2, r_2\right) - T_1\left(\lambda_1, \phi_1, r_1\right) \tag{5.12}$$

The kinetic energy term can be calculated in four different ways, i.e., from the velocities, from equation (5.6) inserted into equation (5.2), according to the approach of Wolff (1969), and by the approach of Jekeli (1999). For the last one, no consistent reference orbit was available and thus it is dismissed in the following. From section 5.1.1 it can still be concluded that the approach should outperform Wolff's approach and be close to the exact representation but slightly worse than it. Consequently, the following approaches are compared:

$$\begin{aligned}
\text{from velocity: :} \quad T_{12} &= \frac{1}{2}\left(|\dot{\boldsymbol{x}}_2|^2 - |\dot{\boldsymbol{x}}_1|^2\right) - U_{12} - Z_{12} \\
\text{K-band representation:} \quad T_{12} &= \frac{1}{2}\left[\dot{\rho}\left(\dot{\boldsymbol{x}}_2 + \dot{\boldsymbol{x}}_1\right)^T \boldsymbol{e}_{12} + \rho\left(\dot{\boldsymbol{x}}_2 + \dot{\boldsymbol{x}}_1\right)^T \dot{\boldsymbol{e}}_{12}\right] - U_{12} - Z_{12} \\
\text{according to Wolff:} \quad T_{12} &= \dot{\rho}\,|\dot{\tilde{\boldsymbol{x}}}| - U_{12} - Z_{12}
\end{aligned}$$

If the data is consistent with the reference potential along the orbit, the first two approaches should give results close to zero and the last one some type of approximation. Figure 5.3 shows exactly this behavior. The approach according to Wolff indeed shows an approximation at the level of $\pm 8\,\mathrm{m^2/s^2}$ as aspired in his paper. The data in the

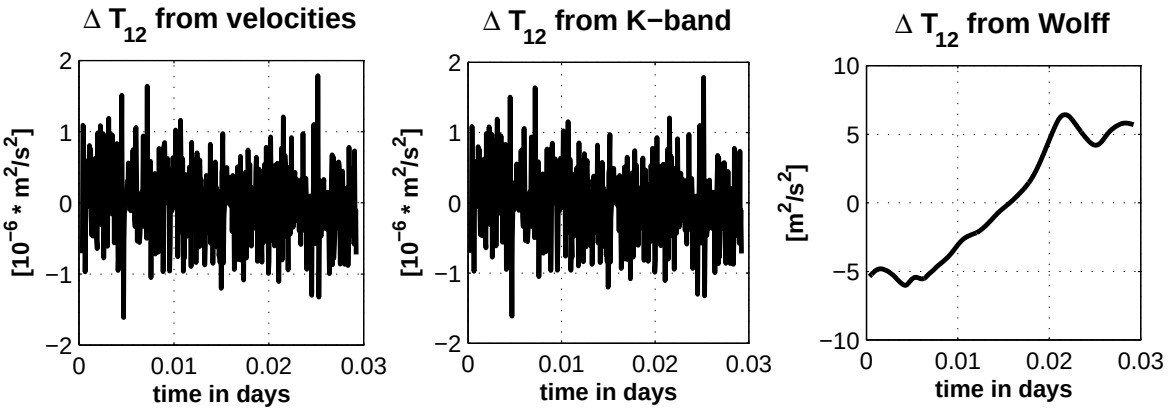

Figure 5.3: Differences between the three approaches and the reference data

left and middle panel is at the level of 10^{-6} and shows an identical pattern, i.e., the derivation using the K-band is an exact representation of the velocity term and can be reproduced using noiseless data.

5.3 Feasibility study: processing of real GRACE data

Despite the high demands of the energy integral for GRACE, the approach was implemented for August 2002 using real data. Figure 5.4 illustrates the flow of the data processing. The two satellites are first independently processed as discussed in section 4.2.1 and subsequently the components are combined and connected with the microwave measurement using equation (5.6). The position data is again provided by the IAPG, TU Munich, and is calculated in the exact same way as for CHAMP, i.e., the positions are derived kinematically and the velocities are determined by numerical differentiation according to section 3.4. Since positions and velocities were provided in a 30-second sampling, the data was subsequently interpolated to the 5-second sampling of the K-band using splines. The results are disturbing potential differences along the orbit and the spherical harmonic coefficients are solved for using a pre-conditioned conjugate gradient method (PCCGM) method.

The PCCGM method follows the procedure in Ditmar and Klees (2002). The initial

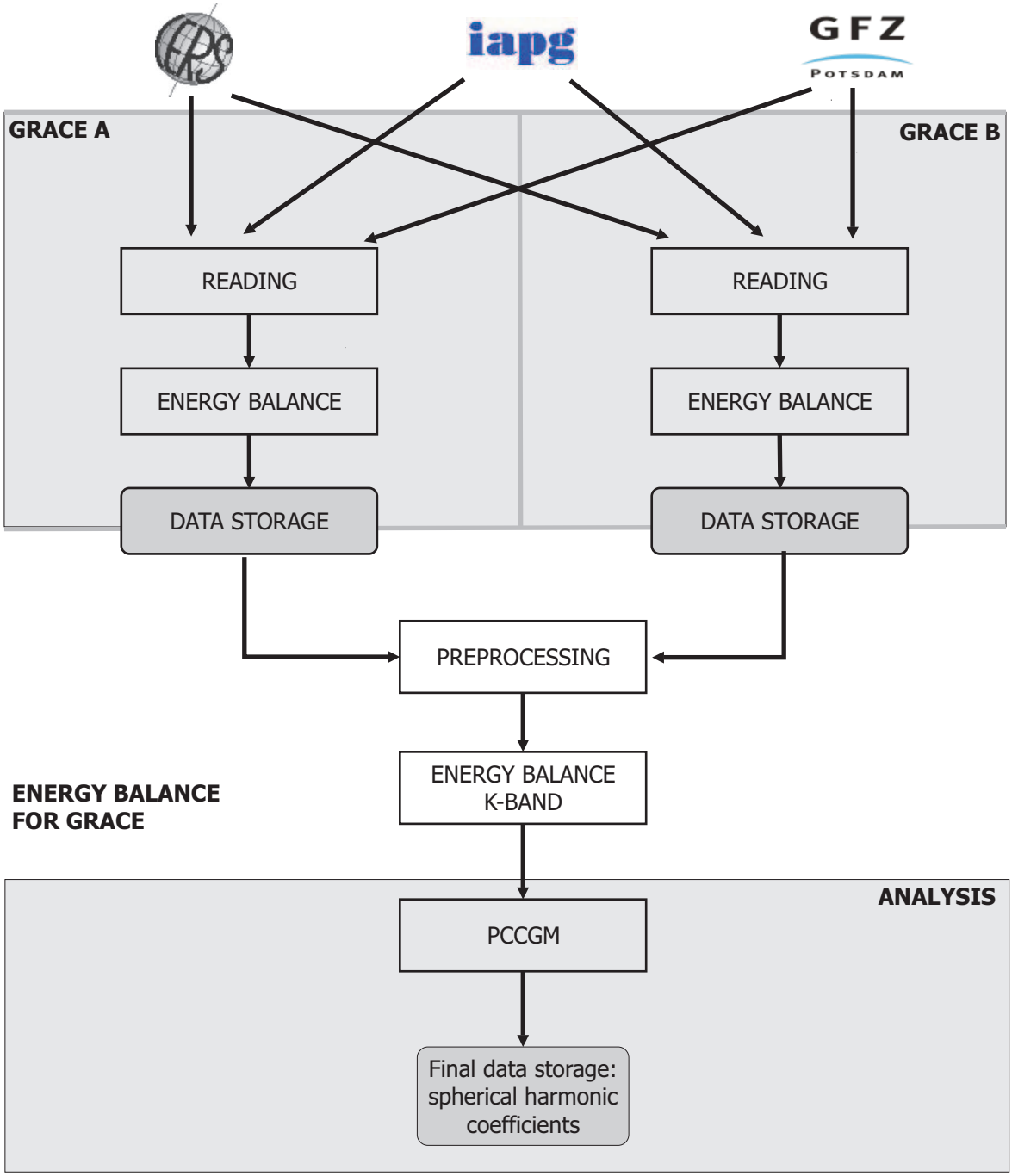

Figure 5.4: Processing structure in case of GRACE

solution is calculated as:

$$\begin{aligned} \boldsymbol{x}_0 &= \tilde{\boldsymbol{x}}_0 = \mathbf{0} \\ \boldsymbol{r}_0 &= \tilde{\boldsymbol{r}}_0 = A^T P \boldsymbol{l} \\ \boldsymbol{p}_0 &= \tilde{\boldsymbol{p}}_0 = N_{bd}^{-1} \boldsymbol{r}_0 \\ k &= 0 \end{aligned}$$

As an approximation, the block-diagonal of the normal matrix N_{bd} is used which reduces the number of iterations compared to a diagonal matrix. The method also includes the so-called Schönauer smoothing (Schönauer, 2000) which ensures a strictly monotonic convergence of the method. If not included, the RMS of the residuals may increase in some steps and decrease in others. The symbols with the tilde are related to this smoothing.

The first step of one iteration consists then of the following:

$$\boldsymbol{a}_k = A^T \left(P \left(A \boldsymbol{p}_k \right) \right) + \alpha R \boldsymbol{p}_k, \tag{5.13}$$

where α is the regularization parameter and R the corresponding regularization matrix. Currently, no regularization was applied in the calculation. Ditmar and Klees (2002) suggest to use the *first order Tikhonov* regularization instead of the *Kaula* rule since in their investigation the former yielded better results. The following steps can be implemented straightforwardly:

$$\begin{aligned} \alpha_k &= \frac{\boldsymbol{r}_k^T \boldsymbol{p}_k}{\boldsymbol{a}_k^T \boldsymbol{p}_k} \\ \boldsymbol{x}_{k+1} &= \boldsymbol{x}_k + \alpha_k \boldsymbol{p}_k \\ \boldsymbol{r}_{k+1} &= \boldsymbol{r}_k - \alpha_k \boldsymbol{a}_k \\ \boldsymbol{e}_k &= N_{bd}^{-1} \left(\tilde{\boldsymbol{r}}_k - \boldsymbol{r}_{k+1} \right) \\ \gamma_k &= -\frac{\boldsymbol{r}_{k+1}^T \boldsymbol{e}_k}{\left(\tilde{\boldsymbol{r}}_k - \boldsymbol{r}_{k+1} \right)^T \boldsymbol{e}_k} \\ \tilde{\boldsymbol{x}}_{k+1} &= \boldsymbol{x}_{k+1} + \gamma_k \left(\tilde{\boldsymbol{x}}_k - \boldsymbol{x}_{k+1} \right) \\ \tilde{\boldsymbol{r}}_{k+1} &= \boldsymbol{r}_{k+1} + \gamma_k \left(\tilde{\boldsymbol{r}}_k - \boldsymbol{r}_{k+1} \right) \end{aligned}$$

At this point, the solution is tested for its convergence. The following two criteria are used:

$$\begin{aligned} \|\tilde{\boldsymbol{r}}_{k+1}\| &< \epsilon_1 \\ \tilde{\boldsymbol{x}}_{k+1} - \tilde{\boldsymbol{x}}_k &< \epsilon_2 \end{aligned}$$

The difference $\tilde{\boldsymbol{x}}_{k+1} - \tilde{\boldsymbol{x}}_k$ is defined as the maximum of the difference of the spherical harmonic coefficients divided by the corresponding error degree variance (cf. Ditmar and Klees (2002)). The two threshold values ϵ_1 and ϵ_2 are set to 10^{-9} in the computations and if the criteria are fulfilled the solution vector $\boldsymbol{x}$ is set equal to the solution vector of the last iteration step $\tilde{\boldsymbol{x}}_{k+1}$. If the criteria are not fulfilled, the following steps are executed:

$$\begin{aligned} \tilde{\boldsymbol{p}}_{k+1} &= N_{bd}^{-1}\boldsymbol{r}_{k+1} \\ \beta_{k+1} &= \frac{\boldsymbol{r}_{k+1}^T\tilde{\boldsymbol{p}}_{k+1}}{\boldsymbol{r}_k^T\tilde{\boldsymbol{p}}_k} \\ \boldsymbol{p}_{k+1} &= \tilde{\boldsymbol{p}}_{k+1} + \beta_{k+1}\boldsymbol{p}_k \end{aligned}$$

The iteration step k is raised by one and the procedure is repeated from equation (5.13) on. The PCCGM enables the solution of large matrix systems. It uses a sparse preconditioning matrix in order to derive a solution and compensates for the error by iterations. For the case of GRACE, 29 iteration steps were necessary for the computation of the solution in August 2002, which already indicates that the solution only converges slowly due to high noise in the data.

The first validation of the results is done is in the spectral domain. Figure 5.5 shows in the top left panel the degree RMS difference spectra with respect to the GGM02s solution and, for comparison, UofC is included. The GRACE solution for August 2002 is already one order of magnitude worse than UofC. The cumulative error shows that the solution is one order of magnitude worse, in general. The gain with respect to UofC and the signal-to-noise ratio show also the degradation by one order of magnitude. Consequently, it must be concluded that this approach fails.

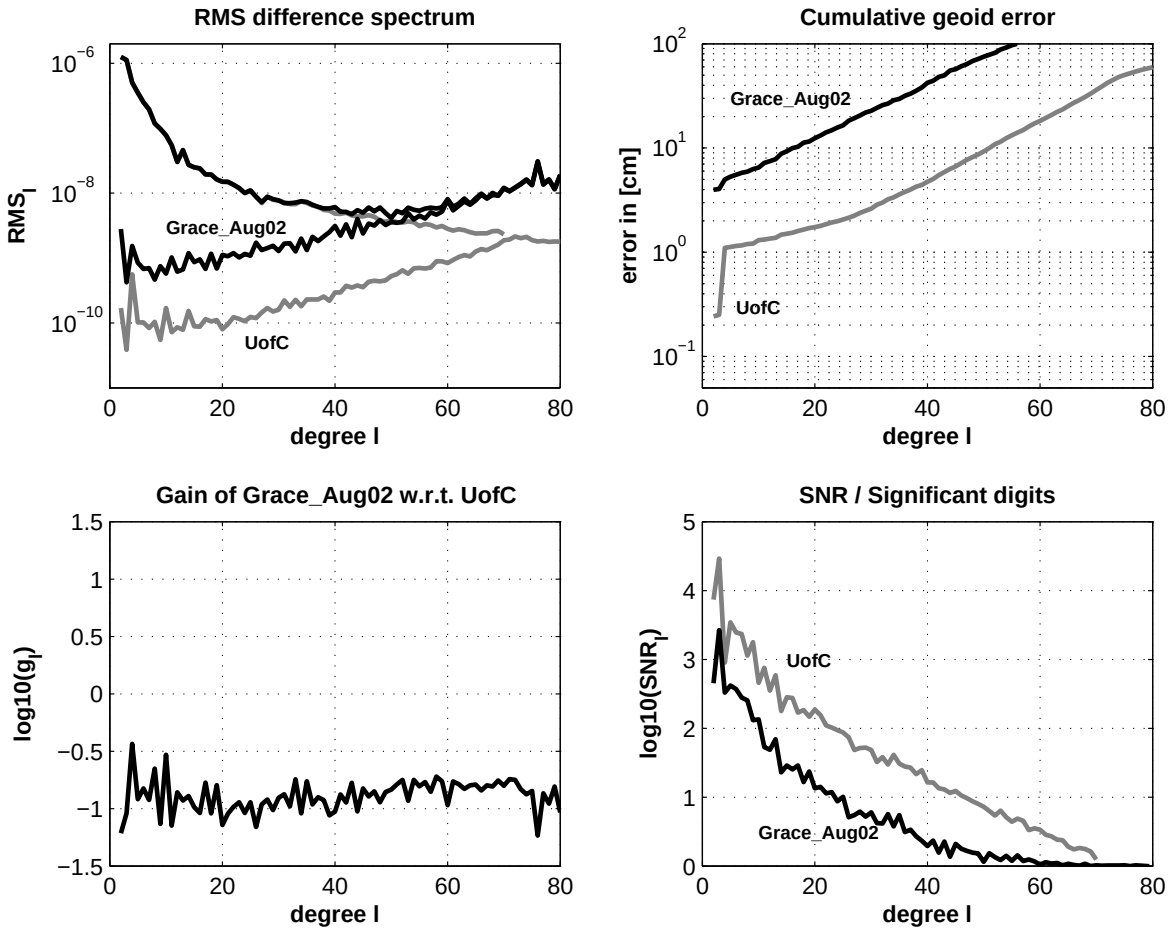

Figure 5.5: Difference spectrum w.r.t. GGM02s: degree RMS (top left), cumulative geoid error (top right), gain w.r.t. EGM96 (bottom left), significant digits (bottom right)

The comparison in the spatial domain shows distinct North-South features which coincide with the groundtracks of the satellite. The RMS along parallels also shows a bulge at the equator. The spatial data distribution can be excluded as a cause, since the groundtrack coverage is dense in August 2002. Instead, the pattern is caused by the noise in the position and velocity data along the orbit, which results in the degradation of the spherical harmonic coefficients.

Overall, it can be concluded that the results are far below the expected performance of GRACE and the velocity determination needs to be held liable as the primary error source. Figure 5.7 shows the comparison of the difference disturbing potential along

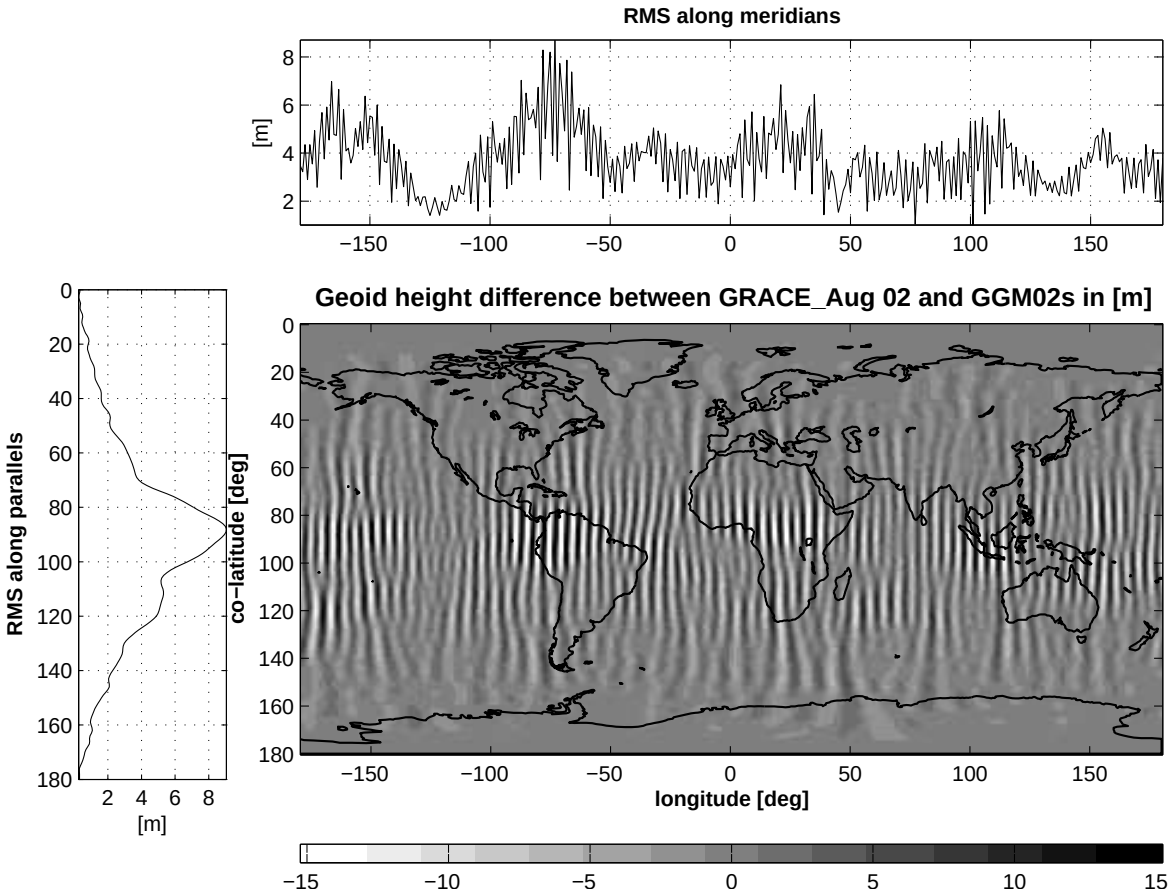

Figure 5.6: Difference between the GRACE August 2002 solution and GGM02s in terms of geoid height: spatial (center), RMS along the meridians (top), RMS along parallels (left). The unit is m and $L^{max} = 80$.

the orbit. The top figure shows the comparison between EGM96 and GGM02s. The difference at satellite height has a maximum of $0.5\,\mathrm{m^2/s^2}$, which corresponds to a difference in geoid height of 5 cm. This serves as a reference. The derived signal should be better than this since it will represent a subset of GGM02s; it is shown in the middle panel. Obviously, oscillations exist which are by a factor of 10 higher than the difference of EGM96 to GGM02s. The bottom panel is derived from simulated data by adding white noise with a magnitude of $0.1\,\mathrm{mm/s}$ to the velocity component of each satellite. It shows similar oscillations with the same magnitude and confirms that the velocity determination cannot match the demanded accuracy. At this point, it must be concluded that

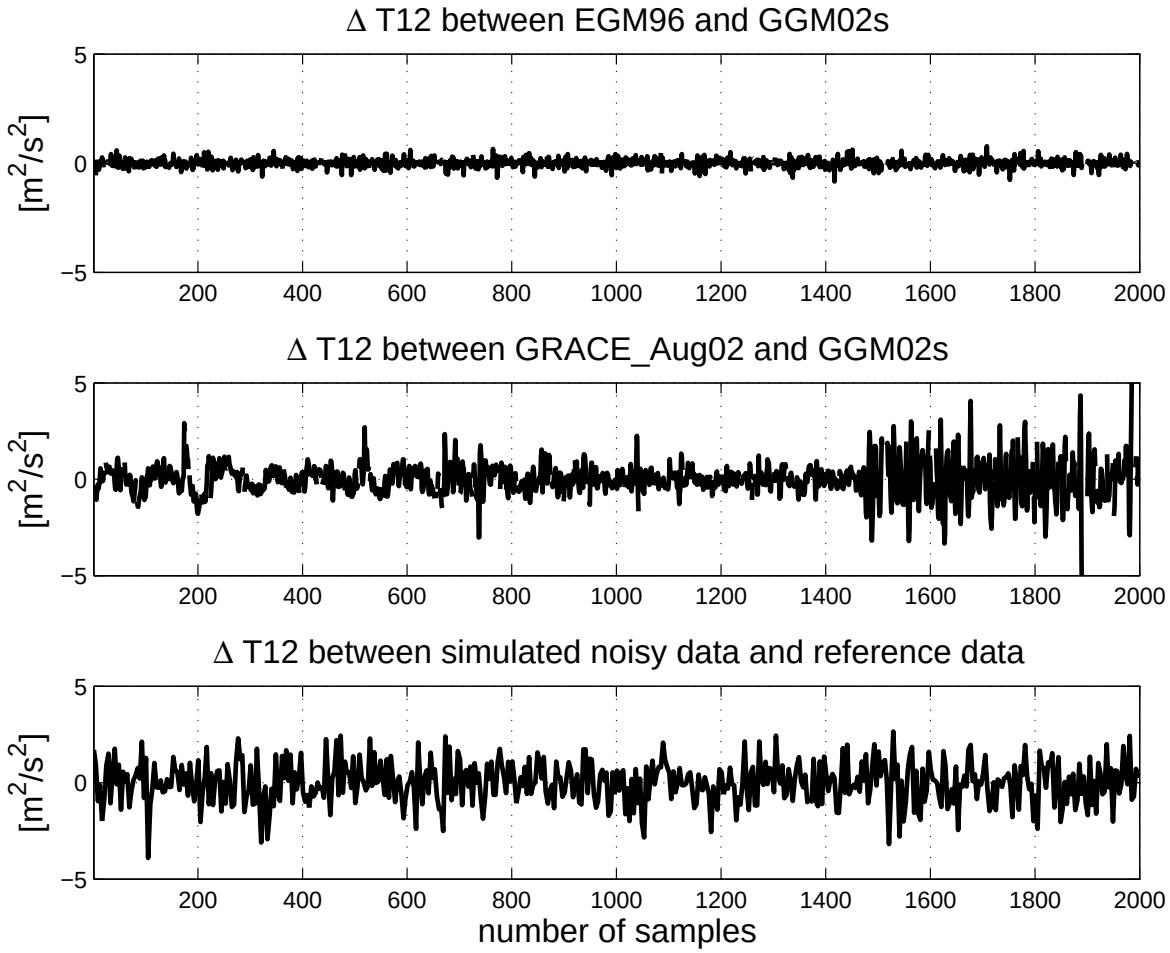

Figure 5.7: Difference of T_{12} with respect to GGM02s: from EGM96 (top), from real data (middle), from simulated data with noise added (bottom)

the approach fails. It should be investigated whether the subtraction of a reference orbit as introduced in Jekeli (1999) reduces the accuracy demands. Additionally, the aforementioned approach by Han et al. (2006) should be considered.

5.4 Summary

The energy balance approach is extended for a second satellite and the microwave inter-satellite measurements are included in the kinetic energy term which yields disturbing potential differences along the orbit. The concept is validated with noiseless simulated

data and shows that equation (5.6) is an exact representation of the relative kinetic energy in terms of the K-band. However, GPS-derived velocities are necessary for the determination of this term. The error analysis shows that the velocity needs to be determined with an accuracy of $0.07\,{}^{\mathrm{mm}}/_{\mathrm{s}}$ or better in order to be applied successfully. Tests with real GRACE data support the conclusion that the approach cannot be used with the current achievable accuracy. The situation might be improved by the subtraction of a reference orbit and should be investigated in future work.

Chapter 6

Local Gravity Field Recovery

The derivation of global gravity field solutions from CHAMP and GRACE led to a vast extension of the knowledge about the gravity field. However, CHAMP as well as GRACE only partially fulfill their anticipated objectives till now. CHAMP misses approximately one order of magnitude in accuracy. As one of the reasons, the data distribution is mentioned which is especially obvious during months with sparse groundtrack coverage (cf. section 4.2.4).

On the other hand, the energy integral yields in-situ measurements but it is analyzed by a global spherical harmonic analysis. Local variations are derived from the global models and subsequently interpreted. Certainly, this is not optimal, especially since global reference models for, e.g., tides are applied. An improvement for local areas is therefore expected if a proper interpolation and/or downward continuation technique is found. This chapter investigates two different methods which can be applied for interpolation at orbit height and/or downward continuation. The input data for this case study is kept consistent, i.e., no localized models for, e.g., tides are applied. This is left for future work. The primary objective is to find a proper method for the derivation of local solutions.

6.1 The framework of local gravity field determination

6.1.1 Motivation

Gravity field recovery depends on the spatial resolution of the data. The dependency of a global solution is mainly related to the separation of orbit arcs at the equator. In the case of CHAMP, the orbit arcs are separated by up to 5° in months with sparse groundtrack coverage. Figure 6.1 illustrates this effect for a time period of good ground

coverage on the left (January 2004) and for a sparse ground coverage on the right (June 2003). The top part of the figure shows the Arctic region with its converging groundtracks. The bottom part shows a 100 °-section around the Greenwich meridian at the equator. Note that the number of measurements is similar in both months, but in June 2003 the arcs are clustered due to the near-repeat mode (see also section 4.2.5). Due to the almost polar orbit of CHAMP the tracks are converging towards the

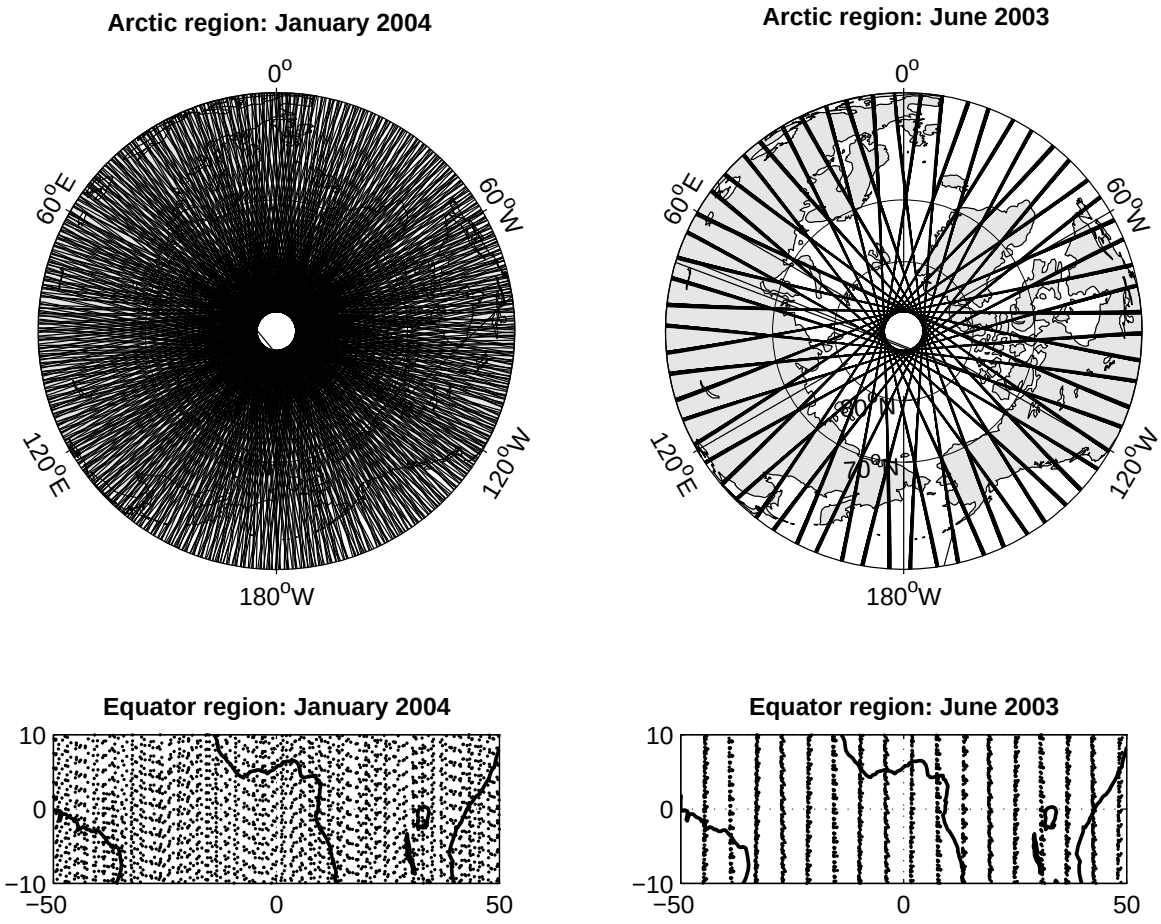

Figure 6.1: Monthly groundtrack pattern for January 2004 (left) and June 2003(right): arctic (top) and equator section (bottom)

pole. It clearly shows that in high-latitude areas more information is available than in equatorial areas. Figure 6.2 confirms the situation. It shows the number of points available in an area of 100 km × 100 km for different latitude bands. The number of

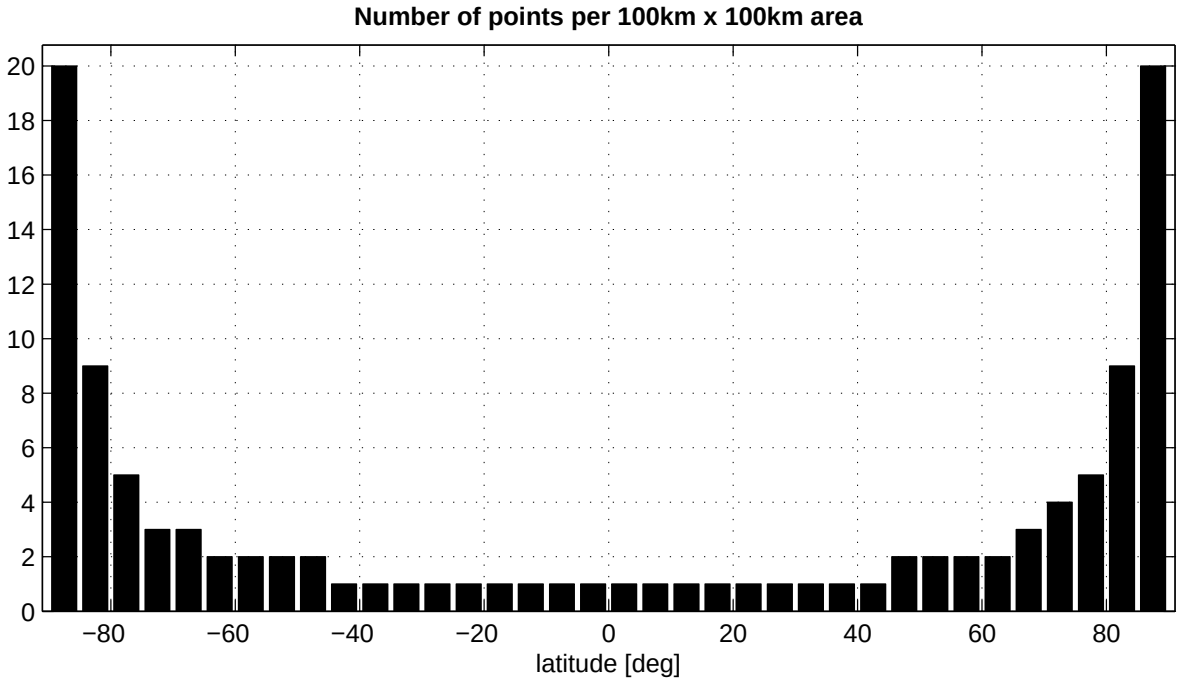

Figure 6.2: Number of points per latitude band

points is constantly increasing starting from $|\varphi| = 50\,^\circ$ towards the pole. In near-polar areas, the data density is 20 times higher than at the equator. Therefore, it is beneficial to recover regional solutions of the gravity field for areas at high latitudes. The possible improvement was already shown by Jekeli and Garcia (2000) using simulated data.

6.1.2 Interpolation techniques

The interpolation or prediction $\hat{x}$ at an arbitrary point P can be represented by a linear combination of the stochastic measurements $\tilde{l}$:

$$\hat{x}_P = \sum_{i=1}^{I} \alpha_i \tilde{l}_i, \tag{6.1}$$

where α_i are the interpolation coefficients. Many different interpolations schemes were investigated in the past. They include triangulation, tessellation and Overhauser splines. Here, the techniques are restricted to the *weighted mean prediction* and the *least-squares prediction/collocation*. The former is a computationally fast procedure and

is often used to create quickly gridded data before the application of FFT-techniques. The least-squares collocation is a computationally intensive method but is optimal in the sense that it minimizes the interpolation error.

Weighted mean prediction Replacing α_i in equation (6.1) with one over the number of measurements I yields the mean of the solution. However, since near masses have a higher influence than far masses on the gravity in one point, the interpolation coefficients should be weighted accordingly. The simplest way to achieve this is by using a weighted mean. The weight depends on the inverse distance of the data point to the calculation point.

$$\alpha_i = \frac{1/r_i^n}{\sum_{i=1}^{I} 1/r_i^n} \tag{6.2}$$

By controlling the power n of the distance r different local behavior can be achieved. The higher the power, the higher the influence of local data. For the interpolation of the disturbing potential, the power can be kept low since the gravity field is smooth.

Least-squares prediction/collocation An interpolation can be considered optimal if the interpolation error is minimized. The interpolation error is given as the difference between a predicted value $\hat{x}_P$ and the true value x_P at the same point:

$$\epsilon = x_P - \hat{x}_P = x_P - \sum_{i=1}^{I} \alpha_i \tilde{l}_i \tag{6.3}$$

Minimizing the maximum error in all interpolation points leads to a Tschebyscheff interpolation. Applying the least-squares principle yields the least-squares prediction (Heiskanen and Moritz, 1967). The theory is discussed comprehensively in Moritz (1980a) and will only be reviewed here with the focus on the application. The optimal interpolation coefficients are given as

$$\alpha_i = \sum_{j=1}^{I} C_{PQ_i} \left(C_{Q_iQ_j} + D_{Q_iQ_j} \right)^{-1}, \tag{6.4}$$

where C is a signal covariance matrix and D a noise covariance matrix. The covariance is the expectation of the product of two gravity quantities at a certain distance.

The matrix $C_{Q_iQ_j}$ describes the correlation of the error-free measurements, the matrix C_{PQ_i} the correlation between the input quantity and the output quantity. Noise is taken into account by $D_{Q_iQ_j}$. Its application is also the reason why least-squares predicition/collocation is considered as consisting of a filtering plus a prediction step.

The usage of the eigenvalues λ_l (see below) of gravity functionals enables the transformation between two gravity quantities of different kind. The covariance can either be determined from a global covariance model or be derived from the measurements itself. It is normally developed into a series of Legendre polynomials:

$$C^{AB}\left(\psi_{SQ}\right) = \sum_{l=2}^{N} c_l^{AB} P_l^{\mathrm{Leg}}\left(\cos\psi_{SQ}\right), \tag{6.5}$$

where S is the calculation point, Q the data point, ψ the spherical distance between S and Q and P_l^{Leg} is the Legendre polynomial of degree l. The degree variance of the two quantities A and B is denoted by c_l^{AB}. The non-specific (i.e., dimensionless) degree variances c_l can be determined from

$$c_l = \sum_{m=0}^{N} \left(\Delta\bar{C}_{lm}^2 + \Delta\bar{S}_{lm}^2\right). \tag{6.6}$$

Specific degree variances can be derived by applying the law of covariance propagation:

$$c_l^{AB} = \beta_n^A\, \beta_l^B\, c_l \tag{6.7}$$

$$c_l^{AA} = \beta_l^A\, \beta_l^A\, c_l \tag{6.8}$$

Given a specific degree variance of B the transition to another specific degree variance of A can be achieved by:

$$c_l^{AA} = \frac{\beta_l^A\, \beta_l^A}{\beta_l^B\, \beta_l^B}\, c_l^{BB} \tag{6.9}$$

The degree variances are not treated as dimensionless quantities which means they consist of a dimensioning factor D, an upward continuation term $\frac{R}{r}$ of specific power, the eigenvalue λ_l and the dimensionless degree variances c_l. The following table 6.1 lists these factors and the specific transfer coefficients β_l. If the upward continuation term is neglected and the input and output quantities are of the same kind, equation

	D	$\left(\frac{R}{r}\right)$	λ_l	β_l
T	$\frac{GM}{R}$	l+1	1	$\frac{GM}{R}\left(\frac{R}{r}\right)^{l+1}$
N	R	l+1	1	$R\left(\frac{R}{r}\right)^{l+1}$
Δg	γ	l+2	$(l-1)$	$\frac{GM}{R^2}\left(\frac{R}{r}\right)^{l+2}(l-1)$
δg	γ	l+2	$-(l+1)$	$-\frac{GM}{R^2}\left(\frac{R}{r}\right)^{l+2}(l+1)$
T_{rr}	$\frac{2GM}{R^3}$	l+3	$(l+1)(l+2)$	$\frac{2GM}{R^3}\left(\frac{R}{r}\right)^{l+3}(l+1)(l+2)$

Table 6.1: Transfer coefficients for covariance propagation

(6.4) is generally referred to as *least-squares prediction*. Otherwise, the method is called *least-squares collocation*.

For the degree variances, several models exist. A famous example is Kaula's rule of thumb:

$$c_l = \frac{1.6 \cdot 10^{-10}}{l^3}, \tag{6.10}$$

which is a unitless signal model. Other degree variance models are mostly specific. Among them is the model of Tscherning & Rapp (Tscherning and Rapp, 1974), which is given as:

$$\begin{aligned} c_2^{\Delta g \Delta g} &= 7.6\,\mathrm{mGal}^2 && \text{for } l = 2 \\ c_l^{\Delta g \Delta g} &= \left(\frac{GM}{R^2}\right)^2 \left(\frac{R^2}{r_P r_Q}\right)^{l+2} s^{l+2} \frac{A(l-1)}{(l-2)(l+B)} && \text{for } l \geqslant 3, \end{aligned} \tag{6.11}$$

with $s = \left({}^{R_B}/_{R}\right)^2 = 0.999617$, $A = 425.28\,\mathrm{mGal}^2$ and $B = 24$. According to equation (6.9) the relation between the degree variances of the potential and of the gravity anomalies is given as

$$c_l^{TT} = \frac{r_P r_Q}{(l-1)^2}\, c_l^{\Delta g \Delta g} \tag{6.12}$$

In order to derive the covariance function for the disturbing potential, equation (6.12)

needs to be inserted in equation (6.11):

$$\begin{aligned} c_2^{TT} &= 7.6\,\mathrm{mGal}^2 \cdot r_P\, r_Q && \text{for } l = 2 \\ c_l^{TT} &= \left(\frac{GM}{R}\right)^2 \left(\frac{R^2}{r_P r_Q}\right)^{l+1} s^{l+2} \frac{A}{(l-1)(l-2)(l+B)} && \text{for } l \geqslant 3 \end{aligned} \tag{6.13}$$

Equation (6.13) together with equation (6.4) provide the optimal interpolation coefficients for the application to CHAMP data. The coefficients are only optimal for a global application due to the usage of a global covariance function. For the localized calculations in high-latitude areas they might be suboptimal and the derivation of local covariance functions from the data should be investigated. Nevertheless, since the calculations are performed for the long to medium wavelength part and due to the smoothing property of the upward continuation term the difference is most likely small.

Only a limited amount of data points can be used in the processing due to memory constraints. The nearest 350 points are selected for the tests. For comparison: in January 2004, 82882 data points were used to estimate 5041 unknown spherical harmonic coefficients.

6.2 Interpolation at satellite height

Before the data is continued downward, the interpolation at orbit height is considered. Downward continuation will result in an amplification of errors. Approximately one order of magnitude is lost during the process. The interpolation at orbit height is also useful for applications that depend on gridded data like, e.g., the spherical harmonic analysis using FFT techniques or for the torus approach (Sneeuw, 2003). The search for time-variable effects can also be done at satellite height, although the signal is smoothed due to the upward continuation term.

Before the interpolation the data is continued to a mean orbit height $\bar{r}$ using a Taylor expansion up to the third order:

$$T(\bar{r}) = T(r) + \frac{\partial T}{\partial r}(\bar{r} - r) + \frac{1}{2}\frac{\partial^2 T}{\partial r^2}(\bar{r} - r)^2 + \frac{1}{6}\frac{\partial^3 T}{\partial r^3}(\bar{r} - r)^3 \tag{6.14}$$

The 3rd-order development ensures mm-level accuracy but one has to be aware that with the partial derivatives a priori information from a known gravity field is introduced. Least-squares collocation is capable of handling data at different heights but in this case study the continuation to a mean radius is also applied in order to have the same type of input for both interpolation methods.

The subsequent comparisons in the spatial domain (figures 6.3 to 6.13) are all set up in the same way. The top left panel shows the signal itself. The top right one shows the comparison to the monthly global CHAMP-only solution. On the bottom half is the comparison to GGM02s; on the left the difference between the interpolated results and GRACE, and on the right the comparison between the monthly global solution and GGM02s. The interpolation method is considered superior if the results are better than the global monthly CHAMP-only solution.

6.2.1 Weighted mean prediction

The first interpolation technique is the linear weighted mean approach, i.e., the order n in equation (6.2) is set equal to 1. The tests are performed for January 2004 and June 2003. For each calculation point, the 20 nearest data points are used. The maximum distance to the calculation point is $5\,^{\circ}$. The weighted mean method depends on the distance of the measurement to the interpolation point. The method is quick but suboptimal, since it can be calculated quickly but the interpolation error is high. The expectation is, that the worse the data distribution and the longer the distances, the worse the results will be.

In January 2004 the groundtrack coverage was good and the data distribution was homogeneous. The top left panel of figure 6.3 shows the interpolated values for Canada. The general shape has the expected features with its minimum over the Hudson Bay, the increase East of it towards Greenland and the slight increase due to the Rocky Mountains. The top right and bottom left panel show the comparisons to global models. Both pictures show similar patterns. The error in the interpolation method exceeds the error caused by the global spherical harmonic analysis.

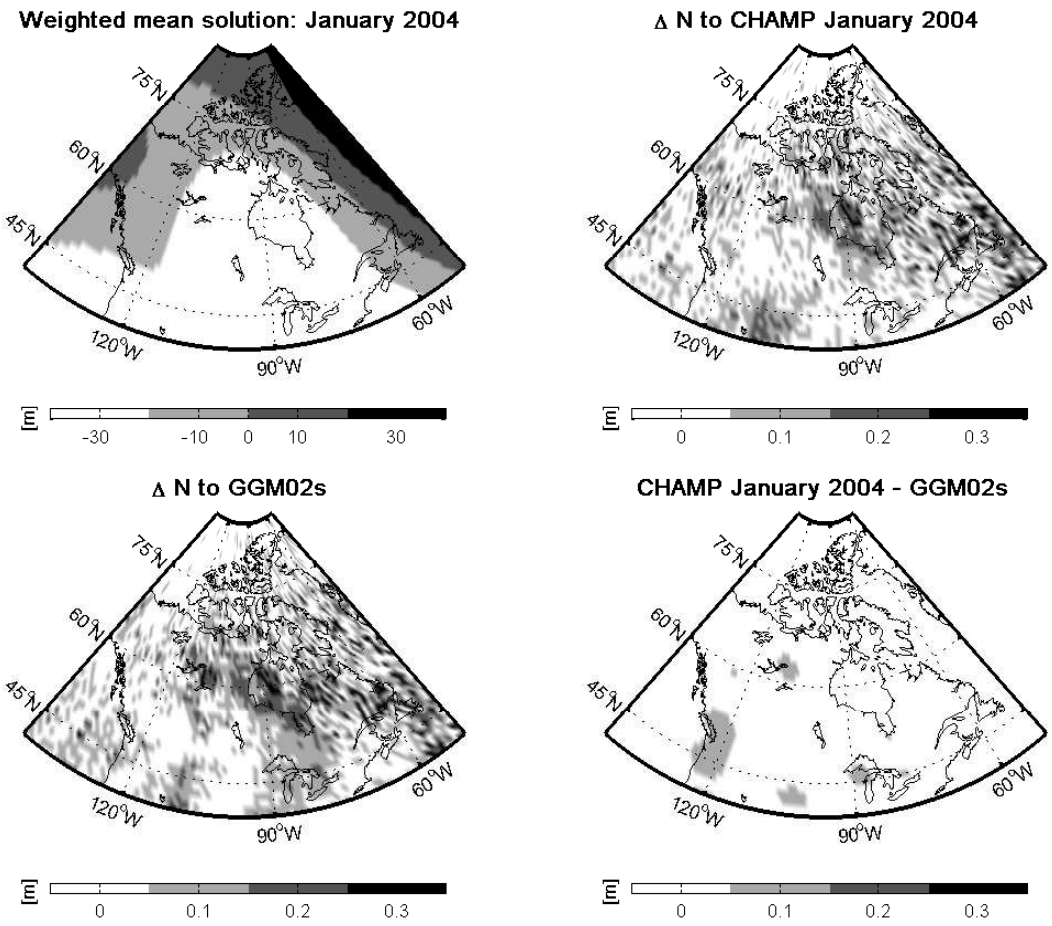

Figure 6.3: The weighted mean solution for January 2004 (top left), the comparison to the global CHAMP solution of January 2004 (top right), to GGM02s (bottom left) and the difference between the global monthly CHAMP solution and GGM02s

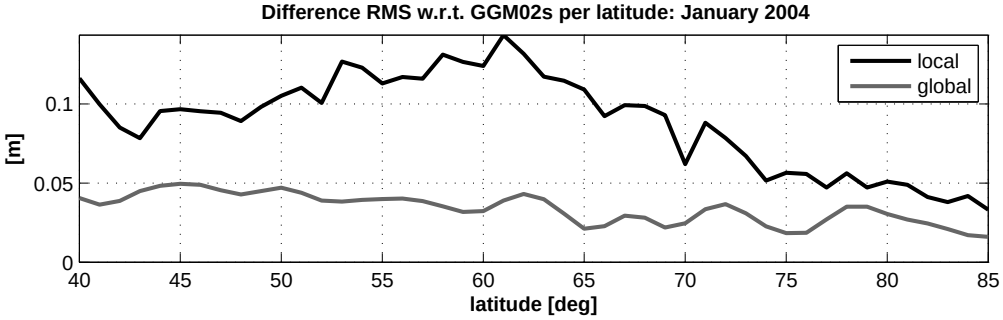

Figure 6.4: Difference RMS per latitude w.r.t. GGM02s at satellite height using weighted mean interpolation: January 2004.

The maximum error appears where the signal is maximum, i.e., in the Hudson Bay and is close to 30 cm.

Figure 6.4 shows the geoid height difference RMS per latitude w.r.t. GGM02s of the interpolated (local) solution and, for comparison, of the spherical harmonic analysis (global). The effect of the denser data distribution near the pole is clearly visible in the local solutions. The RMS drops from 10 cm at $\varphi = 65\,^\circ$ to 5 cm at the pole. The global solution has a small tilt with increasing latitude but is tolerably constant. Note that the constant value only indicates that the monthly CHAMP solution and the GRACE solution are affected equally by their specific data distribution. This does not necessarily mean that both take full advantage of the information at high latitudes.

The RMS of the difference w.r.t. GGM02s for the whole area in table 6.2 shows that the weighted mean solution is in general 2–3 times worse than the global solution. In January 2004, the difference is about 8 cm–9 cm whereas the difference of the global monthly CHAMP solution is as low as 3.5 cm. In June 2003, the RMS value is more than 20 cm and consequently about 2 times bigger than the difference between the global solutions.

	January 2004	June 2003
weighted mean - CHAMP	8.6 cm	22.8 cm
weighted mean - GGM02s	9.4 cm	20.9 cm
CHAMP - GGM02s	3.5 cm	9.0 cm

Table 6.2: RMS of the difference between the weighted mean solutions and the global solutions for Canada

The interpolation results for June 2003 are strongly affected by the data distribution. The error exceeds the limit of the colorbar in figure 6.5, i.e., it is higher than 30 cm. The shape of the error follows the distribution of the orbit arcs. Near an arc the interpolation error is small since the distance to the data points is small. However, the gaps between the arcs can reach 5 ° and there the interpolation error is maximum.

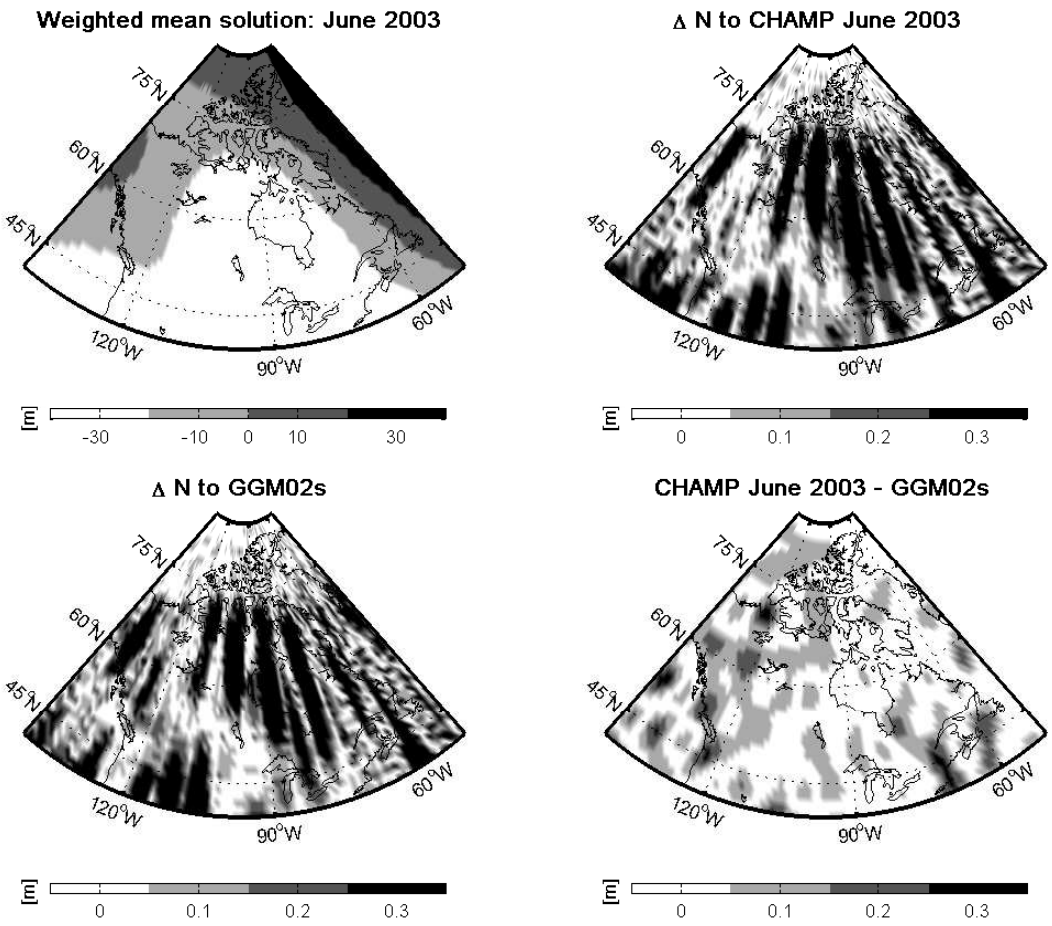

Figure 6.5: The weighted mean solution for June 2003 (top left), the comparison to the global CHAMP solution of June 2003 (top right), to GGM02s (bottom left) and the comparison between the global monthly CHAMP solution and GGM02s as a reference.

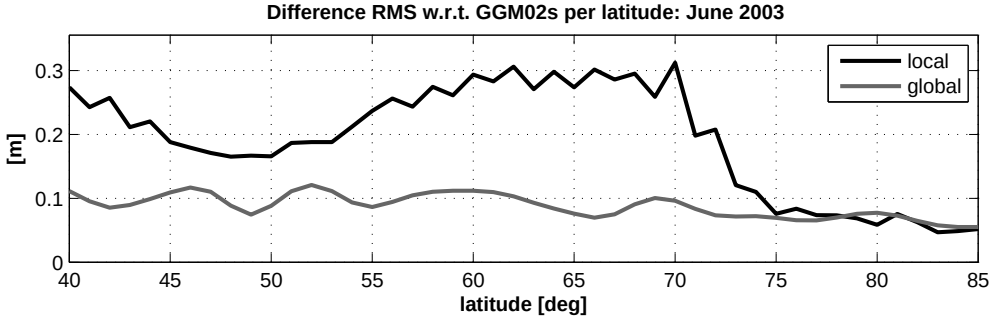

Figure 6.6: Difference RMS per latitude w.r.t. GGM02s at satellite height using weighted mean interpolation: June 2003.

Compared to January 2004, the error level in the geoid height difference RMS (figure 6.6) is doubled for the global solution and tripled for the local solution up to a latitude of $\varphi = 75\,^\circ$. Beyond this latitude, the local solution is comparable to the global monthly CHAMP solution with an RMS-value of 8 cm, i.e., the denser data distribution can only be used effectively beyond $\varphi = 75\,^\circ$.

Any interpolator is generally a smoothing operator, which is a useful property since it might smooth the errors in the measurements. Nevertheless, here it also resulted in filtering of the signal. From section 4.2.3 it is already known that the monthly global solution is degraded for June 2003. The weighted mean solution provides in the best case results on the same level as the global solution and fails to make use of the denser information in high-latitude areas as desired. It might still be useful for quick verifications or data screening. A solution for an area in Canada with 80000 data points is reached within 72 s. Using a least-squares prediction, the calculation of a solution needs 11 min. Both times are measured on a conventional desktop system. In this sense, the method is really "quick and dirty".

6.2.2 Least-squares prediction

The second method is the least-squares prediction which minimizes the interpolation error and is therefore expected to perform better. Besides, it can also be argued that due the usage of the covariance function more information about the behavior of the gravity field is introduced. It will allow the interpolation in areas with data gaps. For the signal covariance, the Tscherning & Rapp model is used up to degree and order 80. The noise covariance is also included, cf. Moritz (1980a). For the model of the noise the global covariance model of Tscherning & Rapp is developed from degree 80 to 720.

The results for January 2004 are shown in figure 6.7. The least-squares prediction improved the solution and the pattern seemed more random than in the case of the weighted mean solution. The difference to GGM02s shows features with amplitudes between 5 cm and 20 cm.

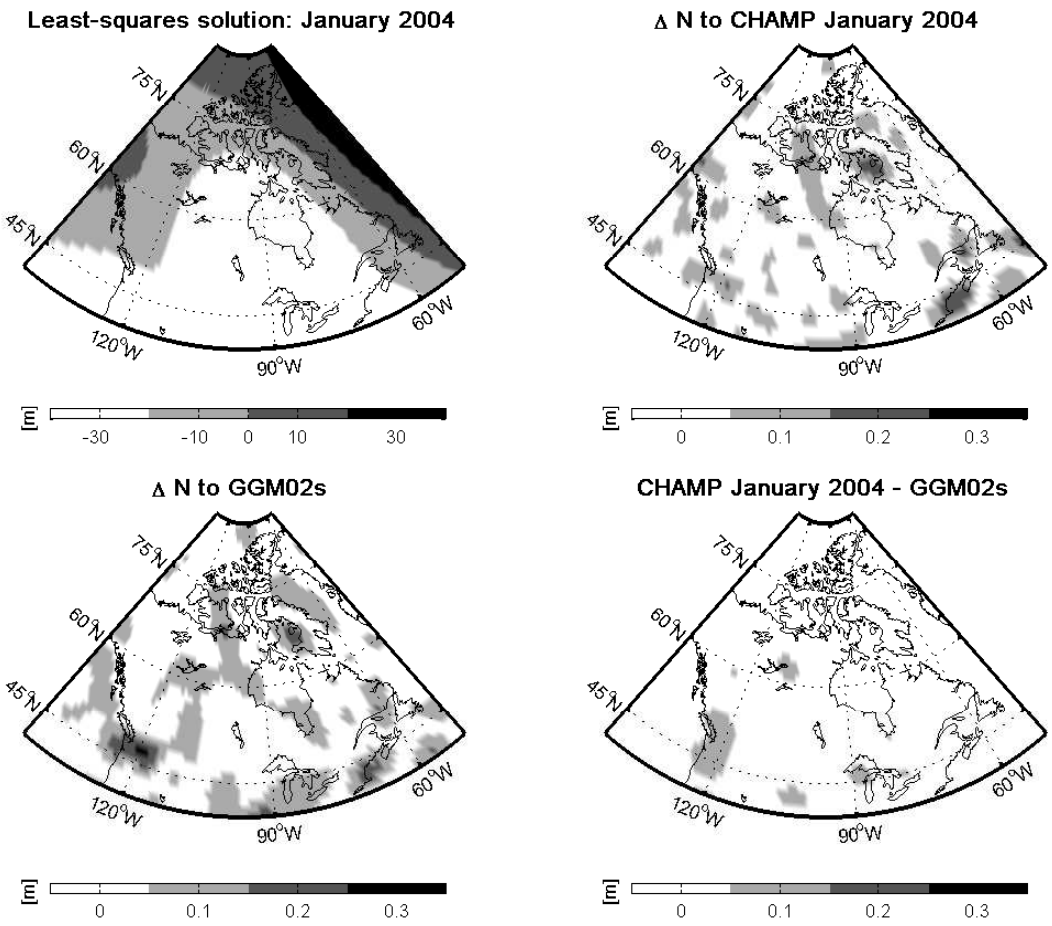

Figure 6.7: The least-squares prediction solution for January 2004 (top left), the comparison to the global CHAMP solution of January 2004 (top right), to GGM02s (bottom left) and the comparison between the global monthly CHAMP solution and GGM02s as a reference.

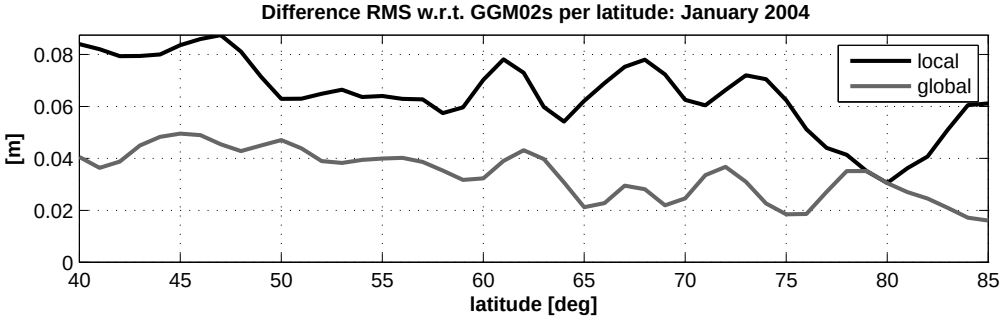

Figure 6.8: Difference RMS per latitude w.r.t. GGM02s at satellite height using least-squares prediction: January 2004.

The comparison of the global monthly solution to GGM02s has only a few pattern with differences higher than 5 cm. The RMS-values in table 6.3 show that the global solution is still better by 3.1 cm. However, the interpolated solutions is about 3 cm better than the weighted mean solution. Moreover, it is derived using a global covariance model and it might improve by using a covariance model specific to this area.

	January 2004	June 2003
LS prediction - CHAMP	5.9 cm	10.1 cm
LS prediction - GGM02s	6.6 cm	7.8 cm
CHAMP - GGM02s	3.5 cm	9.0 cm

Table 6.3: RMS of the difference between the least-squares prediction solutions and the global solutions for Canada

The geoid height difference RMS w.r.t. GGM02s in figure 6.8 shows the same picture. The least-squares solution is up to $\varphi = 75\,^\circ$ two times worse than the global monthly solution. Only for latitudes $75\,^\circ$–$80\,^\circ$ the interpolated solutions gets close to the global solution. Likely, a similar effect as in the case of the weighted mean solution is responsible for this drop. Beyond $\varphi = 80\,^\circ$, the least-squares prediction becomes sensitive to the data distribution causing an increase in the RMS. In this area, more and more data points are selected south of the calculation point due to the polar gap and the predicted value becomes biased towards these points.

In contrast to the weighted mean method, the least-squares prediction is able to handle the sparse data distribution of June 2003. The least-squares prediction solution has a smoother appearance, though there are still some artifacts left. In the south-eastern coast of Canada, northwest of the Hudson Bay and near the border to Alaska, the solution has errors larger than 25 cm. These might be related to the data distribution in these particular areas. The covariance matrix of the measurements is inverted in the processing and the geometry of the data points governs the stability of the matrix.

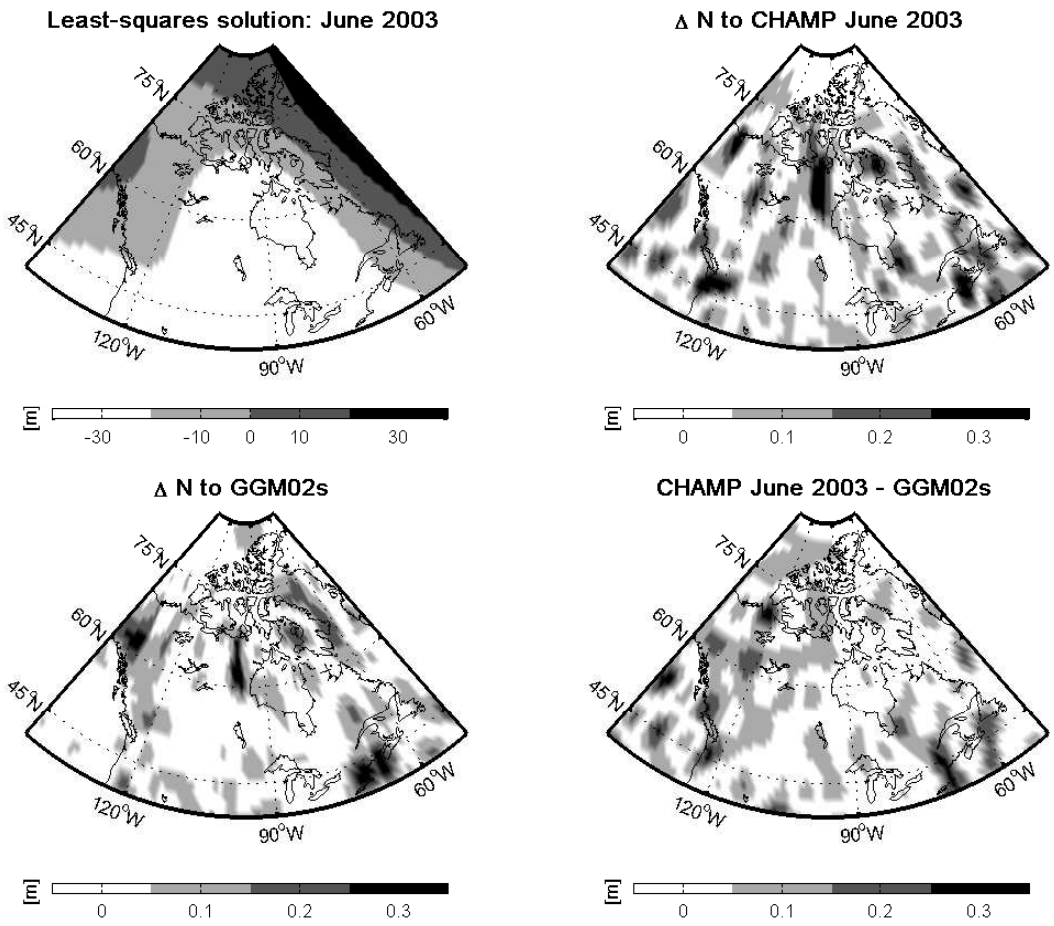

Figure 6.9: The least-squares prediction solution for June 2003 (top left), the comparison to the global CHAMP solution of June 2003 (top right), to GGM02s (bottom left) and the comparison between the global monthly CHAMP solution and GGM02s as a reference.

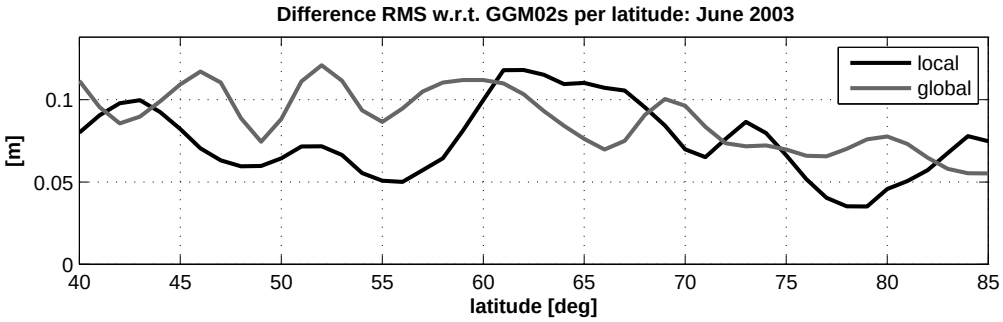

Figure 6.10: Difference RMS per latitude w.r.t. GGM02s at satellite height using least-squares prediction: June 2003.

An uneven distribution or close measurements with large discrepancies will increase the instability of the system.

Nevertheless, considering the overall RMS-value, the interpolation method is outperforming for the first time the global monthly solution in the comparison against GGM02s. The RMS-value is 1.2 cm smaller. The same holds true for most latitude bands. With the exception of the areas mentioned earlier and their corresponding latitudes, the RMS-value of the local solution is up to 4 cm smaller. This already proves that localized solutions can be beneficial. It also shows that global models do not incorporate the full information available in high-latitude areas.

6.3 Downward continuation method

6.3.1 Least-squares collocation: interpolation + downward continuation

The real advantage of the least-squares collocation, i.e., of the least-squares prediction with downward continuation in this case, will be visible in this section. Unlike the spherical harmonic analysis, the downward continuation in collocation yields a smooth solution.

> Thus collocation ensures, in fact, a smooth regular downward continuation of Δg (provided we have only a finite number of Δg_i). As the point P can be an arbitrary point on the sphere $r = R$ (Fig.13.1), the collocation solution automatically combines downward continuation and interpolation in a natural way, so as to obtain a smooth solution. (Moritz, 1980a, §13, p.97)

Although the quote above describes the case of gravity anomalies, it can be easily transferred to the case of the disturbing potential using the law of covariance propagation (6.9). In general, the downward continuation effect is inherent but since collocation is a smoothing operator the effect is expected to be less pronounced than in the case of the global solution.

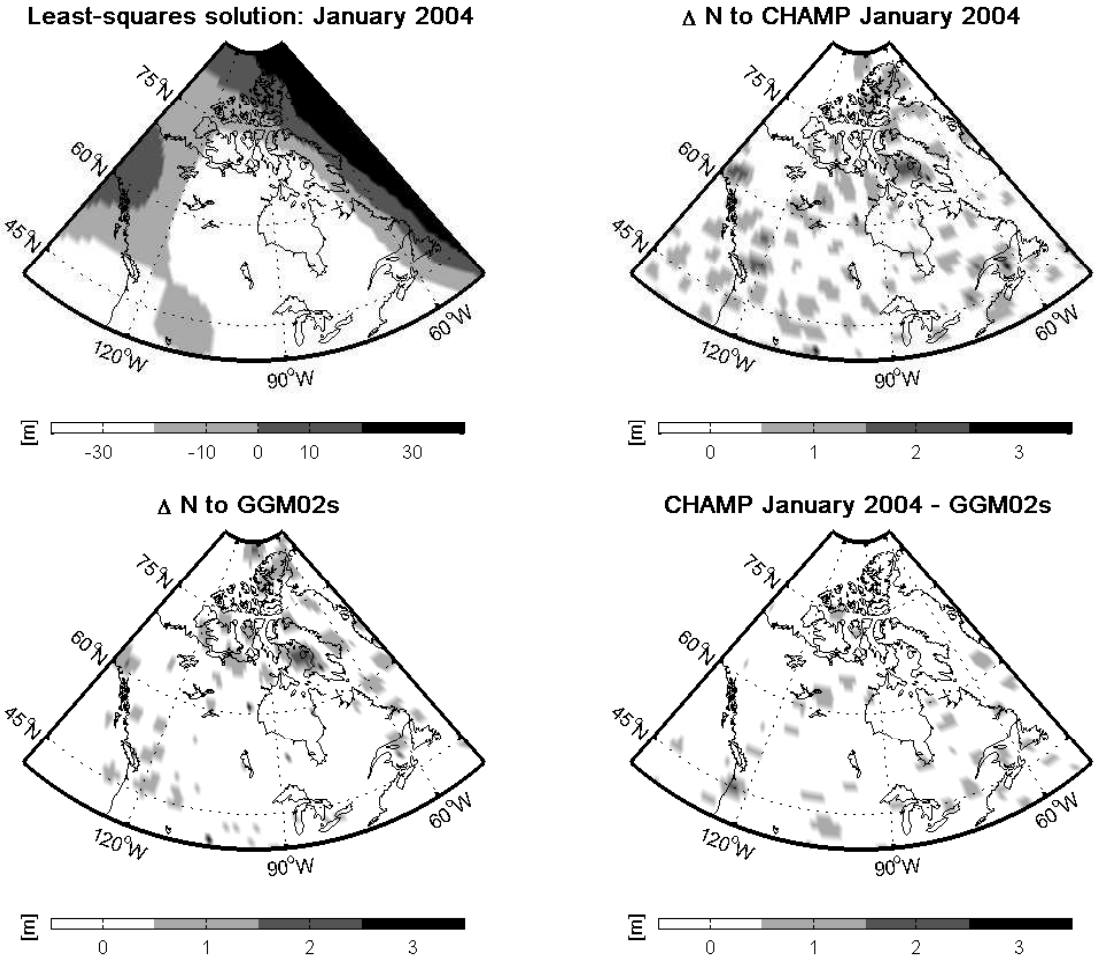

Figure 6.11: The least-squares collocation solution for January 2004 (top left), the comparison to the global CHAMP solution of January 2004 (top right), to GGM02s (bottom left) and the comparison between the global monthly CHAMP solution and GGM02s as a reference.

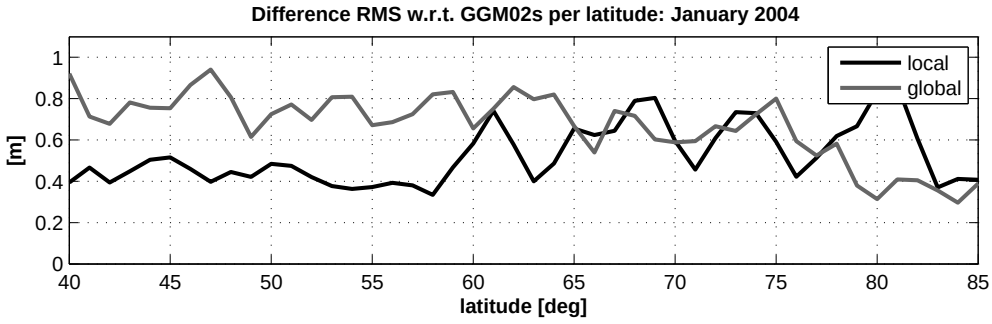

Figure 6.12: Difference RMS per latitude w.r.t. GGM02s at satellite height using least-squares collocation: January 2004.

Starting with January 2004, the comparisons to GGM02s clearly shows that the local solution is outperforming the global spherical harmonic analysis. Note that approximately one order of magnitude in the accuracy is lost due to the downward continuation. The error is around or below 1 m for most of the area. The global monthly solution, on the other hand, has errors of 1 m–2 m for many parts of the area. The overall RMS-value in table 6.4 shows an improvement of 14.2 cm due to the localized calculation.

Surprisingly, the geoid height difference w.r.t. GGM02s per latitude (figure 6.12) shows a better agreement of the local solution with the GRACE-model for the latitude area between 40 ° and 60 °. Beyond these latitudes, the difference RMS increases and is similar to the one of the global monthly solution up to $\varphi = 77\,^\circ$. For higher latitudes, the global solutions are closer, which might be an indication that both global solutions are biased towards the polar areas. On the other hand, the last jump in the local solution is caused by a peak at the northwestern coast of Greenland. Due to this location near the polar gap, these points are likely to be ill-determined. Still, it is surprising that the difference RMS between the local solution and the GRACE-model increases with increasing latitude. Due to the decreasing difference RMS of the two global models the possibility that both global models are biased cannot be excluded without a comparison to independent data, e.g., GPS-leveling or other geoid models like ArcGP. Consequently, it cannot be concluded, if the local or global solution is deficient.

	January 2004	June 2003
LS prediction - CHAMP	0.823 m	2.546 m
LS prediction - GGM02s	0.546 m	0.694 m
CHAMP - GGM02s	0.688 m	2.459 m

Table 6.4: RMS of the difference between the least-squares collocation solutions and the global solutions for Canada

Analogously to the case of the least-squares prediction, a vast improvement is reached in the local solution for June 2003, and this time the effect is very impressive.

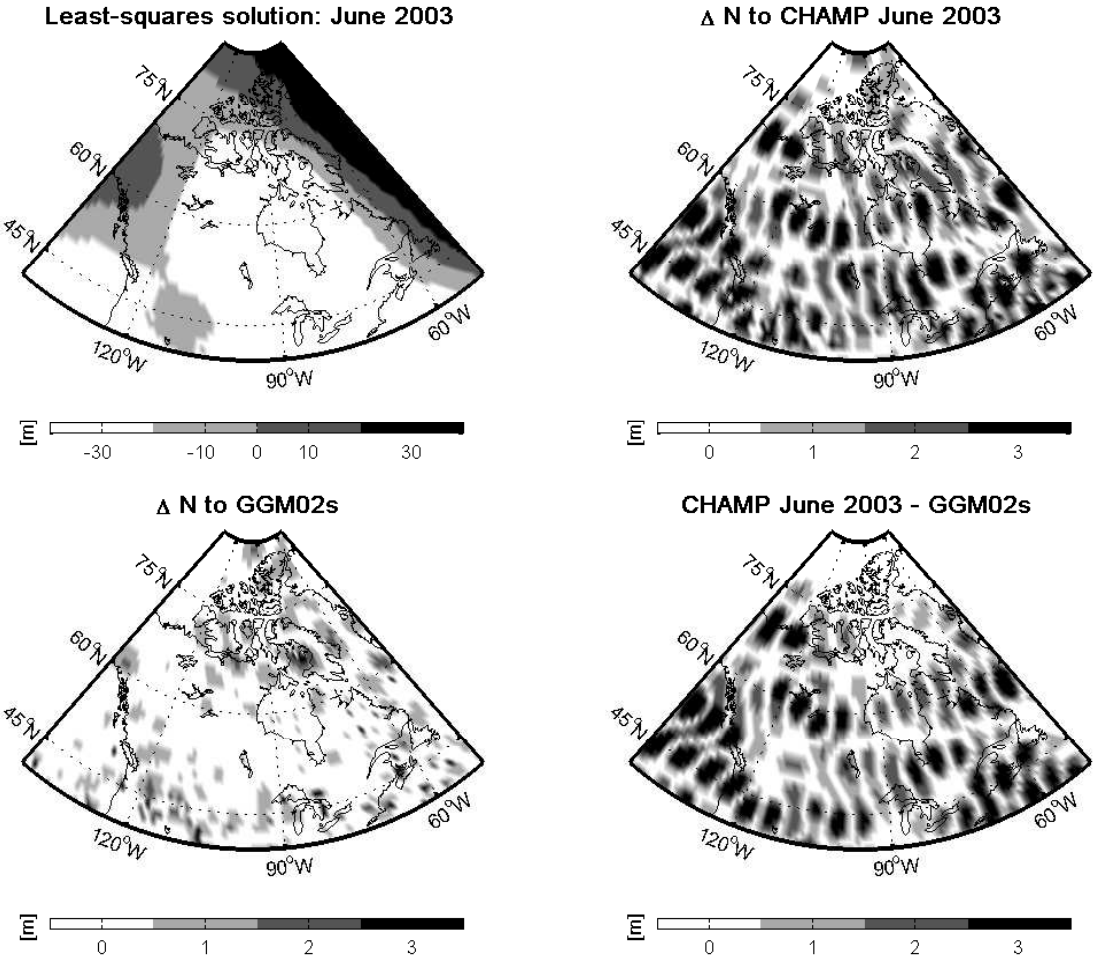

Figure 6.13: The least-squares collocation solution for June 2003 (top left), the comparison to the global CHAMP solution of June 2003 (top right), to GGM02s (bottom left) and the comparison between the global monthly CHAMP solution and GGM02s as a reference.

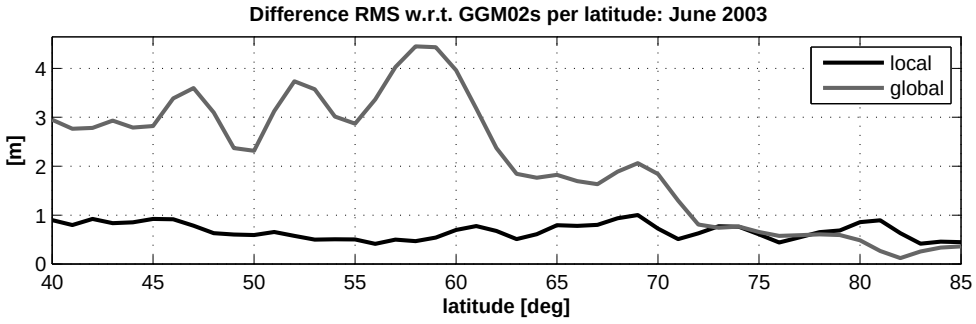

Figure 6.14: Difference RMS per latitude w.r.t. GGM02s at satellite height using least-squares collocation: June 2003.

The global monthly solution shows strong artifacts due to aliasing as discussed in section 4.2.5. The pattern of the groundtracks is visible except for the very high latitude areas. These areas are always densely covered, which also suggests that the spherical harmonic solution is biased towards these areas. However, as mentioned before, the figures show only the difference to GGM02s and it cannot be ruled out that GGM02s is also deficient or biased in these areas. The figures only show that the monthly global CHAMP-only solution and the GGM02s are close in this area.

The difference between the global monthly solution and GGM02s exceeds 3 m whereas the localized solution remains at the level of the January 2004 solution. The overall difference RMS proves this. The value only increases by 14.8 cm. In case of the global monthly CHAMP-only solution for June 2003, the RMS-value is almost tripled. The difference RMS per latitude shows the same picture. For latitudes lower than 62 °, the value is three times higher than the local solution. For $62\,^\circ < \varphi < 71\,^\circ$, the global solution is two times worse and beyond 71 ° the local and global solution are on the same level again.

The collocation solution for June 2003 shows a similar smooth picture as in January 2004. In fact, the patterns are almost identical in figure 6.11 and 6.13 but more pronounced in the latter one. This means that least-squares collocation will yield more consistent results than the global spherical harmonic analysis, which is important for time-variable studies. The improvement, however, is not only reached due to a better data distribution in high latitude areas as suggested earlier, but mostly due to the use of collocation itself.

6.4 Summary

The interpolation at orbit height is not a trivial problem. “Quick and dirty” solutions can only be used for data screening and preliminary solutions. Least-squares prediction is already one of the most sophisticated methods and computationally intensive. Nevertheless, if one is willing to accept this disadvantage, the least-squares prediction

will yield better results in months with sparse groundtrack coverage. The effect is most pronounced for the case of the least-squares collocation, where the smoothing property of the downward continuation supports the derivation of localized and consistent monthly solutions. From this investigation it is not yet clear if the global solutions from both CHAMP and GRACE are biased towards the polar area, or the difference to the local solution is really caused by the improved local solution. Only a test with an independent data source can reveal this. Furthermore, the global covariance model of Tscherning & Rapp was used; the solution might improve by deriving a local covariance model. Both should be investigated numerically in the future.

Chapter 7

Concluding remarks

In this chapter the conclusions and recommendations for future work are outlined. The gravity field recovery in this thesis was based on the principle of energy conservation and was implemented for the case of high-low (CHAMP) and low-low (GRACE) satellite-to-satellite tracking. For the calculations more than 60 million measurements have been processed; 374 Matlab functions with more than 52700 lines of code have been developed. Results have been derived on a global and on a local scale. The following discussion provides a summary of the achievements for each of the three parts of the thesis, namely the global gravity field recovery from CHAMP, the global gravity field recovery from GRACE and the local gravity field recovery in high latitude areas from CHAMP. It should be mentioned that many minor improvements and findings are mentioned in the text but only the major achievements are discussed in the following.

7.1 Conclusions

CHAMP. Two years of CHAMP data have been reprocessed using the energy balance approach and a least-squares adjustment in order to derive gravity models on a global scale. Timewise, monthly as well as two-year solutions have been determined. The important vertices of this part of the thesis are:

1. The two-year solution UofC has been derived and is outperforming the gravity field model TUM2s, although the same input quantities have been used.

2. The calibration using *a priori* information is the primary reason for the improvement in the solution. The filtering of low degree gravity signal is avoided by the selection of a proper mathematical model in the least-squares adjustment and by restricting the estimation to one set of parameters per day. This way, the physical

properties and the behavior of the accelerometer are taken into account.

3. The refined calibration procedure has yielded an improved signal strength till degree and order 40.

4. The derivation of time-variable gravity field information is not possible due to the low accuracy of the CHAMP data. The changing groundtrack pattern has been identified as one of the main contributor to the low accuracy.

5. The loss of the orthogonality in the sine and cosine functions has been identified as the cause of the degradation of the monthly global solutions. The loss of the orthogonality of the Legendre functions, on the other hand, has been ruled out.

6. Considering the GRACE-satellites as two CHAMP-type satellites, the resulting combined monthly solutions start to show variations, which can be connected to mass redistribution. Annual and semi-annual signals are recognizable for some spherical harmonic coefficients whereas others show still a random behavior.

7. The derivation of a two-year combined solution has yielded no further improvement. The limiting factor is the velocity determination by numerical differentiation of kinematic positions.

The improvement w.r.t. TUM2s is maximum for degree 14 with 30%. The cumulative geoid error of the UofC model can reach the 1 cm level with a spatial resolution of 1430 km half wavelength, if the deficient $\bar{C}_{40}$ is replaced by an *a priori* value, e.g., from EGM96. The reason for the deficiency of this coefficient is not clear yet. Investigating the orthogonality of the Legendre functions and the sine/cosine functions in months with good and sparse groundtrack coverage has shown that the data distribution is the main contributor to deficiencies of the global solution and thus is preventing the determination of time-variable gravity patterns.

Currently, the data distribution can only be improved by introducing additional information. Fortunately, the same type of data for the same period of interest is available from the GRACE satellite mission. The idea of using the two GRACE satellites as

CHAMP-like satellites, i.e., no K-band measurements are used, is unique till now and yields a more homogeneous data distribution for the time period of interest. For the combination, variance component estimation is applied. A simple equal weight combination has yielded a deficient solution due to a bias towards the GRACE-data, which has less signal strength due to the higher orbit. The combined solution of months that have formerly been identified with a sparse groundtrack still shows a small deficiency compared to months with good groundtrack coverage. This might be an indication that the weighting coefficients are not yet optimal. Introducing external information into the determination of the weighting factors might improve the situation. Still, by combining single satellite missions, the influence of the groundtrack variability can be minimized. The monthly solutions become more homogeneous and start to show time-variable gravity signals.

GRACE. The energy balance approach for the case of low-low satellite-to-satellite tracking has been derived in the Earth-fixed system, and its feasibility has been investigated using simulated and real GRACE-data. The results of the research are:

1. An exact representation of the velocity difference and consequently of the relative kinetic energy in terms of the K-band measurement has been derived.

2. The error analysis has shown that the limiting factor is the velocity determination from kinematic positions.

3. The application to real GRACE data failed due to the high accuracy demands on the velocity.

The representation of the kinetic energy term in terms of the K-band avoids the approximation suggested by Wolff (1969). The concept has been verified using noiseless simulated data. Compared to the accuracy demands of Jekeli (1999), the newly derived approach can handle about half an order less accurate data and thus has a less stringent condition on the velocity determination. Nevertheless, the approach still demands an

accuracy of 0.077 $^{mm}/_{s}$ and currently the noise in the kinematic position only admits an error-level of 0.14 $^{mm}/_{s}$. Consequently, and due to the higher sensitivity of the observable to noise, the derived monthly solution for August 2002 is one order of magnitude worse than UofC. The situation might be improved by following the approach of Han et al. (2006). By simultaneously adjusting the orbits of the GRACE satellites with the range rate measurements, the accuracy demands can be reduced.

High latitude areas. One of the advantages of the energy balance approach is that it yields pointwise measurements along the orbit. The convergence of the satellite orbit in polar areas forms a denser data distribution than in equatorial areas. Using interpolation and downward continuation techniques, localized solutions at satellite height and on the surface have been derived. The conclusions of this study are:

1. The weighted mean solution has yielded a quick but less accurate solution.

2. The least-squares prediction at satellite height has outperformed the global solution in months with sparse groundtrack coverage.

3. The local solutions derived on the surface with least-squares collocation outperform the global solutions and thus represent an important tool for the investigation of time-variability.

4. The validation showed that the local solutions agree with the GRACE solution better in low than in high latitude areas.

The error of the weighted mean solution strongly depends on the data distribution and does not reach, in comparison to GGM02s, a better level than the corresponding monthly global CHAMP-only solution. The method takes no advantage of the denser information in high-latitude areas. The least-squares methods are computationally intensive for the task of interpolation but for calculation at satellite height have yielded results on the same level as the global solution for month with good groundtrack coverage and

showed a clear improvement for months with sparse groundtracks. The strength of the least-squares prediction is that it allows combination with the downward continuation, thus becoming least-squares collocation which has the property of yielding a smooth solution. However, the predicted value is highly sensitive to outliers and depends on the data distribution in each subset. The behavior of local and global solutions is also contradicting the expectations. It has been anticipated that the local solutions outperform the global solution in high latitude areas due to the higher data density. Failure to do so has three possible explanations. First of all, the local solutions might be deficient due to the data distribution and the high sensitivity of the least-squares collocation to the data distribution. Secondly, the global solutions are biased towards the pole. And thirdly, the global solutions are deficient at high latitudes. A comparison with an independent data source is necessary in order to clarify this situation.

7.2 Recommendations for future work

The applicability of the energy balance approach to a high-low satellite mission has been proven before. In this thesis, several aspects of the data processing have been refined but improvements in some areas of the data processing are possible. For example, the calibration is done using *a priori* information. Although it is generally accepted that every current gravity field can be used and has minimum to no influence on the solution, an iterative scheme might be more beneficial. In the first, step an approximate solution can be derived using e.g. crossover calibration. The preliminary gravity solution can be the input for the next iteration step. Thus the calibration becomes independent of any *a priori* information.

Another not fully understood point is the parametrization and the estimation frequency of calibration parameters. Common procedure of the GeoForschungsZentrum Potsdam is the estimation of daily bias parameters and one monthly scale factor. Other groups estimate scale factors on a daily basis without the estimation of any bias. The primary objective is certainly the calibration of the data and any model enabling this

can be used, but it neglects the physical properties of the accelerometer. In this thesis, the calibration model has been selected with these in mind but a final answer has not been reached so far. Furthermore, with the GGM02s-model an independent data source is available. By determining the potential along the orbit and inverting the energy balance approach, the behavior of the accelerometer can be analyzed. The noise level and the contribution to the solution of each accelerometer axis can be investigated and the optimal number of estimation parameters per time interval can be determined. Certainly, not only the energy balance approach but also other approaches can be used for this.

Concerning the derivation of global solutions from high-low satellite-to-satellite tracking, the focus should be on the improvement of the derivation of monthly solutions. Although GRACE is currently outperforming CHAMP by one order of magnitude, both satellite systems will decay continuously and end probably by 2007. The objectives of physical geodesy include also the monitoring of the time variable gravity field. Future satellite mission like, e.g., the SWARM-mission will consist of three CHAMP-like satellites and thus the optimal combination using variance component estimation is an important tool. The variance is derived from the internal fit of the data, but introducing external criteria might yield an improvement in the global gravity solution. Additionally, coefficients with different degree and order are not equally affected by the different error sources. A degree- and/or order-dependent weighting might be advantageous.

Further efforts should also be undertaken to apply the energy balance approach to the case of low-low satellite-to-satellite tracking. Introducing a reference orbit to the calculations might reduce the accuracy demands for the data. Additionally, the approach of Han et al. (2006) should be investigated in more detail and should be linked to the exact representation of the kinetic energy in terms of the K-band measurement. Also, the use of dynamic position and velocity data should be considered. They might lead to a dependency on the *a priori* gravity field used in the determination of the position and velocity, but the noise level is generally lower than the one of kinematic positions. In case of a successful implementation, certainly the dependency on the *a*

priori data should be investigated, as well. An iterative scheme for orbit determination and gravity field recovery might be able to minimize this influence.

Regarding the local calculations, least-squares collocation has been identified as the most powerful tool, especially when downward continuation is included and necessary. The input data, on the other hand, was not optimal since the same data were used for global calculations. The stepwise improvement of the input data by adapting, e.g., localized tides model and the estimation of local covariance functions will yield further improvements. Deriving consistent data for monthly solutions in high-latitude areas is expected to support studies of time-variability.

List of Abbreviations

BIQUE	best invariant quadratic unbiased estimation
B.G.I.	Bureau Gravimetrique International
BVP	Boundary Value Problem
CEO	Celestial Ephemeris Origin
CEP	Celestial Ephemeris Pole
CGG2000	Canadian Gravimetric Geoid model 2000
CHAMP	CHAllenging Minisatellite Payload
CIP	Celestial Intermediate Pole
CPR	cycle per revolutions
CRS	Celestial Reference System
EGM96	Earth Geopotential Model 1996
EOP	Earth Orientation Parameters
FFT	Fast Fourier Transformation
FIR	Finite Impulse Response
GAST	Greenwich Apparent Sidereal Time
GFZ	GeoForschungsZentrum Potsdam
GGM01s	GRACE Gravity Model 01s
GGM02s	GRACE Gravity Model 02s

$GMST$	Greenwich Mean Sidereal Time
GPS	Global Position System
GRACE	Gravity Recovery And Climate Experiment
GRM	Geopotential Research Mission
IAG	International Association of Geodesy
IAU	International Astronomical Union
IERS	International Earth Rotation Service
JPL	Jet Propulsion Laboratory
LEO	low Earth orbiter
PCCGM	pre-conditioned conjugate gradient method
RSO	Rapid Science Orbits
SBF	Space Body Frame
SLR	Satellite Laser Ranging
SNR	signal-to-noise ratio
SST	satellite-to-satellite tracking
TAI	Temps Atomique International = International Atomic Time
TDT	Terrestrial Dynamic Time
TEO	Terrestrial Ephemeris Origin
T_{GPS}	Global Position System time
TRS	Terrestrial Reference System

TUM1s Technical University Munich model 1s

TUM2s Technical University Munich model 2s

UTC Universal Time Coordinated

$UT1$ mean solar day

VLBI Very Long Baseline Interferometry

References

Ameele, J. (2004). GRACE data processing & orbit and groundtrack analysis. Technical report, University of Calgary & Delft University of Technology.

Antoniou, A. (1979). *Digital filters: analysis and design*. McGraw-Hill Book Company.

Austen, G. and Reubelt, T. (2000). Räumliche Schwerefeldanalyse aus semi-kontinuierlichen ephemeriden niedrigfliegender GPS-vermessener Satelliten vom Typ CHAMP, GRACE und GOCE. Master's thesis, Universität Stuttgart, Geodätisches Institut.

Balmino, G., Perosanz, F., Rummel, R., Sneeuw, N., and Sünkel, H. (1999). CHAMP, GRACE and GOCE: mission concepts and simulations. *Bolletino di Geofisica Teorica ed Applicata*, 40(3–4):309–319.

Bjerhammer, A. (1967). A new approach to satellite geodesy. Technical report, USAEGI MRADA, Alexandria, Virginia.

Bruton, A., Glennie, C., and Schwarz, K. (1999). Differentiation for high-precision GPS velocity and acceleration determination. *GPS Solutions*, 2(4):7–21.

Buttkus, B. (1991). *Spektralanalyse und Filtertheorie*. Springer.

Cheng, M., Gunter, B., Ries, J., Chambers, D., and Tapley, B. (2004). Temporal variations in the Earth's gravity field from SLR and CHAMP GPS data.

Colombo, O. (1983). Numerical methods for harmonic analysis on the sphere. Technical report, Report No.310, Dept. Geod. Sci. and Surv., Ohio State Univ., Columbus, Ohio.

Ditmar, P. and Klees, R. (2002). A method to compute the Earth's gravity fied from SGG / SSTdata to be acquired by the GOCE satellite. Technical report, Delft University.

Ditmar, P. and van Eck van der Sluijs, A. (2004). A technique for modeling the Earth's gravity field on the basis of satellite accelerations. *Journal of Geodesy*, 78:12–33.

Eanes, R. (2002). The CSR4.0 global ocean tidal model. `ftp.csr.utexas.edu/pub/tide`.

Flechtner, F. (2005). AOD1B Product Description Document. Technical report, GeoForschungszentrum Potsdam.

Földváry, L., Švehla, D., Gerlach, C., Wermuth, M., Gruber, T., Rummel, R., Rothacher, M., Frommknecht, B., Peters, T., and Steigenberger, P. (2005). Gravity model TUM-2Sp based on the energy balance approach and kinematic CHAMP orbits. In Reigber et al. (2005c),

pages 13–18.

Garcia, R. (2002). *Local geoid determination from GRACE*. PhD thesis, Ohio State University.

Gerlach, C. (2003). A annote on the use of energy integrals for gravity field recovery.

Gerlach, C., Földváry, L., Švehla, D., Gruber, T., Wermuth, M., Sneeuw, N., Frommknecht, B., Oberndorfer, H., Peters, T., Rothacher, M., Rummel, R., and Steigenberger, P. (2003a). A CHAMP-only gravity field model from kinematic orbits using the energy integral. *Geophysical Research Letters*, 30(20):7–1–7–4.

Gerlach, C., Sneeuw, N., Visser, P., and Švehla, D. (2003b). CHAMP gravity field recovery using the energy balance approach. *Advances in Geosciences*, 1:73–80.

Gerlach, C., Sneeuw, N., Visser, P., and Švehla, D. (2003c). CHAMP gravity field recovery with the energy balance approach: first results. In Reigber, C., Lühr, H., and Schwintzer, P., editors, *First CHAMP mission results for gravity, magnetic and atmospheric studies*. GeoForschungsZentrum, Potsdam, Springer.

GFZ Potsdam (2000). ISDC - information systems and data center. `http://isdc.gfz-potsdam.de/index.php`.

Han, S. (2003). *Efficient Global Gravity Determination form Satellite-to-Satellite Tracking (SST)*. PhD thesis, Geodetic and GeoInformationScience, Ohio State University.

Han, S. (2004). Efficient determination of global gravity field from satellite-to-satellite tracking missions. *Celestial Mechanics and Dynamical Astronomy*, 88:69–102.

Han, S., Jekeli, C., and Shum, C. (2002). Efficient gravity field recovery using in situ disturbing potential observables from CHAMP. *Geophysical Research Letters*, 29(16):36–1–36–4.

Han, S., Jekeli, C., and Shum, C. (2003). Static and temporal gravity field recovery using GRACE potential difference observables. *Advances in Geosciences*, (1):19–26.

Han, S., Jekeli, C., and Shum, C. (2004). Time-variable aliasing effects of ocean tides, atmosphere, and continental water mass on monthly mean GRACE gravity field. *Journal of Geophysical Research*, 109:B04403.

Han, S., Shum, C., and Jekeli, C. (2006). Precise estimation of in situ geopotential differences from GRACE low-low satellite-to-satellite tracking and accelerometer data. *Journal of Geophysical Research*, 111:B04411.

Hanson, A. (2006). *Visualizing Quaternions*. Morgan Kaufmann Publishing.

Heiskanen, W. and Moritz, H. (1967). *Physical geodesy*. W.H. Freeman and Company San

Francisco.

Howe, E., Stenseng, L., and Tscherning, C. (2003). Analysis of one month of CHAMP state vector and accelerometer data for the recovery of the gravity potential. *Advances in Geosciences*, 1:1–4.

IERS (2002). Explanatory supplement to IERS bulletins A and B. `http://hpiers.obspm.fr/eoppc/bul/bulb/explanatory.html`.

Ilk, K. (2001). Special commission SC7, gravity field determination by satellite gravity gradiometry. `http://www.geod.uni-bonn.de/SC7/sc7.html`.

Ilk, K., Flury, J., Rummel, R., Schwintzer, P., Bosch, W., Haas, C., Schröter, J., Stammer, D., Zahel, W., Miller, H., Dietrich, R., Huybrechts, P., Schmeling, H., Wolf, D., Riegger, J., Bardossy, A., and Güntner, A. (2004). Mass transport and mass distribution in the Earth system.

Jacobi, C. (1836). Über ein neues Integral fuer den Fall der drei Körper, wenn die Bahn des störenden Planeten kreisförmig angenommen und die Masse des gestörten vernachlässigt wird. *Monthly reports of the Berlin Academy.*

Jekeli, C. (1996). Spherical harmonic analysis, aliasing, and filtering. *Journal of Geodesy*, 70:214 – 223.

Jekeli, C. (1999). The determination of gravitational potential differences from satellite-to-satellite tracking. *Celestial Mechanics and Dynamical Astronomy*, 75:85–101.

Jekeli, C. and Garcia, R. (2000). Local geoid determination with in-situ geopotential data obtained from satellie-to-satellite tracking. In Sideris, M., editor, *Gravity, Geoid and Geodynamics 2000*, volume 123 of *International Association of Geodesy Symposia*, pages 123–128. IAG, Springer.

Kertz, W. (2002). Biographisches Lexikon zur Geschichte der Geophysik. `http://www.geophys.tu-bs.de/geschichte/index1.html`.

Khan, I. and Ohba, R. (1999). Closed-form expressions for the finite difference approximations of first and higher derivaties based on Taylor series. *Journal of Computational and Applied Mathematics*, 107:179–193.

Kim, M. (1997). Theory of satellite ground-track crossover. *Journal of Geodesy*, 71:749–767.

Koch, K. and Kusche, J. (2002). Regularization of geopotential determination from satellite data by variance components. *Journal of Geodesy*, 76:259–268.

Koop, R. (1993). *Global gravity field modelling using satellite gravity gradiometry.* PhD thesis, Technische Universiteit Delft, Delft, Netherlands.

Lerch, F. (1991). Optimum data weighting and error calibration for estimation of gravitational parameters. *Bulletin Géodésique*, 65:44–52.

Letellier, T. (2004). *Etude des ondes de mare sur les plateux continentaux, FES2004 - Road to the data and the thesis (in French).* Thèse doctorale, Universit de Toulouse III, Ecole Doctorale des Sciences de l'Univers, de l'Environnement et de l'Espace.

Lyons, R. (1997). *Understanding digital signal processing.* Prentice Hall PTR.

McAdoo, D., Wagner, C., and Laxon, S. (2005). Improvement in Arctic gravity and geoid from CHAMP and GRACE: an evaluation. In Reigber et al. (2005c).

McCarthy, D. D. and Petit, G. (2003). IERS 2000 conventions. Technical Report 32, IERS, Frankfurt am Main, Verlag des Bundesamts fr Kartographie und Geodäsie.

Milani, A., Nobili, A. M., and Farinella, P. (1987). *Non-gravitational perturbations and satellite geodesy.* Adam Hilger.

Montenbruck, O. and Gill, E. (2000). *Satellite orbits.* Springer.

Moritz, H. (1980a). *Advanced Physical Geodesy.* Wichmann, Karlsruhe.

Moritz, H. (1980b). Geodetic Reference System 1980. Technical report.

Müller, J. (1999). Zeitskalen. In Schneider, M., editor, *3. DFG-Rundgespräch zum Thema Bezugssysteme*, volume 5 of *Mitteilungen des BKG.*

Niemeier, W. (2001). *Ausgleichsrechnung.* Walter de Gruyter.

O'Connor, J. and Robertson, E. (1999). The MacTutor history of mathematics archive. `http://www-history.mcs.st-andrews.ac.uk`.

O'Keefe, J. (1957). An application of jacobi's integral to the motion of an Earth satellite. *The Astronomical Journal*, 62(8):266–267.

Raizner, C., Weigelt, M., and Sideris, M. (2006). On the accelerometer calibration onboard GRACE. Presented at the Astro 2006 - 13th Canadian Astronautics Conference and 53rd Annual General Meeting, Montreal 2006.

Reigber, C. (1969). Zur Bestimmung des Gravitationsfeldes der Erde aus Satellitenbeobachtungen. Reihe C 137, DGK.

Reigber, C. (1989). *Theory of satellite geodesy and gravity field determination*, chapter Gravity field recovery from satellite tracking data, pages 197–234. Number 25 in Lecture annotes

in Earth science. Springer.

Reigber, C., Balmino, G., Schwintzer, P., Biancale, R., Bode, A., Lemoine, J.-M., König, R., Loyer, S., Neumayer, H., Marty, J.-C., Barthelmes, F., Perosanz, F., and Zhu, S. (2002). A high-quality global gravity field model from CHAMP GPS tracking data and accelerometry (EIGEN-1S). *Geophysical Research Letters*, 29(14):37–1–37–4.

Reigber, C., Jochmann, H., Wünsch, J., Petrovic, S., Schwintzer, P., Barthelmes, F., Neumayer, K., König, R., Förste, C., Balmino, G., Biancale, R., Lemoine, J., Loyer, S., and Perosanz, F. (2005a). Earth gravity field and seasonal variability from CHAMP. In Reigber, C., Lühr, H., Schwintzer, P., and Wickert, J., editors, *Earth observation with* CHAMP - *Results from three years in orbit*, pages 25 – 30. Springer.

Reigber, C., Jochmann, H., Wünsch, J., Petrovic, S., Schwintzer, P., Barthelmes, F., Neumayer, K., König, R., Förste, C., Balmino, G., Biancale, R., Lemoine, J.-M., Loyer, S., and Perosanz, F. (2005b). Earth gravity field and seasonal variability from CHAMP. In Reigber et al. (2005c), pages 25–30.

Reigber, C., Lühr, H., Schwintzer, P., and Wickert, J., editors (2005c). *Earth observation with CHAMP: Results from three years in orbit*. Springer.

Reigber, C., Schwintzer, P., Neumayer, K.-H., Barthelmes, F., König, R., Förste, C., G.Balmino, Biancale, R., Lemoine, J.-M., Loyer, S., Bruinsma, S., Perosanz, F., and Fayard, T. (2003). The CHAMP-only Earth gravity field model EIGEN-2. *Advances in Space Research*, 31(8):1883–1888.

Reigber, C., Schwintzer, P., Stubenvoll, R., Schmidt, R., Flechtner, F., Meyer, U., König, R., Neumayer, H., Förste, C., Barthelmes, F., Zhu, S., Balmino, G., Biancale, R., Lemoine, J.-M., Meixner, H., and Raimondo, J. (2004). A high resolution global gravity field model combining CHAMP and GRACE satellite mission and surface gravity data: EIGEN-CG01C. *Journal of Geodesy*, submitted in August.

Reubelt, T., Austen, G., and Grafarend, E. (2003). Harmonic analysis of the Earth's gravitational field by means of semi-conitnuous ephemeris of a low Earth orbiting GPS-tracked satellite. Case study: CHAMP. *Journal of Geodesy*, 77:257–278.

Reubelt, T., Götzelmann, M., and Grafarend, E. (2006). *Observation of the Earth System from Space*, chapter Harmonic analysis of the Earth's gravitational field from kinematic CHAMP orbits based on numerically derived satellite accelerations, pages 27–42. Springer.

Rummel, R., Balmino, G., Johannessen, J., Visser, P., and Woodworth, P. (2002). Dedicated gravity field missions - principles and aims. *Journal of Geodynamics*, 33:3–20.

Rummel, R., Reigber, C., and Ilk, K. (1978). The use of satellite-to-satellite tracking for gravity parameter recovery. In *Proceedings of the European Workshop on Space Oceanography, Navigation and Geodynamics (SONG)*.

Rummel, R. and van Gelderen, M. (1995). Meissl scheme - spectral characteristics of physical geodesy. *manuscripta geodetica*, 20:379 – 385.

Sansò, F. (1990). On the aliasing problem in the spherical harmonic analysis. *Bulletin Geodetica*, 64:313 – 330.

Schneider, M. (1992). *Himmelsmechanik, Band I: Grundlagen, Determinierung*. BI Wissenschaftsverlag.

Schönauer, W. (2000). *Architecture and use of shared and distributed memory parallel computers*. Self-Edition by W. Schönauer.

Schrama, E. (1989). The role of orbit errors in processing of satellite alitmeter data. Technical Report 33, Netherlands Geodetic Commission.

Schwiderski, H. (1984). Combined hydrodynamical and empirical modeling of ocean tides. In Seeber, G. and Apel, editors, *Geodetic Features of the Ocean Surface and their Implications*, number 215 – 229. D. Reidel, Dordrecht.

Seeber, G. (2003). *Satellite geodesy*. Walter de Gruyter, 2 edition.

Sneeuw, N. (1994). Global spherical harmonic analysis by least squares and numerical quadrature methods in historical perspective. *Geophysical Journal International*, 118:707 – 716.

Sneeuw, N. (2000). A semi-analytical approach to gravity field analysis from satellite observations. Reihe C 527, DGK.

Sneeuw, N. (2003). Space-wise, time-wise, torus and rosborough representations in gravity field modelling. *Space Science Reviews*, 108:37–46.

Sneeuw, N., Gerlach, C., Földváry, L., Gruber, T., Peters, T., Rummel, R., and Švehla, D. (2005). One year of time-variable CHAMP-only gravity field models using kinematic orbits. In Sansò, F., editor, *A window on the future of geodesy*, volume 128 of *International Association of Geodesy Symposia*, pages 288–293. Springer.

Sneeuw, N., Gerlach, C., Švehla, D., and Gruber, C. (2003). A first attempt at time-variable gravity field recovery from CHAMP using the energy balance approach. In Tziavos, I.,

editor, *Gravity and Geoid 2002*, Proceedings of 3rd Meeting of the International Gravity and Geoid Commission, pages 237–242, Thessaloniki, Greece. Editions ZITI.

Sneeuw, N. and Ilk, K. (1997). The status of spaceborne gravity field mission concepts: a comparative simulation study. In Segawa, J., Fujimoto, H., and Okubo, S., editors, *Gravity, Geoid and Marine Geodesy*, International Association of Geodesy, pages 171–178. Springer.

Sneeuw, N. and van Gelderen, M. (1997). The polar gap. In Sansò, F. and Rummel, R., editors, *Geodetic boundary value problems in view of the one centimeter geoid*, volume 65. Springer-Verlag, Berlin.

Švehla, D. and Rothacher, M. (2004). Two years of CHAMP kinematic orbits for geosciences. presented at the European Geosciences Union, 1st General Assembly, Nice, France, 2004.

Švehla, D. and Rothacher, M. (2005). Kinematic precise orbit determination for gravity field determination. In Sansò, F., editor, *A window on the future of geodesy*, volume 128 of *International Association of Geodesy Symposia*. Springer.

Tapley, B., Bettadpur, S., Watkins, M., and Reigber, C. (2004a). The gravity recovery and climate experiment: mission overview and early results. *Geophysical Research Letters*, 31(L09607):1 – 4.

Tapley, B., Ries, J., Bettadpur, S., Chambers, D., Cheng, M., Condi, F., Gunter, B., Kang, Z., Nagel, P., Pastor, R., Pekker, T., Poole, S., and Wang, F. (2005). GGM02 - An improved Earth gravity field model from GRACE. *Journal of Geodesy*, 79:467 – 478.

Tapley, B., S.Bettadpur, Ries, J., Thompson, P., and Watkins, M. (2004b). GRACE measurements of mass variability in the Earth system. *Science*, 305:503–505.

Tipler, P. (1995). *Physik*. Spektrum Akademischer Verlag.

Torge, W. (2001). *Geodesy*. Walter de Gruyter, 3 edition.

Touboul, P., Foulon, B., and Clerc, G. L. (1998). STAR, the accelerometer for the geodesic mission CHAMP.

Trefethen, L. and Bau III., D. (1997). *Numerical linear algebra*. Siam.

Tscherning, C. and Rapp, R. (1974). Closed covariance expressions for gravity anomalies, geoid undulations, and deflections of the vertical implied by anomaly degree variance models. Technical report, Ohio State University.

Véronneau, M. (2001). The Canadian Gravimetric Model of 2000 (CGG2000). `http://www.geod.rncan.gc.ca/publications/papers/pdf/cgg2000a.pdf`.

Visser, P., Sneeuw, N., and Gerlach, C. (2003). Energy integral method for the gravity field determination from satellite orbit coordinates. *Journal of Geodesy*, 77:207–216.

Vonbun, F. (1977). Probing the earth's gravity field by means of satellite-to-satellite tracking. *Phil. Trans. R. Soc. Lond. A.*, 284:475–483.

Wagner, C., McAdoo, D., Klokočník, J., and Kostelecký, J. (2006). Degradation of geopotential recovery from short repeat-cycle orbits: application to GRACE monthly fields. *Journal of Geodesy*, 80(2):94–103.

Wahr, J., Swenson, S., Zlotnicki, V., and Velicogna, I. (2004). Time-variable gravity from GRACE: first results. *Geophysical Research Letters*, 31(L11501):1–4.

Weigelt, M., Sideris, M., and Sneeuw, N. (2006a). Combination of CHAMP and GRACE data for gravity field analysis. Poster presented at 1st symposium of the International Gravity Field Service (IGFS) of the International Association of Geodesy (IAG), Istanbul, Turkey, 2006, also presented at Canadian Geophysical Union Annual Meeting, Banff, Canada, 2006.

Weigelt, M., Sideris, M., and Sneeuw, N. (2006b). High-latitude local gravity field recovery from CHAMP with least-squares collocation. Poster presented at the European Geosciences Union, General Assembly 2006, Wien, Austria 2006.

Weigelt, M. and Sneeuw, N. (2004). Numerical velocity determination and calibration methods for CHAMP using the energy balance approach. In Jekeli, C., Bastos, L., and Fernandes, J., editors, *Gravity, Geoid and Space Missions - GGSM2004*, volume 129 of *IAG Symposia*, pages 54 – 59. Springer.

Wermuth, M., Švehla, D., Földváry, L., Gerlach, C., Gruber, T., Frommknecht, B., Peters, T., Rothacher, M., Rummel, R., and Steigenberger, P. (2004). A gravity field model from two years of CHAMP kinematic orbits using the energy balance approach. Presentation at the EGU 1st General Assembly, Nice.

Wolff, M. (1969). Direct measurement of Earth's gravitational potential using a satellite pair. *Journal of Geophysical Research*, 74(22):5295–5300.

Xu, C., Sneeuw, N., and Sideris, M. (2006). The torus approach for spaceborne gravimetry. In Xu, P., editor, *Theoretical and Computational Geodesy: Challenge and Role of Modern Geodesy*, volume 130.

Yamamoto, K., T.Otsubo, Kubo-oka, T., and Fukuda, Y. (2005). A simulation study of effects of GRACE orbit decay on the gravity field recovery. *Earth Planets Space Letter*, 57.